

Computational Studies of Dendritic Deposition and Trajectory Phase Coexistence

Thesis by
Daniel Rance Jacobson

In Partial Fulfillment of the Requirements for the
Degree of
Doctor of Philosophy in Chemical Engineering

The logo for the California Institute of Technology (Caltech), featuring the word "Caltech" in a bold, orange, sans-serif font.

CALIFORNIA INSTITUTE OF TECHNOLOGY
Pasadena, California

2022
Defended 5/24/2022

© 2022

Daniel Rance Jacobson
ORCID: 0000-0001-7990-4093

All rights reserved except where otherwise noted

ACKNOWLEDGEMENTS

I would like to thank my advisor Tom Miller for his patience and guidance throughout my Ph.D. I also would not have made it to this point without the mentorship and encouragement of my collaborator Steve Whitlam. Finally, I want to thank all the members of the Miller Group for the many great memories I have of the past six years, research-related or otherwise. I couldn't imagine spending this journey with a better group of colleagues and friends.

ABSTRACT

Many out-of-equilibrium systems display collective transitions in the behavior of particles akin to phase transitions. The field of nonequilibrium statistical mechanics seeks to develop new theories and methods to characterize these phenomena. In this thesis, we advance this aim by presenting computational studies of two different kinds of nonequilibrium transitions: the compact-to-dendritic (CTD) transition in the deposition of Brownian particles and trajectory phase coexistence (TPC) in stochastic dynamical systems.

The CTD transition occurs when Brownian particles (like ions, colloids, or misfolded proteins) deposit from all sides onto a reactive cluster. While the cluster initially maintains a compact morphology, upon reaching a critical radius, it spontaneously develops dendritic branches. Although the size of the critical radius depends on the deposition conditions, this relationship is not well understood at a mechanistic level. Here, we show that contrary to previous evidence, the critical radius in Brownian dynamics simulations follows the behavior predicted by a continuum analysis. That is, dendrites emerge when the cluster circumference exceeds the length that particles can diffuse in the characteristic reaction timescale. Consequently, our results provide microscopic validation for continuum methods that are widely applied to study dendrite formation in electrodeposition and lithium metal batteries.

Trajectory phase coexistence (TPC) arises when qualitatively different trajectory behaviors interconvert in a stochastic dynamical system. This type of coexistence plays a central role in theories of glassy dynamics. In this work, we focus on two different research areas related to TPC. First, we introduce an importance sampling method, Variational Ansatz for Rare Dynamics (VARD), for characterizing a system's rate function. VARD is technically and conceptually straightforward yet can still sample the large deviations of many-body models found in the literature. We then examine the meaning of kinks in the scaled cumulant generating function (SCGF). Although these singularities are often taken to be proof that TPC occurs, a more precise understanding of the connection between kinks and coexistence remains lacking. By characterizing the dynamics of two kinds of random walkers, we show that kinks actually result from diverging timescales in the dynamics and do not always indicate the presence of TPC.

PUBLISHED CONTENT AND CONTRIBUTIONS

1. Jacobson, D. & Miller III, T. F. Compact-to-Dendritic Transition in the Reactive Deposition of Brownian Particles. Version 3. arXiv: 2204.01173 [cond-mat]. <http://arxiv.org/abs/2204.01173> (Apr. 12, 2022)

DJ conceived the study, performed the simulations, analyzed the data, and wrote the manuscript.

2. Jacobson, D. & Whitelam, S. Direct Evaluation of Dynamical Large-Deviation Rate Functions Using a Variational Ansatz. *Physical Review E* **100**, 052139. <https://link.aps.org/doi/10.1103/PhysRevE.100.052139> (Nov. 25, 2019)

DJ participated in conceiving the study, ran the simulations, analyzed the data, and participated in writing the manuscript.

3. Whitelam, S. & Jacobson, D. Varied Phenomenology of Models Displaying Dynamical Large-Deviation Singularities. *Physical Review E* **103**, 032152. <https://link.aps.org/doi/10.1103/PhysRevE.103.032152> (Mar. 29, 2021)

DJ participated all of the following: conceiving the study, running the simulations, analyzing the data, and writing the manuscript.

TABLE OF CONTENTS

Acknowledgements	iii
Abstract	iv
PUBLISHED CONTENT AND CONTRIBUTIONS	v
Table of Contents	v
List of Illustrations	viii
List of Tables	xvi
Chapter I: Introduction	1
1.1 The Compact-to-Dendritic Transition in Reactive Deposition	1
1.2 Trajectory Phase Coexistence	2
1.3 Sampling the Rate Function	4
1.4 The Meaning of a Kink in the SCGF	5
Chapter II: Compact-to-Dendritic Transition in the Reactive Deposition of	
Brownian Particles	11
2.1 Introduction	11
2.2 Model Definitions	16
2.3 Theory and Methods	18
2.4 Results and Discussion	26
2.5 Conclusion	29
2.6 Acknowledgments	30
Supplementary Materials: Compact-to-Dendritic Transition in the Reactive	
Deposition of Brownian Particles	34
2.7 Linear Stability Analysis of the Continuum Growth Model	34
2.8 Brownian Dynamics Simulations	37
2.9 Reactive Deposition on a Lattice	43
2.10 First-Hit Distribution in Three Dimensions	45
Chapter III: Direct evaluation of dynamical large-deviation rate functions	
using a variational ansatz	50
3.1 Introduction	50
3.2 A variational ansatz for rare dynamics	54
3.3 VARD applied to four examples	69
3.4 Conclusions	81
3.5 Acknowledgments	83
Chapter IV: Varied phenomenology of models displaying dynamical large-	
deviation singularities	89
4.1 Introduction	89
4.2 Driven random walker	90
4.3 Undriven random walker	95
4.4 When should we expect intermittency?	96
4.5 Singularities in non-ergodic models	100

4.6	Discussion & Conclusions	102
4.7	Acknowledgments	104
A	Appendix: Thermodynamic interpretation of walker models	104
B	Appendix: Large-deviation functions of the growth model	105

LIST OF ILLUSTRATIONS

<i>Number</i>	<i>Page</i>
<p>2.1 The compact-to-dendritic transition for discrete deposition at $\log_{10} \text{Da} = -2.12$. Panels (a) and (b) illustrate the two-dimensional deposition process. The N particles in these panels are rendered with a radius twice that of the actual radius for clarity. The ith band of color moving outwards from the center corresponds to the structure after $iN/5$ particles have been deposited. (a) Initially, the cluster displays a compact morphology. (b) However, upon reaching a critical radius, it spontaneously forms dendritic branches. (c) During three-dimensional deposition, a similar dendritic morphology emerges at large length scales. Here, particles are colored based on their distance from the origin. The inset shows a two-dimensional slice through the initial compact cluster, $N = 1 \times 10^6$, with a continuous gradient color scheme based on the deposition order.</p>	13
<p>2.2 The probability that the Brownian particle reacts with wall A, Φ_A, for various values of the timestep Δt. Red triangles correspond to simulations run at $\psi_A = 1/4$ where the sticking probability at wall A, P_A, varies according to (2.10). As $\Delta t \rightarrow 0$, these simulations approach the analytical result from (2.13), $\Phi_A = 1/10$ (red horizontal line). In contrast, the blue, orange, and green diamonds were generated from simulations that used the fixed values of the sticking probability indicated in the upper-right legend. As $\Delta t \rightarrow 0$, these data approach $\Phi_A = 1/2$ (black-dashed line), the infinitely fast reaction limit, following the predictions of (2.9) and (2.13) (blue, orange, and green curves). All numerical data points were generated using 10^4 samples. Error bars constructed from Wald confidence intervals are smaller than the symbols [32].</p>	20

- 2.3 Continuum limit scaling analysis of the compact-to-dendritic transition in two dimensions. All error bars are bootstrapped 95% confidence intervals (CI) and are sometimes smaller than the lines or symbols. See Table 2.1 for further trajectory details. (a) The fractal dimension \mathcal{D}_F versus the radius of gyration R_g for various values of the Damköhler number, Da . (b) Absolute value of the derivative of the fractal dimension $|\mathcal{D}'_F|$. The peaks define the critical radius at each value of Da , see (2.18). (c) The critical radius R_c as a function of Damköhler number. (d) The derivative of panel (c), Γ , which provides an estimate for the scaling exponent γ in (2.3) as $Da \rightarrow 0$. The leftmost (blue) point has a value of -0.06 with a 95%CI of $[-0.03, -0.09]$. At the top of the panel, the black dashed line represents the hypothesis that $\gamma = 0$. (e) The maximum value of $|\mathcal{D}'_F|$ (or equivalently $|\mathcal{D}'_F|$ evaluated at critical radius) versus the Damköhler number. A linear fit to the three points with the lowest Da values (dash-dot black line) has a slope of -0.15 with a 95%CI of $[-0.16, -0.14]$ 24
- 2.4 Continuum limit scaling of the compact-to-dendritic transition in three dimensions. Panel axis labels are the same as in Fig. 2.3, but note the difference in scale between panel (d) and Fig. 2.3(d). The repeated caption is provide for convenience. See Table 2.2 for further trajectory details. (a) Fractal dimension \mathcal{D}_F as a function of the radius of gyration R_g for different Damköhler numbers, Da . (b) The absolute value of the derivative of panel (a), $|\mathcal{D}'_F|$. (c) The critical radius R_c versus Da . (d) Derivative of the log of the critical radius with respect to the log of the Damköhler number, Γ . The black dashed line corresponds to the $\gamma = 0$ hypothesis. (e) Height of the peak in panel (b), $\max |\mathcal{D}'_F|$, versus the Damköhler number. 26

- 2.5 Test of the timestep and parallel algorithm convergence for 2D (a) and 3D (b) Brownian dynamics simulations. Each panel shows the critical radius R_c versus the Damköhler number Da for the serial (blue and orange curves) and parallel (green curve) algorithms. The serial curves were generated with different values of the cutoff distance σ_{cut} and the root-mean-square-displacement per timestep $\sqrt{d\eta^2}$ (which implicitly sets the value of the timestep Δt , see (2.37)). Note that to increase the visibility of individual points, the x-values of the orange and green curves in both panels are shifted by 0.025 and -0.025 , respectively. 41
- 2.6 Illustration of a particle (light blue) with radius a represented on square lattices with varying lattice constants l . As l becomes smaller, the particle takes up in increasing number of lattice sites. 44
- 2.7 The particle lies on the z -axis a distance α away from the center of an absorbing unit sphere. Once released, it diffuses until it escapes off to infinity or absorbs at polar angle θ 45

- 3.1 Large deviations from a variational ansatz for rare dynamics (VARD).
 (a) We aim to bound or calculate the large-deviation rate function $J(a)$ (black dashed line) for a given model and observable a , under the continuous-time dynamics (4.2) and (3.4). We introduce a reference model (3.7) and (3.9), a variational ansatz for the rare dynamics of the original model conditioned upon a . The reference model has rate function $\tilde{J}(a)$ (gray line; we do not aim to compute this function). The typical value of a generated by the reference model is \tilde{a}_0 ; this is potentially far from the typical value a_0 generated by the original model. Evaluation of (3.17) from the sample mean of a single trajectory of the reference model produces one point $J_0(\tilde{a}_0)$ on the blue line, an upper bound on $J(a)$. (b) If we can evaluate the auxiliary rate function $\tilde{J}(\delta q, \tilde{a}_0)$ at the point δq^* at which its gradient is unity, then we can calculate the correction term (3.18) and determine one point on the green curve in panel (a), the exact rate function of the original model. If not, then we gain information about the quality of the bound $J_0(\tilde{a}_0)$. Variation of the parameters of the reference model allows reconstruction of the entire blue and (potentially) green curves in panel (a). VARD thus reduces a single nonlocal problem, the computation of $J(a)$ arbitrarily far from a_0 , to a series of local problems, each requiring the evaluation of an auxiliary rate function $\tilde{J}(\delta q, \tilde{a}_0)$ at the point δq^* at which its gradient is unity. As we show in this paper, this procedure can be carried out for models commonly found in the literature using relatively simple choices of reference model. 56
- 3.2 Entropy production rate σ for the 4-state model of Ref. [55], the rates W_{xy} of which are given by (3.36). (a) Bounds (3.17) for the large-deviation rate function $J(\sigma)$. Each point on the colored lines results from a reference-model dynamics [Eqns. (3.7) and (3.9)] obtained by scanning the indicated parameters. The black dashed line is the exact answer. (b) Bound (blue line) resulting from a scan of the parameters s and λ compared with the WLR bound of Ref. [55], Eq. (3.37). Inset: The sum (green line) of the bound and the correction (3.18) equals the exact rate function, arbitrarily far into its tails. The boxed region in panel (b) indicates the scale of Fig. 2 of Ref. [55]. Error bars for both axes are smaller than the thickness of the lines. 69

- 3.3 Large-deviation rate function $J(c)$ of particle current, c , for the version of the ASEP studied in Ref. [55]; rate constants are given in the text. (a) We show the exact answer (black), the WLR universal current bound [54, 55] (gray), and the bound produced using our default (s, λ) reference-model parameterization (dark blue). (b) With additional physical insight used to refine the reference model it is possible to tighten the bound (compare dark blue and light blue lines). The green line in (a) is the corrected version of the 6D bound. The boxed region in panel (a) indicates the scale of Fig. 3 of Ref. [55] (not the scale of Fig. 3.3(b)). Error bars for both axes are smaller than the thickness of the lines. 72
- 3.4 Large-deviation rate function $J(a)$ for the number of jumps $1 \rightarrow 0$ per unit time, a , for the 3-state model of Ref. [56]. We compare with the exact answer (black) the bounds produced by reference models in which we control jump times (blue), or jump times and jumps from $0 \rightarrow 1$ (green). Error bars for both axes are smaller than the thickness of the lines. Also shown is the CMP universal activity bound [56], Eq. (3.39) (gray). 75
- 3.5 Large-deviation rate function $J(k)$ for the number of jumps per unit time, k , for the one-dimensional Fredrickson-Andersen model. (a) We compare with the exact answer (black) the bounds produced by reference models in which we control jump times (dark blue) or jump times and the mean up-spin fraction (light blue). Also shown is the CMP universal activity bound [56], Eq. (3.39) (gray). (b) The sum (green) of the bound (produced using a reference model in which we control jump times, mean up-spin fraction, and pair correlations) and the correction matches the exact answer. Error bars for both axes are smaller than the thickness of the lines. 76
- 3.6 Large-deviation rate function $J(k)$ for the number of jumps per unit time, k , for the Fredrickson-Andersen model of Ref. [78] with $c = 0.1$. Lattice sizes are (a) $L = 40$ sites and (b) $L = 100$ sites. We compare the matrix product state (MPS) calculation of Ref. [78] (black) with the three-parameter VARD bound of Fig. 3.5 (blue). Also shown is the CMP universal activity bound [56], Eq. (3.39) (gray). 79

- 4.1 (a–c) Large-deviation functions for the time-averaged position a of a driven discrete random walker on a closed lattice of L sites. (d) Walker trajectories showing the instantaneous position x/L under the biased dynamics corresponding to the point $k = k^*$ of greatest curvature of $\lambda(k)$. These trajectories show intermittency, with the walker switching between two locations on either side of the lattice. The timescale for residence in the distinct lattice locations increases with increasing L . (e) Histograms of the instantaneous position x/L for the trajectories in (d). 91
- 4.2 Analog of Fig. 4.1, now for an undriven walker. (a–c) As for the driven walker, large-deviation functions show increasingly sharp behavior as L increases. (d) Trajectories showing the instantaneous position x/L of the walker at the point of greatest curvature of $\lambda(k)$, $k^* = 0$. These trajectories do not exhibit intermittency. (e) As a result, histograms of the instantaneous position x/L for the trajectories in (d) are unimodal. 93
- 4.3 (a–c) The large-deviation functions of Fig. 4.2 (a–c), rescaled by L^2 to account for the timescale associated with diffusion. The resulting collapse indicates that these systems behave similarly when viewed on the natural timescale T/L^2 . The large-deviation singularity in this case results from divergence of the diffusive timescale. 94
- 4.4 Negative log-probability per unit time for the driven walker to achieve a time-averaged position $a = x/L$ in a homogeneous way (blue lines) or a two-state intermittent way (cyan and red lines). In panel (a) the walker’s driving is constant, $p(x) = 1/4$, while in panel (b) the tendency of the walker to move left increases with rightward distance, $p(x) = [1 - (x/L)^2]/4$. The lattice size $L = 20$. When the straight lines lie below the blue lines it is more likely for the system to achieve the time-averaged position a corresponding to x/L in an intermittent way. This construction is consistent with conditioned trajectories of these models (Fig. 4.5), as long as the trajectory time comfortably exceeds the time on which switching occurs. 96

- 4.5 Large-deviation rate function $I(a)$ for the time-averaged position of the driven lattice random walker from Section 4.2 (red), together with that for a super-driven walker (cyan) for which the probability to move left increases with distance from the left-hand edge. Shown below are histograms of the instantaneous walker position from trajectories of the two models conditioned to produce various atypical values of a . Consistent with the simple arguments developed in this section, the driven walker displays intermittency, for most values of a , involving sites near the edges of the lattice. By contrast, the super-driven walker shows intermittency for a not too far from the typical value a_0 , involving sites near the middle of the lattice. For a far from a_0 , its conditioned trajectories are homogeneous. For both models, $L = 20$. 98
- 4.6 Summary of the biased trajectory ensembles associated with three model systems, each generated at the point k^* at which the SCGF associated with the time-integrated observable has largest curvature. For the undriven walker (left) and the growth model (right) we have $k^* = 0$, while for the driven walker (center) we have $k^* \neq 0$. The top panels show the instantaneous dynamical observable associated with a single trajectory (two trajectories in the case of the growth model). The lower panels show a , the time-integrated version of x , for an ensemble of 100 trajectories. The trajectories of the top panels are indicated in the bottom panels by the dark blue or red lines. . . . 101

- B1 Empirical rate functions $-T^{-1} \ln \rho_T(A)$ for different values of trajectory time T (denoted by symbols) for the irreversible growth model, compared with the steady-state rate function (B1) (black lines). Panels are labeled by values of the parameter J . (a) Far from the critical point $J_c = 1$ the empirical rate functions are convex in the one-phase region ($J < 1$) and concave in the two-phase region ($J > 1$). Close to the critical point the behavior of the model, on the times simulated, is influenced by a population of transient trajectories. (b) Enlargement of the right-hand portion of the plot for $J = 3$ shows the empirical rate function to be consistent with the form (B1), indicating steady-state growth. (c) We again consider the case $J = 1.3$, but now initiate simulations from a pre-made structure of size $T_0 = 1000$ and composition a , consistent with the position of the right-hand minimum of the steady-state rate function (B1). Doing so allows us to effectively access longer timescales than we could from “unassembled” initial conditions. The empirical rate function derived from the resulting ensemble of trajectories is again consistent with the form (B1). 106
- B2 Time-integrated observable a for ensembles of trajectories of the irreversible growth model of Refs. [15, 16]. From left to right we show the one-phase region, the critical point, and the two-phase region. Panels are labeled by the values of the model parameter J . The black lines are derived from (B1). 107
- B3 In the two-phase regime of the growth model, trajectory ensembles begun from structures of increasing size T_0 , having composition $a_0 = 0$ (top row), become increasingly strongly confined by the unstable dynamical attractor at $a = 0$, corresponding to the central minimum of the function (B1). By contrast, large structures of initial composition $a_0 \neq 0$ not consistent with any of the minima are driven toward the stable dynamical attractors (in this figure only, the symbol a_0 denotes initial composition, and not a typical value of the trajectory ensemble.) 107

LIST OF TABLES

<i>Number</i>		<i>Page</i>
2.1	Details of the 2D deposition simulations used to generate Fig. 2.3 in the main text. The first column lists the Damköhler number Da . The second column, R_c runs, indicates the number of runs used to calculate the critical radius. A smaller number of runs listed in the next column, extended runs, were extended in some cases to map out the fractal dimension curve. Finally, the last column indicates whether we used the parallel or serial algorithm.	43
2.2	Descriptions of the 3D simulations used to generate Fig. 2.4 in the main text. The columns are the same as in Table 2.1.	43
3.1	Glossary of frequently-used symbols	55

INTRODUCTION

One of the crowning achievements of equilibrium statistical mechanics is that it can describe any phase transition in terms of a microscopic partition function [1]. Unfortunately, in nonequilibrium systems, the partition function is no longer relevant, even though collective transitions in the behavior of particles remain. For example, imagine a clear stream of water flowing from a faucet spontaneously becoming cloudy with turbulence, or cars on the highway that were speeding along just seconds ago congealing into a traffic jam without any apparent trigger [2, 3]. Consequently, the field of nonequilibrium statistical mechanics seeks to understand these kinds of behaviors without the guiding hand of equilibrium theory. In this thesis, we advance this aim by applying computational methods to characterize two different collective nonequilibrium transitions: the compact-to-dendritic transition in the reactive deposition of Brownian particles (Chapter 2) and trajectory phase coexistence in stochastic dynamical systems (Chapters 3 and 4).

1.1 The Compact-to-Dendritic Transition in Reactive Deposition

The first part of the thesis, consisting of Chapter 2, investigates dendrite formation in reactive deposition. When Brownian particles—like ions, colloids, or misfolded proteins—deposit onto a reactive surface, they do not assemble into a uniform coating [4–6]. Rather, they form fractal branching structures called dendrites. Due to the beauty of these structures and the fact that they can be recreated using simple computer models, studying dendrite formation has long been a fundamental scientific pursuit [7–9]. However, managing dendritic deposition is also critically important in current and next-generation batteries. When dendrites form inside these devices, they consume the working metal and the electrolyte and create catastrophic short circuits [10–12].

One way to understand dendrite formation is by studying the compact-to-dendritic (CTD) transition. This transition occurs when Brownian particles are allowed to deposit from all sides onto the a small reactive seed cluster [13–17]. Initially, the deposition maintains the compact morphology of the seed. However, once the cluster reaches a certain critical radius, it spontaneously forms dendritic branches. This transition is illustrated in Fig. 2.1. Note that the critical radius sets the thickness

of the dendritic branches in the large length-scale morphology.

A fundamental feature of the CTD transition is that the critical radius, and therefore the branch thickness, depends on the deposition conditions [13, 15, 17]. For example, a faster reaction leads to thinner branches. Unfortunately, developing a quantitative theory that describes the critical radius has proven challenging. Continuum modeling suggests that this radius should be proportional to the ratio of the surface reaction rate constant to the diffusion constant [13]. However, Brownian dynamics (BD) simulations of the microscopic evolution of the cluster have not been found to be fully consistent with this behavior [15, 17]. The discrepancy suggests that continuum modeling may be missing a key part of the microscopic dendrite formation dynamics. But this hypothesis is concerning because many studies use similar continuum models to analyze dendritic growth in the literature, particularly in the context of lithium-metal batteries [18–25].

Consequently, to clarify the accuracy of these widely used continuum models, we revisit the discrepancy between the BD simulations and the continuum scale analysis. In particular, we improve on the prior microscopic simulation methodologies in several ways. We adopt an alternative paradigm for the reaction between the particles and the reactive surface that allows us to converge our simulations and to work in terms of experimentally relevant quantities, both of which were previously impossible. We also run larger-scale simulations and investigate the three-dimensional CTD transition for the first time.

1.2 Trajectory Phase Coexistence

The second part of this thesis, consisting of Chapters 3 and 4, investigates a different kind of collective nonequilibrium transition: trajectory phase coexistence (TPC) in stochastic dynamical systems. It is convenient to focus on a prototypical system to introduce this topic. Consider a driven random walker in a box with walls. Each timestep, the walker hops right with probability P_R and left with probability P_L where $P_R > P_L$. Since the walker is driven to the right, its average position \bar{x} over any time T will be close to the right wall of the box. However, the actual value of \bar{x} will vary from measurement to measurement.

While small fluctuations in the average position of the walker follow the central limit theorem, rare “large” fluctuations far out on the tails of the probability distribution cannot be described in this manner [26]. The probability density of these events can instead be framed in the language of the mathematical theory of large deviations.

That is, under a general set of assumptions often satisfied in practice (see [27]), the probability density ρ of measuring a given value χ of a time-averaged observable \bar{x} in a stochastic dynamical system decays exponentially according to

$$\rho(\bar{x} = \chi, T) \sim \exp(-I(\chi)T) \quad (1.1)$$

in the long time limit [26]. Here, the function $I(\chi)$ is called the *rate function* and is non-negative. Rather than working with I directly, it is common to use its Legendre transform instead

$$\lambda(k) = \chi(k)k - I(\chi(k)) \quad (1.2)$$

which encodes equivalent information when I is convex. λ is called the *scaled cumulant generating function* (SCGF).

Eq. (1.1) is fascinating because the rate function I characterizes the probability density of a subset of trajectories (those with $\bar{x} = \chi$) in the same way that the free energy dictates the probability of a subset of configurations in equilibrium statistical mechanics [1]. This connection between equilibrium and nonequilibrium frameworks goes far beyond the surface level. It is, in fact, possible for stochastic dynamical systems to display phase coexistence in trajectory space, much as equilibrium systems display coexistence at the level of configurations [27].

As an example of such coexistence, consider a large fluctuation in the average position of the driven walker. Let us say we want to characterize the probability that we measure \bar{x} to be the middle of the box m . That is, we want to know the value of $I(m)$. To calculate this quantity, we must determine the most likely out of the possible unlikely ways that the system can achieve the given average position over a long time T [26]. The immediately obvious way that the system could realize this average would be for the walker to hop to the middle of the box and remain there for the entire time. Alternatively, the same \bar{x} could result from having the walker spend half of the time on the left side of the box and half of the time on the right side. Amazingly, as shown in Chapter 4, these 50-50 trajectories are the most probable of all possible choices, and consequently, they determine the value of $I(m)$. Such “coexistence” between sections of trajectories that favor each side of the box closely resembles how an Ising strip crystal achieves zero magnetization. Rather than mixing up and down spins uniformly, the crystal forms alternating spin up and spin down sections [28]. In addition, just as the phase transitions in thermodynamic systems are associated with a singularity in the free energy, TPC is associated with a singularity in the SCGF [27, 29–32].

Since TPC often only appears during extremely rare fluctuations, it is natural to ask whether the study of this phenomenon has any practical utility. And many investigations of TPC are indeed motivated exclusively by the drive to develop a nonequilibrium framework that mirrors the beauty of equilibrium statistical mechanics. However, TPC research is far from being completely disconnected from practical concerns. TPC plays a central role in the study of glassy dynamics [33]. Furthermore, studies of TPC can also yield insights into the nature of equilibrium phase transitions [34].

1.3 Sampling the Rate Function

Identifying and characterizing TPC requires sampling the rate function and SCGF [27]. This process introduces technical challenges that are similar to the challenges of calculating free energies in equilibrium systems [35]. Specifically, a brute force calculation of $I(\chi)$ would require generating many trajectories and finding the proportion that achieves $\bar{x} = \chi$. But if χ is far away from its typical value—for example, $\chi = m$, the middle of the box, in the case of the driven walker—then such trajectories will be incredibly rare, and attempting to sample them will be futile.

Instead, a number of enhanced sampling methods have been introduced to calculate the rate function more efficiently [36–41]. These methods commonly evaluate the SCGF directly using

$$\lambda(k) = \lim_{T \rightarrow \infty} \frac{1}{T} \ln \langle \exp(-k\bar{x}T) \rangle. \quad (1.3)$$

Sampling λ is more convenient than sampling I because the average in (1.3) does not have a δ function constraint on the value of the observable. This constraint is implicit in the definition of I in (1.1).

The workhorse method for sampling λ is cloning [36–38]. As the name indicates, cloning involves duplicating trajectories that achieve large values of the weight $\exp(-k\bar{x}T)$. Each time a trajectory is cloned, the stochastic component is reseeded. Consequently, if ten clones are made of a trajectory, these clones will then branch out from the same configurations in many different directions. Trajectories with low values of the weight are also removed (pruned) to keep the total number of trajectories being propagated at any one time, N , constant. The cloning and pruning process, therefore, takes advantage of cumulative self-enhancing small fluctuations of the system to bootstrap to the rare trajectories that contribute maximally to the average in (1.3). Convergence is achieved when increasing the N no longer changes the empirical value of λ .

While cloning has proven effective for sampling large deviations, it has several limitations. To begin with, the method samples the SCGF instead of the rate function. This feature is usually not a problem since λ can often be transformed to get I . However, when I is nonconvex, the equivalence of these two functions breaks down [26]. In addition, the cloning method is highly technical. This has two consequences. First, setting up a cloning calculation is a significant investment. As a result, it is not a great choice for exploratory work that may not yield interesting results. Second, cloning techniques are often unfamiliar to researchers outside of the field, creating a barrier that prevents the study of large deviations and TPC from being taken up more widely.

For these reasons, in Chapter 3, we introduce *Variational Ansatz for Rare Dynamics* (VARD), the latest iteration in a series of large deviation sampling methods based on importance sampling [42–44]. VARD computes the rate function directly, is technically straightforward, and is conceptually familiar since it closely resembles umbrella sampling in equilibrium statistical mechanics [45]. While importance sampling has sometimes been included as part of cloning, previous studies have suggested that it is not powerful enough to calculate large deviations in nontrivial systems on its own [37, 38, 46]. We show, on the contrary, that VARD is capable of sampling the rate function in a number of systems in the literature that have been studied with cloning. As a result, this method provides a previously unrealized balance of efficacy versus implementation effort. Further, VARD can easily be extended with cloning if a higher level of accuracy is needed.

1.4 The Meaning of a Kink in the SCGF

In the last chapter, Chapter 4, we examine the meaning of singularities, specifically kinks, in the SCGF. Kinks are often taken to be proof that TPC occurs. As a result, the search for these singularities plays a central role in the field [27, 47–51]. However, more formal understanding of what creates a kink is lacking. In particular, does a kink in the SCGF always imply TPC and vice-versa?

Answering this question is important conceptually for developing a complete understanding of TPC and practically for ensuring that the current method for locating coexistence is valid. Consequently, we explore the meaning of kink singularities by characterizing the behavior of two different random walkers, the driven random walker introduced in Section 1.2, and an unbiased random walker. Using these systems, we show that kinks are caused by a diverging timescale in the dynamics,

which is often but not always indicative of TPC. Similarly, our analysis suggests that kinks in the free energy in equilibrium statistical mechanics arise due to the divergence of a length scale, a process that is not always linked to a phase transition.

References

1. McQuarrie, D. A. *Statistical Mechanics* 641 pp. ISBN: 978-1-891389-15-3 (University Science Books, Sausalito, Calif, 2000).
2. Avila, K. *et al.* The Onset of Turbulence in Pipe Flow. *Science* **333**, 192–196. <https://www.science.org/doi/10.1126/science.1203223> (July 8, 2011).
3. Chou, T., Mallick, K. & Zia, R. K. P. Non-Equilibrium Statistical Mechanics: From a Paradigmatic Model to Biological Transport. *Reports on Progress in Physics* **74**, 116601. ISSN: 0034-4885. <http://stacks.iop.org/0034-4885/74/i=11/a=116601> (2011).
4. Lin, M. Y. *et al.* Universality in Colloid Aggregation. *Nature* **339**, 360–362. ISSN: 1476-4687. <https://www.nature.com/articles/339360a0> (June 1989).
5. Foderà, V., Zacccone, A., Lattuada, M. & Donald, A. M. Electrostatics Controls the Formation of Amyloid Superstructures in Protein Aggregation. *Physical Review Letters* **111**, 108105. <https://link.aps.org/doi/10.1103/PhysRevLett.111.108105> (Sept. 5, 2013).
6. Kahanda, G. L. M. K. S., Zou, X.-q., Farrell, R. & Wong, P.-z. Columnar Growth and Kinetic Roughening in Electrochemical Deposition. *Physical Review Letters* **68**, 3741–3744. <https://link.aps.org/doi/10.1103/PhysRevLett.68.3741> (June 22, 1992).
7. Mullins, W. W. & Sekerka, R. F. Morphological Stability of a Particle Growing by Diffusion or Heat Flow. *Journal of Applied Physics* **34**, 323–329. ISSN: 0021-8979. <https://aip.scitation.org/doi/abs/10.1063/1.1702607> (Feb. 1, 1963).
8. Witten, T. A. & Sander, L. M. Diffusion-Limited Aggregation, a Kinetic Critical Phenomenon. *Physical Review Letters* **47**, 1400–1403. <https://link.aps.org/doi/10.1103/PhysRevLett.47.1400> (Nov. 9, 1981).
9. Sander, L. M. Diffusion-Limited Aggregation: A Kinetic Critical Phenomenon? *Contemporary Physics* **41**, 203–218. <http://www.tandfonline.com/doi/abs/10.1080/001075100409698> (July 2000).
10. Liu, K., Liu, Y., Lin, D., Pei, A. & Cui, Y. Materials for Lithium-Ion Battery Safety. *Science Advances* **4**, eaas9820. <https://www.science.org/doi/10.1126/sciadv.aas9820> (June 22, 2018).

11. Lin, D., Liu, Y. & Cui, Y. Reviving the Lithium Metal Anode for High-Energy Batteries. *Nature Nanotechnology* **12**, 194–206. ISSN: 1748-3387. <http://www.nature.com/nnano/journal/v12/n3/full/nnano.2017.16.html> (Mar. 2017).
12. Hwang, J.-Y., Myung, S.-T. & Sun, Y.-K. Sodium-Ion Batteries: Present and Future. *Chemical Society Reviews* **46**, 3529–3614. ISSN: 1460-4744. <http://pubs.rsc.org/en/content/articlelanding/2017/cs/c6cs00776g> (June 19, 2017).
13. Witten, T. A. & Sander, L. M. Diffusion-Limited Aggregation. *Physical Review B* **27**, 5686–5697. <https://link.aps.org/doi/10.1103/PhysRevB.27.5686> (May 1, 1983).
14. Meakin, P. Diffusion-Controlled Cluster Formation in 2—6-Dimensional Space. *Physical Review A* **27**, 1495–1507. <https://link.aps.org/doi/10.1103/PhysRevA.27.1495> (Mar. 1, 1983).
15. Meakin, P. Models for Colloidal Aggregation. *Annual Review of Physical Chemistry* **39**, 237–267. ISSN: 0066-426X. <https://www.annualreviews.org/doi/10.1146/annurev.pc.39.100188.001321> (Oct. 1, 1988).
16. Nagatani, T. Laplacian Growth Phenomena with the Third Boundary Condition: Crossover from Dense Structure to Diffusion-Limited Aggregation Fractal. *Physical Review A* **40**, 7286–7291. <https://link.aps.org/doi/10.1103/PhysRevA.40.7286> (Dec. 1, 1989).
17. Halsey, T. C. & Leibig, M. Electrodeposition and Diffusion-limited Aggregation. *The Journal of Chemical Physics* **92**, 3756–3767. ISSN: 0021-9606. <https://aip.scitation.org/doi/abs/10.1063/1.457834> (Mar. 15, 1990).
18. Aogaki, R. Image Analysis of Morphological Instability in Galvanostatic Electrocrystallization: I. General Expression for the Growth Mode of Surface Irregularities. *Journal of The Electrochemical Society* **129**, 2442. ISSN: 1945-7111. <https://iopscience.iop.org/article/10.1149/1.2123563/meta> (Nov. 1, 1982).
19. Sundström, L.-G. & Bark, F. H. On Morphological Instability during Electrodeposition with a Stagnant Binary Electrolyte. *Electrochimica Acta* **40**, 599–614. ISSN: 0013-4686. <http://www.sciencedirect.com/science/article/pii/001346869400379F> (Apr. 1, 1995).
20. Monroe, C. & Newman, J. The Effect of Interfacial Deformation on Electrodeposition Kinetics. *Journal of The Electrochemical Society* **151**, A880. ISSN: 1945-7111. <https://iopscience.iop.org/article/10.1149/1.1710893/meta> (May 4, 2004).

21. Monroe, C. & Newman, J. The Impact of Elastic Deformation on Deposition Kinetics at Lithium/Polymer Interfaces. *Journal of The Electrochemical Society* **152**, A396–A404. ISSN: 0013-4651, 1945-7111. <http://jes.ecsdl.org/content/152/2/A396> (Feb. 1, 2005).
22. Tikekar, M. D., Archer, L. A. & Koch, D. L. Stability Analysis of Electrodeposition across a Structured Electrolyte with Immobilized Anions. *Journal of The Electrochemical Society* **161**, A847–A855. ISSN: 0013-4651, 1945-7111. <https://iopscience.iop.org/article/10.1149/2.085405jes> (2014).
23. Liu, W., Lin, D., Pei, A. & Cui, Y. Stabilizing Lithium Metal Anodes by Uniform Li-Ion Flux Distribution in Nanochannel Confinement. *Journal of the American Chemical Society* **138**, 15443–15450. ISSN: 0002-7863. <https://doi.org/10.1021/jacs.6b08730> (Nov. 30, 2016).
24. Tu, Z. *et al.* Nanoporous Hybrid Electrolytes for High-Energy Batteries Based on Reactive Metal Anodes. *Advanced Energy Materials* **7**, 1602367. ISSN: 1614-6832. <https://onlinelibrary.wiley.com/doi/full/10.1002/aenm.201602367> (Apr. 1, 2017).
25. Choudhury, S. *et al.* Confining Electrodeposition of Metals in Structured Electrolytes. *Proceedings of the National Academy of Sciences* **115**, 6620–6625. ISSN: 0027-8424, 1091-6490. pmid: 29891658. <https://www.pnas.org/content/115/26/6620> (June 26, 2018).
26. Touchette, H. The Large Deviation Approach to Statistical Mechanics. *Physics Reports* **478**, 1–69. ISSN: 03701573. arXiv: 0804.0327. <http://arxiv.org/abs/0804.0327> (July 2009).
27. Jack, R. L. Ergodicity and Large Deviations in Physical Systems with Stochastic Dynamics. *The European Physical Journal B* **93**, 74. ISSN: 1434-6036. <https://doi.org/10.1140/epjb/e2020-100605-3> (Apr. 22, 2020).
28. Jack, R. L., Nemoto, T. & Lecomte, V. Dynamical Phase Coexistence in the Fredrickson-Andersen Model. *Journal of Statistical Mechanics: Theory and Experiment* **2020**, 053204. ISSN: 1742-5468. arXiv: 1912.02465. <http://arxiv.org/abs/1912.02465> (May 28, 2020).
29. Den Hollander, F. *Large Deviations* (American Mathematical Soc., 2008).
30. Touchette, H. The large deviation approach to statistical mechanics. *Physics Reports* **478**, 1–69 (2009).
31. Gallavotti, G. & Cohen, E. G. D. Dynamical ensembles in nonequilibrium statistical mechanics. *Physical Review Letters* **74**, 2694 (1995).
32. Lebowitz, J. L. & Spohn, H. A Gallavotti–Cohen-type symmetry in the large deviation functional for stochastic dynamics. *Journal of Statistical Physics* **95**, 333–365 (1999).

33. Hedges, L. O., Jack, R. L., Garrahan, J. P. & Chandler, D. Dynamic Order-Disorder in Atomistic Models of Structural Glass Formers. *Science* **323**, 1309–1313. ISSN: 0036-8075, 1095-9203. pmid: 19197025. <http://science.sciencemag.org/content/323/5919/1309> (Mar. 6, 2009).
34. Whitelam, S. & Jacobson, D. Varied Phenomenology of Models Displaying Dynamical Large-Deviation Singularities. *Physical Review E* **103**, 032152. <https://link.aps.org/doi/10.1103/PhysRevE.103.032152> (Mar. 29, 2021).
35. Touchette, H. *A Basic Introduction to Large Deviations: Theory, Applications, Simulations* June 21, 2011. <http://arxiv.org/abs/1106.4146>.
36. Giardinà, C., Kurchan, J. & Peliti, L. Direct Evaluation of Large-Deviation Functions. *Physical Review Letters* **96**, 120603. <https://link.aps.org/doi/10.1103/PhysRevLett.96.120603> (Mar. 31, 2006).
37. Nemoto, T., Jack, R. L. & Lecomte, V. Finite-Size Scaling of a First-Order Dynamical Phase Transition: Adaptive Population Dynamics and an Effective Model. *Physical Review Letters* **118**. ISSN: 0031-9007, 1079-7114. <https://link.aps.org/doi/10.1103/PhysRevLett.118.115702> (Mar. 14, 2017).
38. Ray, U., Chan, G. K.-L. & Limmer, D. T. Importance Sampling Large Deviations in Nonequilibrium Steady States. I. *The Journal of Chemical Physics* **148**, 124120. ISSN: 0021-9606. <https://aip.scitation.org/doi/10.1063/1.5003151> (Mar. 28, 2018).
39. Bañuls, M. C. & Garrahan, J. P. Using Matrix Product States to Study the Dynamical Large Deviations of Kinetically Constrained Models. *Physical Review Letters* **123**, 200601. <https://link.aps.org/doi/10.1103/PhysRevLett.123.200601> (Nov. 12, 2019).
40. Das, A. & Limmer, D. T. *Variational Control Forces for Enhanced Sampling of Nonequilibrium Molecular Dynamics Simulations* Sept. 8, 2019. <http://arxiv.org/abs/1909.03589>.
41. Ray, U. & Chan, G. K.-L. *Constructing Auxiliary Dynamics for Nonequilibrium Stationary States with Variational Monte-Carlo* Sept. 25, 2019. <http://arxiv.org/abs/1909.11283>.
42. Klymko, K., Geissler, P. L., Garrahan, J. P. & Whitelam, S. Rare Behavior of Growth Processes via Umbrella Sampling of Trajectories. *Physical Review E* **97**, 032123. <https://link.aps.org/doi/10.1103/PhysRevE.97.032123> (Mar. 19, 2018).
43. Whitelam, S. Multi-Point Nonequilibrium Umbrella Sampling and Associated Fluctuation Relations. *Journal of Statistical Mechanics: Theory and Experiment* **2018**, 063211. ISSN: 1742-5468. <https://doi.org/10.1088/2F1742-5468%2Faac915> (June 2018).

44. Whitelam, S. Sampling Rare Fluctuations of Discrete-Time Markov Chains. *Physical Review E* **97**, 032122. <https://link.aps.org/doi/10.1103/PhysRevE.97.032122> (Mar. 19, 2018).
45. Newman, M. E. J. *Monte Carlo Methods in Statistical Physics* in collab. with Barkema, G. T. xiv+475. ISBN: 978-0-19-851796-2 (Clarendon Press ; Oxford University Press, Oxford : New York, 1999).
46. Warren, P. B. & Allen, R. J. Trajectory Reweighting for Non-Equilibrium Steady States. *Molecular Physics* **116**, 3104–3113. ISSN: 0026-8976. <https://doi.org/10.1080/00268976.2018.1471226> (Nov. 17, 2018).
47. Garrahan, J. P. *et al.* First-order dynamical phase transition in models of glasses: an approach based on ensembles of histories. *Journal of Physics A: Mathematical and Theoretical* **42**, 075007 (2009).
48. Vaikuntanathan, S., Gingrich, T. R. & Geissler, P. L. Dynamic phase transitions in simple driven kinetic networks. *Physical Review E* **89**, 062108 (2014).
49. Nemoto, T., Jack, R. L. & Lecomte, V. Finite-size scaling of a first-order dynamical phase transition: Adaptive population dynamics and an effective model. *Physical Review Letters* **118**, 115702 (2017).
50. Klymko, K., Garrahan, J. P. & Whitelam, S. Similarity of ensembles of trajectories of reversible and irreversible growth processes. *Physical Review E* **96**, 042126 (2017).
51. Klymko, K., Geissler, P. L., Garrahan, J. P. & Whitelam, S. Rare behavior of growth processes via umbrella sampling of trajectories. *Phys. Rev. E* **97**, 032123. <https://link.aps.org/doi/10.1103/PhysRevE.97.032123> (3 Mar. 2018).

Chapter 2

COMPACT-TO-DENDRITIC TRANSITION IN THE REACTIVE DEPOSITION OF BROWNIAN PARTICLES

Jacobson, D. & Miller III, T. F. Compact-to-Dendritic Transition in the Reactive Deposition of Brownian Particles. Version 3. arXiv: 2204.01173 [cond-mat]. <http://arxiv.org/abs/2204.01173> (Apr. 12, 2022)

Chapter Abstract

When Brownian particles—such as ions, colloids, or misfolded proteins—deposit onto a reactive cluster, the cluster undergoes a transition from a compact to a dendritic morphology. Continuum modeling reveals that the critical radius for this compact-to-dendritic (CTD) transition should be proportional to the particle diffusivity divided by the surface reaction rate. However, previous studies have had limited success verifying that the same scaling arises in the continuum limit of a particle-based deposition model. This discrepancy suggests that the continuum model may be missing part of the microscopic dendrite formation mechanism, a concerning hypothesis given that similar models are commonly used to study dendritic growth in electrodeposition and lithium metal batteries. To clarify the accuracy of such models, we reexamine the particle-based CTD transition using larger system sizes, up to hundreds of millions of particles in some cases, and an improved paradigm for the surface reaction. Specifically, this paradigm allows us to converge our simulations and to work in terms of experimentally accessible parameters. With these methods, we show that in both two and three dimensions, the behavior of the critical radius is consistent with the scaling of the continuum model. Our results help unify the particle-based and continuum views of the CTD transition. In each of these cases, dendrites emerge when particles can no longer diffuse around the cluster within the characteristic reaction timescale. Consequently, this work implies that continuum methods can effectively capture the microscopic physics of dendritic deposition.

2.1 Introduction

Many systems that display dendritic growth consist of diffusive particles that deposit onto a reactive surface. Examples include colloidal aggregation, amyloid formation,

and electrodeposition [1–3]. One way to understand these systems is by studying idealized models of reactive deposition [4–9]. These models show that dendrites emerge due to a feedback loop. Incoming particles preferentially attach to the bumps of a reactive surface before they have time to diffuse into the valleys [4, 10]. The preferential deposition causes the bumps to grow faster than the rest of the surface, which exacerbates the preferential deposition, and so on.

In idealized models, the dendritic feedback loop also produces a deeper phenomenology. The thickness of the dendritic branches decreases as the rate of the surface reaction increases [4, 9]. This relationship is significant because it qualitatively matches what is observed in electrodeposition experiments [3]. Understanding branch thickness in idealized models can thus help clarify the mechanism of dendrite formation in a number of electrodeposition-based applications like batteries. Currently, dendrite formation in lithium-ion and next-generation alkali metal batteries is one of the primary sources of cell failure as it can deplete the working metal and the electrolyte, and create catastrophic short circuits [11–13].

In this work, we investigate the factors that determine dendritic branch thickness in idealized models specifically through the lens of the compact-to-dendritic (CTD) transition. This transition occurs when a small, compact cluster is embedded in a concentration field of reactive particles that cause it to grow outwards in all directions [4–8]. While at first, the cluster continues to display a compact morphology, upon reaching a critical radius, it splits into a characteristic dendritic pattern¹. Illustrations of the growth process for two and three-dimensional deposition are shown in Fig. 2.1. Since the critical radius sets the resulting dendritic branch thickness, the CTD transition offers a convenient way to study the branch structure of the large length-scale dendritic morphology.

Unfortunately, understanding this transition has proven to be challenging. Previous studies attempted to analyze the growing cluster by comparing the behavior of two related models of the deposition dynamics, a discrete model and a continuum model [4]. These models differ based on how they represent the concentration field that surrounds the cluster. In the discrete model, particles in the field are represented explicitly, and the cluster grows particle-by-particle. In contrast, in the continuum model, the concentration field itself is taken to be fundamental. Instead of growing

¹Meakin suggested that the initial phase of compact deposition is linked to Eden growth, reasoning that, when the cluster is small enough, incoming particles equilibrate with its surface and become equally likely to deposit everywhere [14, 15].

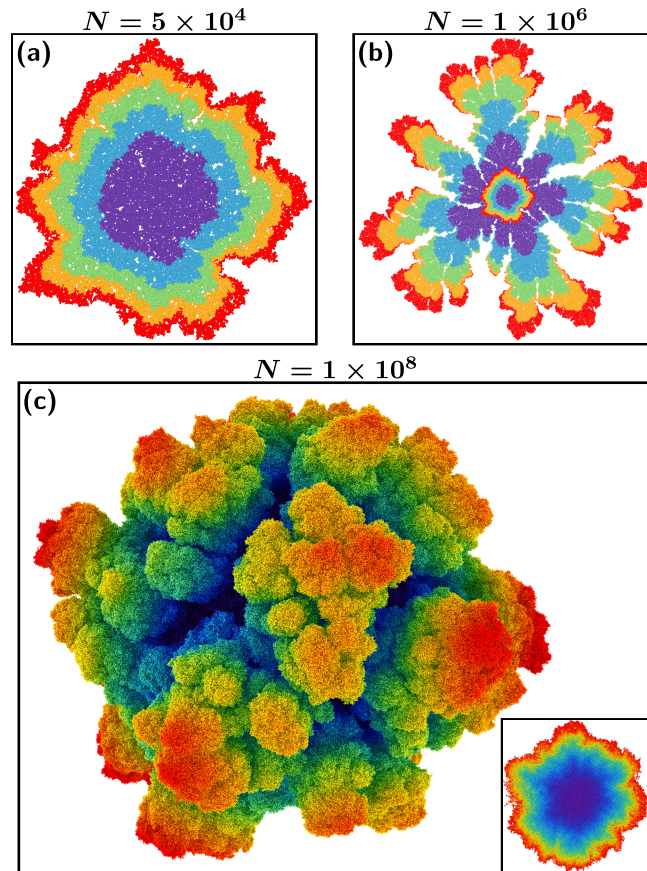


Figure 2.1: The compact-to-dendritic transition for discrete deposition at $\log_{10} \text{Da} = -2.12$. Panels (a) and (b) illustrate the two-dimensional deposition process. The N particles in these panels are rendered with a radius twice that of the actual radius for clarity. The i th band of color moving outwards from the center corresponds to the structure after $iN/5$ particles have been deposited. (a) Initially, the cluster displays a compact morphology. (b) However, upon reaching a critical radius, it spontaneously forms dendritic branches. (c) During three-dimensional deposition, a similar dendritic morphology emerges at large length scales. Here, particles are colored based on their distance from the origin. The inset shows a two-dimensional slice through the initial compact cluster, $N = 1 \times 10^6$, with a continuous gradient color scheme based on the deposition order.

particle-by-particle, the cluster grows outwards at all points simultaneously with a velocity proportional to the continuum flux.

The CTD transition in the continuum model can be treated analytically. A linear stability analysis reveals that for two and three-dimensional growth, the critical radius R_c scales as

$$R_c \sim D/k, \quad (2.1)$$

where D is the diffusion constant and k is the surface reaction rate constant² [4, 16]. We will show that D/k scaling is associated with a simple dendrite formation mechanism.

In comparison, the CTD transition in the discrete model is significantly more difficult to characterize. The behavior of this transition depends on the parameters of the deposition process through the dimensionless Damköhler number

$$\text{Da} = \frac{ka}{D}, \quad (2.2)$$

where a is the particle radius. Physically, Da quantifies the relative rate of reaction versus diffusion in the system. In the limit as the reaction becomes infinitely fast, $\text{Da} \rightarrow \infty$, the model approaches diffusion-limited aggregation (DLA). That is, particles begin to deposit as soon as they touch the cluster [4, 17]. As a result, the critical radius for the CTD transition tends towards zero, and the cluster immediately forms dendritic branches that are a single particle thick.

The limit $\text{Da} \rightarrow 0$, in contrast, yields a nontrivial critical radius. This limit corresponds to making the surface reaction infinitely slow. Alternatively, $\text{Da} \rightarrow 0$ can be thought of as the continuum limit since it can be reached by taking the particle radius a to zero at fixed values of k and D . In either view, when $\text{Da} \rightarrow 0$, R_c is expected to converge to the following power-law form based on dimensional analysis³ [18]

$$\frac{kR_c}{D} \sim \text{Da}^\gamma. \quad (2.3)$$

Here, γ is an unknown scaling exponent that encodes the mechanistic details of CTD transition. This exponent plays a central role in the rest of this article.

Due to its mechanistic importance, a number of authors have previously analyzed γ [4, 6, 8]. In particular, Witten and Sander hypothesized that the continuum limit of

²See also Sec. 2.7.

³Choosing to nondimensionalize the critical radius by the particle radius a provides a different, though equivalent, scaling relationship [4, 6, 8].

the *discrete model* (2.3) should reproduce the D/k scaling of the *continuum model* (2.1) [4]. Their reasoning implies that, in two and three dimensions, γ should be equal to zero.

However, the $\gamma = 0$ hypothesis has received only limited empirical support. Refs. [6] and [8] calculated γ using lattice-based and off-lattice 2D Brownian dynamics simulations and obtained estimates of -0.2 and -0.25 ± 0.3 , respectively⁴. In the latter case, $\gamma = 0$ is included at the edge of the error bars, so at a minimum, the Witten and Sander hypothesis cannot be ruled out. But taken together, these two results suggest a power-law divergence with $\gamma \approx -0.2$.

The lack of agreement between the hypothesized value of γ and the value calculated from simulations is significant for three reasons. To begin with, the evidence that $\gamma \neq 0$ suggests that the continuum model might be missing part of the microscopic dendrite formation mechanism. This potential limitation is particularly concerning because similar continuum models have been widely used to study dendrite prevention strategies in lithium metal batteries and other electrodeposition applications [19–26]. From a theoretical perspective, the value of γ also determines the behavior of the discrete model’s own continuum limit. If $\gamma = 0$, then this limit is well-defined. Once the particle radius is small enough, its exact value no longer has any impact on the critical radius. Conversely, if $\gamma \neq 0$, the continuum limit is not physically meaningful. The critical radius either diverges for $\gamma < 0$, or goes to zero for $\gamma > 0$. The apparent absence of a well-defined continuum limit in the discrete model has previously led some authors to explore this limit by instead representing deposition as a random sequence of conformal maps [27]. Finally, the disagreement between the discrete and continuum descriptions of the CTD transition has prevented both of these models from being widely embraced experimentally. Neither one has been tested against the branch thickness phenomenology of real systems.

Given the importance of γ for understanding dendrite formation across the microscopic and continuum scales, here, we reexamine this quantity using an updated Brownian dynamics simulation approach. We improve on past simulation studies in four ways. First, we use a corrected simulation algorithm [16, 28]. Fixing the probability that the particle deposits onto the cluster upon contact, as is standard, makes achieving timestep convergence impossible [8, 9]. Instead, the sticking probability must be a function of the timestep. Second, we carefully evaluate the convergence of γ as the Damköhler number is taken to zero. Third, we examine the CTD transition

⁴See also Sections 2.3 and 2.9.

in two dimensions at much smaller values of the Damköhler number than those used to study the continuum limit in previous work [6, 8]. As part of this process, we generate clusters containing hundreds of millions of particles, orders of magnitude larger than the largest cluster sizes reported so far. Finally, we also investigate, for the first time, the scaling of the CTD transition in three dimensions.

Apart from the simulation-based study of γ , this article contains three additional contributions. The first is that we review the literature relating to the CTD transition. The second is that we reorganize this literature into a unified framework based on the Damköhler number introduced in (2.2). Previously, the sticking probability in the Brownian dynamics algorithm was used in place of Da because it was taken to be a fundamental physical parameter [4–8, 15]. However, the sticking probability is actually a convergence parameter akin to the simulation timestep [16, 28]. The third contribution is that we show the D/k scaling of the continuum model, (2.1), has a simple physical interpretation.

The rest of this work is organized as follows. First, in Sec. 2.2, we define the discrete and continuum growth models. Next, in Sec. 2.3, we describe our Brownian dynamics algorithm for simulating the discrete model and detail our methods for calculating the exponent γ . Finally, in Sec. 2.4, we evaluate γ based on simulation data and discuss how our results compare to the hypothesis that $\gamma = 0$.

2.2 Model Definitions

We begin by defining the discrete and continuum reactive deposition models. The discrete model represents the dynamics of the diffusive particles reacting with the cluster explicitly and is the main focus of this work. In contrast, the continuum model coarse-grains the particle dynamics as a concentration field and is included for comparison.

In the discrete model, the cluster is initially composed of a single reactive particle with radius a , fixed at the origin [4]. A diffusive particle, also with radius a , is launched from a random point on a circle (or a sphere in 3D) with radius b that surrounds the cluster. After the diffusive particle deposits, another particle is launched, and the process repeats. The launching surface is destructive. If the diffusive particle ever returns to this surface, it is killed, and a new particle is introduced. Finally, the launching radius b is assumed to be very large; that is, we take the limit $b \rightarrow \infty$ (details of how this limit is handled in simulations can be found in Sec. 2.8).

Before formalizing these dynamics, we simplify the excluded volume interaction. Specifically, we treat the incoming particle as a point particle and double the radii of the particles that compose the cluster, generating what we term the “supercluster.”

The deposition process in the model is defined by the growth probability density $\rho(\mathbf{w})$, the probability density that the incoming particle attaches to the supercluster boundary at the point \mathbf{w} . $\rho(\mathbf{w})$ can be expressed in terms of a steady-state concentration field C using the standard Laplacian growth framework [29, 30]. Following this approach, the field $C(\mathbf{x})$ (for position \mathbf{x}) satisfies Laplace’s equation

$$\nabla^2 C = 0 \quad (2.4)$$

on the domain outside of the supercluster boundary and inside the launching radius. The launching circle or sphere becomes a particle bath with an arbitrary, fixed concentration C_0

$$C(|\mathbf{x}| = b) = C_0. \quad (2.5)$$

And lastly, the reactivity of the supercluster at a point \mathbf{w} is included with the boundary condition

$$D\nabla C(\mathbf{w}) \cdot \mathbf{n}(\mathbf{w}) = kC(\mathbf{w}). \quad (2.6)$$

Here, \mathbf{n} is the outward unit normal, D is the diffusivity of the incoming particle, and k is the reaction rate constant. Note that k is a surface rate constant, and so has units of velocity. The growth probability density $\rho(\mathbf{w})$ is then proportional to the flux

$$\rho(\mathbf{w}) \propto \nabla C(\mathbf{w}) \cdot \mathbf{n}(\mathbf{w}). \quad (2.7)$$

The discrete model specified by (2.7) has three dimensional parameters k , a , and D . These parameters combine to form the Damköhler number, Da in (2.2). The value of Da sets the ratio of the reaction and diffusion rates in the system. In addition, since it is the only dimensionless quantity, Da uniquely determines the growth dynamics.

The continuum growth model is similar to the Laplacian growth framing of the discrete model in that it consists of a reactive cluster, a bath, and a concentration field [4]. However, the concentration field C is taken to be fundamental instead of being introduced only as a means of calculating the behavior of discrete particles. This feature leads to two changes. First, in the continuum model, the cluster is a closed curve (or a surface in 3D) rather than a collection of particles. Second, the cluster grows outward at every point along the unit surface normal \mathbf{n} simultaneously

as opposed to growing one particle at a time. Specifically, the growth velocity of a point on the boundary $v(\mathbf{w})$ is set by the flux

$$v(\mathbf{w}) = \mu D \nabla C(\mathbf{w}) \cdot \mathbf{n}(\mathbf{w}). \quad (2.8)$$

The constant of proportionality in this equation, μ , is taken to be small enough that C is pseudosteady. As a result, C is described by the same set of equations, (2.4)-(2.6), as in the discrete model.

2.3 Theory and Methods

Brownian Dynamics Algorithm

Propagating the growth dynamics of the discrete model involves repeatedly sampling the growth probability density $\rho(\mathbf{w})$, defined in (2.7), and attaching a new particle to the cluster at the selected point. We obtain these samples by simulating the motion of the incoming particle directly using the specialized Brownian dynamics algorithm from Refs. [16] and [28]. In this subsection, we provide an overview of the unusual features of this algorithm. Further technical details of our simulations can be found in Sec. 2.8.

The Brownian dynamics algorithm functions as follows. Each timestep, the position of the incoming particle is updated using a Gaussian displacement as in standard methods [31]. If the particle makes contact with the cluster during the update, it deposits with a given sticking probability P [4, 15]. Otherwise, it reflects off of the cluster surface.

This algorithm is unusual for two reasons. First, we would like to simulate discrete deposition for a given value of the rate constant k . However, k does not appear in the operational parameters of the algorithm, which include the particle radius a , the diffusion constant D , the timestep Δt , and the sticking probability P . Rather, the value of k is set implicitly by the values of these other parameters. The second reason the algorithm is unusual is that the implicit equation for k includes the timestep. Specifically, we have [16, 28]

$$k = P \sqrt{\frac{D}{\pi \Delta t}}. \quad (2.9)$$

Eq. (2.9) implies that we must approach timestep convergence carefully. We still need to take the limit $\Delta t \rightarrow 0$ to converge any observables of interest calculated from the simulations. But taking this limit for a fixed value of the sticking probability P will cause k to diverge. Instead, to keep k constant, we need to take the timestep and

the sticking probability to zero simultaneously such that the ratio $P/\sqrt{\Delta t}$ is fixed. In other words, to simulate a given k value, we must always set

$$P = k\sqrt{\frac{\pi\Delta t}{D}} \quad (2.10)$$

as we take $\Delta t \rightarrow 0$. For this reason, the sticking probability is effectively a convergence parameter like the timestep rather than a physical parameter like the rate constant.

We verified the timestep convergence of our simulations by evaluating the critical radius (defined in Sec. 2.3) at various values of the Damköhler number. More information about this procedure can be found in Sec. 2.8.

Toy Model: A Brownian Particle in a One-Dimensional Box with Reactive Walls

Since the convergence behavior of the Brownian dynamics algorithm is counterintuitive, we illustrate it here with a toy example. Consider a Brownian point particle initialized at a random position in a one-dimensional box of length L . The left wall of the box, wall A , is reactive with surface rate constant k_A , while the right wall of the box, wall B , is absorbing (or equivalently $k_B = \infty$). After nondimensionalizing with L and the diffusion constant D , the probability density of the particle ξ as a function of position y and time τ is described by

$$\begin{aligned} \partial_\tau \xi &= \partial_{yy} \xi, \\ \partial_y \xi(0, \tau) &= \psi_A \xi(0, \tau), \\ \xi(1, \tau) &= 0, \\ \xi(y, 0) &= 1. \end{aligned} \quad (2.11)$$

Here, $\psi_A = k_A L/D$ is a dimensionless rate constant similar to the Damköhler number in the discrete deposition model.

For this toy system, we focus on the effect of the timestep on the probability that the particle will react with wall A on the left, Φ_A . This quantity can be calculated analytically as follows. First, we integrate (2.11) and define $\Xi = \int_0^\infty \xi d\tau$ yielding

$$\begin{aligned} \Xi''(y) &= -1 \\ \Xi'(0) &= \psi_A \Xi(0), \\ \Xi(1) &= 0. \end{aligned} \quad (2.12)$$

Φ_A is then equal to the integrated flux

$$\Phi_A = \int_0^\infty \partial_y \xi(0, \tau) d\tau = \Xi'(0) = \frac{\psi_A/2}{1 + \psi_A}. \quad (2.13)$$

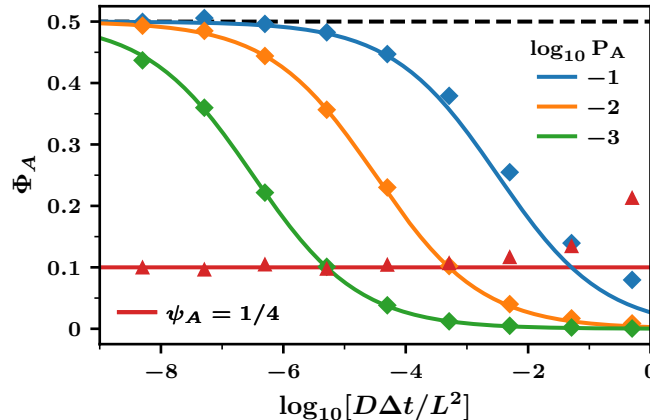


Figure 2.2: The probability that the Brownian particle reacts with wall A , Φ_A , for various values of the timestep Δt . Red triangles correspond to simulations run at $\psi_A = 1/4$ where the sticking probability at wall A , P_A , varies according to (2.10). As $\Delta t \rightarrow 0$, these simulations approach the analytical result from (2.13), $\Phi_A = 1/10$ (red horizontal line). In contrast, the blue, orange, and green diamonds were generated from simulations that used the fixed values of the sticking probability indicated in the upper-right legend. As $\Delta t \rightarrow 0$, these data approach $\Phi_A = 1/2$ (black-dashed line), the infinitely fast reaction limit, following the predictions of (2.9) and (2.13) (blue, orange, and green curves). All numerical data points were generated using 10^4 samples. Error bars constructed from Wald confidence intervals are smaller than the symbols [32].

When the rate constant ψ_A goes to infinity, we find $\Phi_A \rightarrow 1/2$ as expected from symmetry.

In Fig. 2.2, we demonstrate the convergence behavior of the Brownian dynamics algorithm by comparing Φ_A in simulations run with variable and fixed values of P_A , the sticking probability at wall A . This figure clearly shows that only a variable sticking probability, (2.10), is consistent with the goal of simulating a fixed rate constant in reactive deposition. The simulations run with this method at $\psi_A = 1/4$ (red triangles) approach the analytical solution $\Phi_A = 1/10$ from (2.13) (red line) as $\Delta t \rightarrow 0$. In contrast, as predicted by (2.9), the fixed sticking probability simulations (blue, orange, and green diamonds) all converge to the infinitely fast reaction result, $1/2$, (black-dashed line) in the limit $\Delta t \rightarrow 0$.

Previous Studies Treated the Sticking Probability as a Physical Parameter

We now compare our conceptual framework for discrete reactive deposition, which is based on the Damköhler number, with the approach used by previous authors, which is based on the sticking probability. In particular, we focus on off-lattice

deposition, where the particles move in continuous space. Many authors instead studied lattice-based systems which we discuss in Sec. 2.9 [4, 6].

Prior studies considered the sticking probability P to be a fundamental physical parameter of the system that controlled the surface reaction rate rather than a convergence parameter like Δt [8, 9, 33]. This view of the sticking probability appeared to be borne out in simulations where different fixed values of P were found to generate different cluster morphologies [8, 9]. Consequently, Halsey and Leibig proposed that the critical radius for the CTD transition should scale as a power law with P in the limit $P \rightarrow 0$ and attempted to use simulations to calculate the associated exponent [8].

Eq. (2.9) and Fig. 2.2, however, illustrate that treating the sticking probability as a normal physical parameter has a number of conceptual limitations. In particular, all fixed values of P yield the same infinitely fast reaction dynamics in the limit $\Delta t \rightarrow 0$. The reason different P values previously seemed to produce different cluster morphologies in simulations was due to the incomplete timestep convergence [8, 9]. In addition, since for any constant P , the morphology always crosses over immediately to fractal growth, examining the behavior of the critical radius in the limit as $P \rightarrow 0$ is not physically meaningful.

To resolve these issues, we can recast the simulation results of prior studies into the rate constant-based framework we have introduced here. Since these studies happened to use the same timestep for all of their simulations, the effective rate constant k being simulated, (2.9), is always directly proportional to the sticking probability P [8, 9]. Consequently, the figures and calculations in these references can be adapted to our framework if the appropriate value of the Damköhler number is substituted for each value of P . For example, Halsey and Leibig's estimate of the power-law scaling exponent of the critical radius in terms of the sticking probability can instead be taken as an estimate for the exponent γ in (2.3), yielding $\gamma = -0.25 \pm 0.3^5$ [8].

There is, however, one caveat with the conversion procedure. After the sticking probability is replaced with the Damköhler number, the simulation results cannot be assumed to be converged with respect to the timestep. That is, the only way to guarantee Δt convergence to a finite rate constant is to follow the prescription of (2.9) and take Δt and P to zero at the same time. But previous authors instead

⁵Ref. [15] states that Halsey and Leibig's result in Ref. [8] is consistent with $\gamma = 0.2$ instead of $\gamma = -0.25$. However, we believe this is in error based on Eq. 3.4 in the original reference.

always treated P as a fixed quantity [8, 9]. Nevertheless, the values of Δt these authors happened to choose are comparable to the value of Δt we selected for our simulations in this work based on the rigorous convergence procedure described in Sec. 2.8. Consequently, these studies' P to Da converted results are likely free of significant timestep-related artifacts.

The Reaction-Diffusion Length D/k

The ratio of the diffusion constant to the reaction rate constant D/k plays a significant role in the CTD transition. As a reminder, in the continuum model, (2.1), we have $R_c \sim D/k$ directly, and in the discrete model, (2.3), we have $R_c \sim D/k$ in the continuum limit if $\gamma = 0$. In this section, we show how the Brownian dynamics algorithm helps to clarify the physical meaning of this length scale, offering a new view of the CTD transition.

The Brownian dynamics algorithm implies that one of the key physical parameters in the simulation is the ratio of the sticking probability and the square root of the timestep. This ratio defines a new microscopic rate constant κ

$$\kappa = \frac{P}{\sqrt{\Delta t}} = k \sqrt{\frac{\pi}{D}} \quad (2.14)$$

that can be used in place of the macroscopic rate constant k [16, 28].

Thinking in terms of κ is helpful for understanding the ratio D/k . Specifically, since it has units of reciprocal square root of time, κ clearly indicates that the timescale for the surface reaction T is

$$T \sim 1/\kappa^2 \sim D/k^2. \quad (2.15)$$

The definition of T is not immediately apparent based on the macroscopic view of the system since if we start from the macroscopic rate constant k , we find both a/k and D/k^2 have units of time. Based on (2.15), we can see that the ratio D/k is the length a particle can diffuse in the characteristic reaction timescale

$$\sqrt{DT} \sim D/k. \quad (2.16)$$

Consequently, we call this quantity the ‘‘reaction-diffusion length.’’

Using the reaction-diffusion length, we can propose a new mechanistic interpretation of the CTD transition. Specifically, D/k scaling of the critical radius implies that dendritic growth initiates when particles can no longer diffuse around the circumference of the cluster within the characteristic reaction timescale. This mechanism

helps explain dendrite formation in the continuum model where $R_c \sim D/k$. However, critically, it also applies to the discrete model if $\gamma = 0$. If instead, $\gamma \neq 0$, the discrete CTD transition must result from some other physical process that the continuum perspective fails to adequately capture. Consequently, determining the value of γ is paramount for advancing understanding of dendritic growth and for potentially unifying this understanding across the discrete and continuum scales.

The Critical Radius R_c

In this subsection, we define the critical radius quantitatively so that it can be calculated in simulations. The definition we use is posed in terms of the instantaneous fractal dimension of the cluster

$$\mathcal{D}_F = \frac{d \log_{10} N}{d \log_{10}(kR_g/D)}. \quad (2.17)$$

Here, N is the number of particles in the cluster, and R_g is the cluster's radius of gyration. For compact growth, \mathcal{D}_F approaches the dimension of the space d after initial transients decay. In contrast, for dendritic growth, \mathcal{D}_F plateaus at a characteristic value less than d , once again after initial transient behavior. The value of \mathcal{D}_F in this dendritic regime has empirically been found to be 1.71 in 2D and 2.51 in 3D independent of the value of Da [6, 8, 34]. As a result of the two plateaus, plots of the fractal dimension versus the log of the cluster radius, such as Fig. 2.3(a), are roughly sigmoidal.

Based on this behavior, we take the critical radius, R_c , to be the x-value on the fractal dimension curve with the most negative slope

$$R_c = \operatorname{argmin}_{R_g} \frac{d\mathcal{D}_F}{d \log_{10}(kR_g/D)}. \quad (2.18)$$

We evaluate (2.18) using simulation data by first calculating fractal dimension and its derivative with finite difference. We then apply cubic splines to fit the resulting data before taking the argmin.

Calculating the Critical Radius Scaling Exponent γ

We now describe how we calculate the critical radius scaling exponent γ from simulation data and contrast our approach with the one taken by previous authors. We compute γ by finding the slope of a log-log plot of the critical radius versus the Damköhler number in the limit as the latter goes to zero. While conceptually straightforward, this method requires evaluating the critical radius at very small

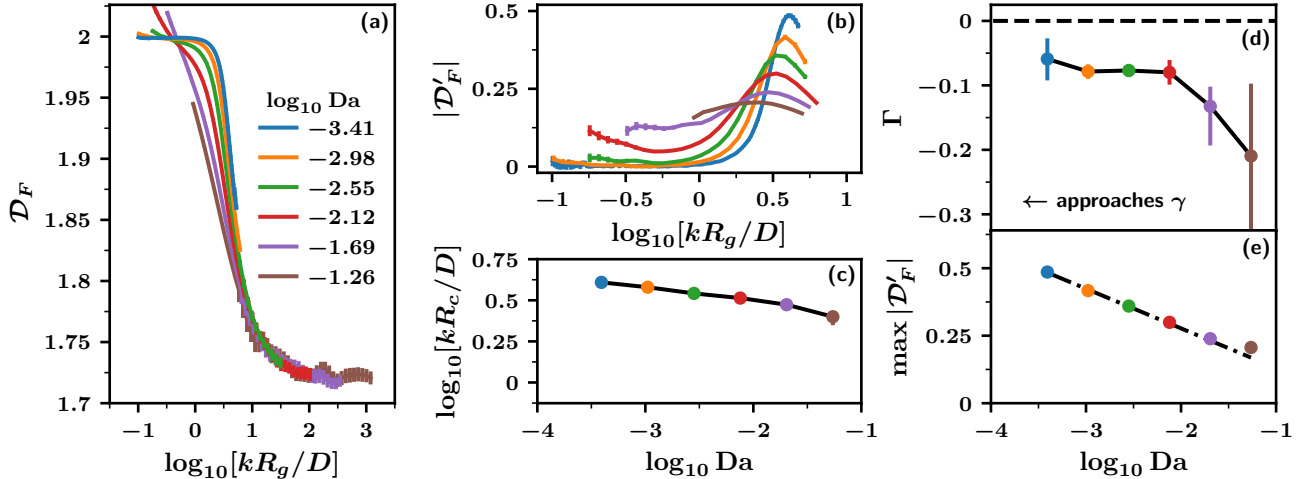


Figure 2.3: Continuum limit scaling analysis of the compact-to-dendritic transition in two dimensions. All error bars are bootstrapped 95% confidence intervals (CI) and are sometimes smaller than the lines or symbols. See Table 2.1 for further trajectory details. (a) The fractal dimension \mathcal{D}_F versus the radius of gyration R_g for various values of the Damköhler number, Da . (b) Absolute value of the derivative of the fractal dimension $|\mathcal{D}'_F|$. The peaks define the critical radius at each value of Da , see (2.18). (c) The critical radius R_c as a function of Damköhler number. (d) The derivative of panel (c), Γ , which provides an estimate for the scaling exponent γ in (2.3) as $\text{Da} \rightarrow 0$. The leftmost (blue) point has a value of -0.06 with a 95%CI of $[-0.03, -0.09]$. At the top of the panel, the black dashed line represents the hypothesis that $\gamma = 0$. (e) The maximum value of $|\mathcal{D}'_F|$ (or equivalently $|\mathcal{D}'_F|$ evaluated at critical radius) versus the Damköhler number. A linear fit to the three points with the lowest Da values (dash-dot black line) has a slope of -0.15 with a 95%CI of $[-0.16, -0.14]$.

values of Da . This procedure is computationally challenging for two reasons. First, as Da gets smaller, an increasing number of particles are needed to observe the fractal transition, especially in 3D. N_c , the number of particles in a d dimensional critical cluster, scales as

$$N_c \sim (R_c/a)^d \sim \text{Da}^{d(\gamma-1)}, \quad (2.19)$$

and based on analyses so far, it is clear $\gamma < 1$ [6, 8]. Second, since Da is proportional to the sticking probability in (2.10), the smaller its value, the longer it takes each particle to deposit in terms of computational steps.

As described in Sec. 2.8, we used a parallel Brownian dynamics algorithm to help partially alleviate these two problems. However, calculating γ still required substantial computational effort because the goal was always to probe deeper into the continuum limit, $\text{Da} \rightarrow 0$. In the end, we used large-scale simulations to examine Da

values where the critical clusters in 2D and 3D contained several hundred million particles, orders of magnitude more particles than the largest reactive deposition clusters generated previously [6, 8].

Authors of prior studies calculated γ using an alternative strategy. Rather than computing the critical radius directly, these authors instead determined γ by exploiting data collapse⁶ [6, 8]. As an example of this approach, consider the relationship between the fractal dimension and the cluster radius in nondimensional form

$$\mathcal{D}_F = f\left(\frac{kR_g}{D}, \text{Da}\right). \quad (2.20)$$

Taking the continuum limit and using the fact that the cluster starts off compact, $\mathcal{D}_F = 2$, yields

$$\mathcal{D}_F = g\left(\frac{kR_g}{\text{Da}^\gamma D}\right), \quad (2.21)$$

where the factor Da^γ is associated with the critical radius [18]. As a result, it is possible to evaluate γ by probing the collapse of the fractal dimension data in the low Da limit.

However, such collapse-based methods have several limitations. To begin with, quantitatively characterizing the extent of a collapse is not straightforward. Previous authors instead estimated γ by judging each potential collapse by eye [6, 8]. In addition, equations such as (2.21) only apply if the Damköhler number is small enough. Consequently, it is necessary to leave out the highest Da value, then the next highest Da value, and so on, to assess convergence. Previous authors, however, did not investigate convergence in a systematic matter [6, 8]. Finally, checking for a collapse is susceptible to bias if only partial data is available. For example, at certain values of Da , we often cannot generate large enough clusters to see the full fractal plateau. Running a collapse calculation on such data would artificially add weight to the initial compact piece of the curve that we can successfully compute.

In contrast, directly measuring the critical radius provides a simple way to calculate γ and evaluate convergence. All that is necessary is to examine a log-log plot of R_c versus Da . Further, direct measurement also avoids introducing any bias due to partial data.

⁶Meakin in Ref. [6] actually estimated the equivalent lattice-based scaling exponent ν instead of γ , see Sec. 2.9. However, the same data collapse method was used for this ν calculation.

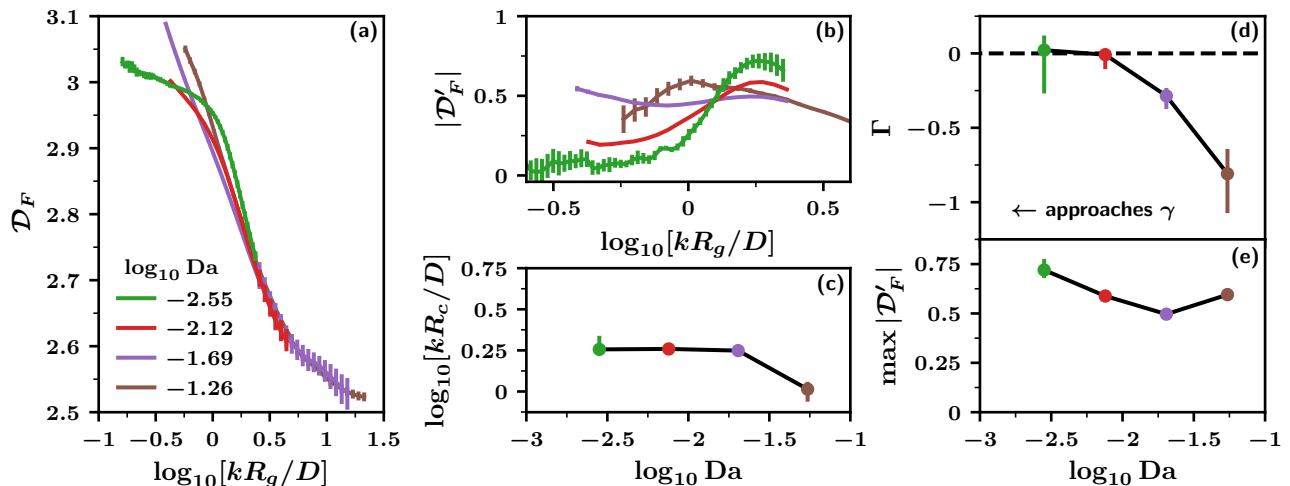


Figure 2.4: Continuum limit scaling of the compact-to-dendritic transition in three dimensions. Panel axis labels are the same as in Fig. 2.3, but note the difference in scale between panel (d) and Fig. 2.3(d). The repeated caption is provide for convenience. See Table 2.2 for further trajectory details. (a) Fractal dimension \mathcal{D}_F as a function of the radius of gyration R_g for different Damköhler numbers, Da . (b) The absolute value of the derivative of panel (a), $|\mathcal{D}'_F|$. (c) The critical radius R_c versus Da . (d) Derivative of the log of the critical radius with respect to the log of the Damköhler number, Γ . The black dashed line corresponds to the $\gamma = 0$ hypothesis. (e) Height of the peak in panel (b), $\max |\mathcal{D}'_F|$, versus the Damköhler number.

2.4 Results and Discussion

In this section, we present the results of our two and three-dimensional Brownian dynamics simulations and evaluate whether these results are consistent with the $\gamma = 0$ hypothesis. We also explore the sharpening of the CTD transition in the continuum limit, a feature of the system that resembles the finite-size scaling of an equilibrium phase transition.

Simulation results for two-dimensional deposition are shown in Fig. 2.3. Panel (a) exhibits the characteristic sigmoidal shape of the fractal dimension as a function of the cluster radius. At smaller values of the Damköhler number, the fractal transition occurs when the cluster has very few particles. For this reason, the plateau at $\mathcal{D}_F = 2$ due to compact growth is not yet fully visible. The lack of this compact plateau makes calculating the critical radius impossible at $\log_{10} Da$ values larger than -1.26 . Panel (a) also provides further evidence that the fractal dimension of 2D dendritic growth is approximately 1.71 independent of the value of Da [6, 8].

From Fig. 2.3(a), we can calculate the critical radius, (2.18), and evaluate its behavior

in the continuum limit. Fig. 2.3(b) shows the magnitude of the derivative of the fractal dimension. The peaks on this panel define the critical radius R_c for each Da . Plotting these R_c values directly in Fig. 2.3(c) shows that the critical radius increases as the Damköhler number gets smaller. To find the exponent γ , in panel (d) we compute the derivative $\Gamma = \frac{d \log_{10}[kR_c/D]}{d \log_{10} Da}$ which converges to γ in the limit $Da \rightarrow 0$. We find that this derivative gets closer to zero as Da gets smaller. Further, taking the leftmost point on the curve (blue) to approximate γ yields an estimate of -0.06 with a 95%CI of $[-0.09, -0.03]$.

The confidence interval for γ must be interpreted carefully in relation to the $\gamma = 0$ hypothesis. In particular, this interval does not include zero. The remaining discrepancy can be explained by the magnitude of the Damköhler number. That is, for smaller values of Da , Γ might follow the trend in Fig. 2.3(d) and move closer to zero. But this trend is not robust. The bottom of the confidence interval for the blue point, -0.09 , may instead indicate that the final part of the upwards drift in the data is a numerical artifact covering an underlying plateau at a value of around -0.1 . Such a plateau would be consistent with the position of the preceding orange, green, and red points.

In spite of this concern about the trend in Γ , we can draw two conclusions from the results of the 2D simulations. First, previous studies reported that $\gamma \approx -0.2$, but this value does not fit our data [6, 8]. Based on panel (d), it is clear that $\gamma \geq -0.1$, a significant upward revision. Second, while it is not possible to distinguish between a plateau at around $\gamma = -0.1$ and a continued trend towards $\gamma = 0$, the latter is still entirely consistent with the simulation results. Consequently, the data offers the first substantial numerical support for the hypothesis that $\gamma = 0$.

We now turn toward characterizing the critical radius of the CTD transition in 3D. The results of our 3D simulations are presented in Fig. 2.4 using the same format as the 2D results. In panel (c), as Da tends towards zero, R_c exhibits an immediate plateau at a value of around $3D/k$. Again using the leftmost point of panel (d), we find that $\gamma = 0.02$ with a 95%CI of $[-0.27, 0.12]$. This confidence interval is very broad due to the limited number of trajectories generated at $\log_{10} Da = -2.55$. To increase the precision, we can instead estimate γ using the second-to-last point from the left (red), which has a value of -0.01 with a 95%CI of $[-0.11, 0.02]$. However, by using a larger value of the Damköhler number, we may sacrifice some accuracy with respect to the $Da \rightarrow 0$ limit.

Using the 3D data to evaluate the $\gamma = 0$ hypothesis presents its own set of challenges

because simulations in this dimension are more expensive than in 2D. To begin with, we could not observe the CTD transition at as wide a range of Damköhler numbers, and as a result, the convergence to the $Da \rightarrow 0$ limit is not as robust. For example, unlike in 2D, the plateau that corresponds to the compact growth regime $\mathcal{D}_F = 3$ is not fully developed in Fig. 2.4(a) even for the smallest value of $\log_{10} Da = -2.55$ (green curve). In addition, since we generated fewer trajectories overall, the error bars in Fig. 2.4 are wider than in Fig. 2.3. For this reason, although the flattening trend in the 3D data is clear, it is not possible to rule out plateau at a γ value between zero and -0.1 .

Despite these limitations, the estimate for γ in 3D is consistent with the 2D estimate, 95%CI $[-0.09, -0.03]$. Further, taken together, the 2D and 3D data sets offer significant evidence for the $\gamma = 0$ hypothesis. Both γ confidence intervals are close to zero, and the remaining differences can be plausibly explained by Damköhler number and statistical convergence effects.

These findings clarify the behavior of CTD transition in two ways. First, they suggest that the continuum limit of the discrete model, $Da \rightarrow 0$, is well-defined. Once the particles become small enough, the critical radius rescaled by D/k converges to a constant. Second, our results help unify the discrete and continuum models by showing that they exhibit the same dendrite formation mechanism. In both cases, the dendritic instability develops when the cluster circumference exceeds the reaction-diffusion length D/k . The ability of the continuum model to reproduce the microscopic physics of the discrete model is important because it validates the continuum approach to studying dendritic deposition more generally. In particular, this agreement provides a stronger microscopic foundation for a number of research efforts that have used continuum methods to examine electrodeposition applications including dendrite suppression strategies in lithium metal batteries [19–26]

One last feature of the CTD transition that warrants discussion is its sharpness. Fig. 2.3(b) shows that, in 2D, the height of the peak in the fractal dimension derivative, $|\mathcal{D}'_F|$, appears to diverge in the limit as $Da \rightarrow 0$. This behavior is notable because as Da gets smaller, the number of particles in the critical cluster, N_c in (2.19), goes to infinity. The sharpening of the CTD transition is thus reminiscent of the finite-size scaling of an equilibrium phase transition [35].

This connection motivates us to analyze the transition by following the standard equilibrium protocol. Specifically, we examine the scale of the divergence and the associated prefactor [35]. Fig. 2.3(e) shows the height of the peak in the derivative,

$\max |\mathcal{D}'_F|$, as a function of the Damköhler number. The line of best fit suggests that this quantity diverges logarithmically with a prefactor of -0.15 (95%CI of $[-0.16, -0.14]$). However, since the range of values in the figure is relatively small, it is not possible to distinguish between a logarithmic and a power-law divergence. The latter case leads to a best-fit exponent with the same value as the logarithmic prefactor, -0.15 with a 95%CI of $[-0.16, -0.14]$. Figs. 2.4(b) and (e) show that the CTD transition also becomes increasingly sharp in 3D, though we do not yet have enough points to evaluate the prefactor in this dimension.

Beyond a numerical characterization of the divergence of $|\mathcal{D}'_F|$, many aspects of the finite-size scaling of the CTD transition remain unclear. For example, how does this divergence emerge from the microscopic dynamics? And how does the behavior of the transition relate to finite-size scaling in equilibrium? We hope to pursue these questions in the future.

2.5 Conclusion

In this work, we examined the CTD transition in reactive deposition to clarify how the dendritic branch thickness depends on the deposition parameters. Specifically, we compared the behavior of the CTD transition in an analytically tractable continuum model and a particle-based (discrete) model. In contrast with previous studies, we found that Brownian dynamics simulations of the discrete model in the continuum limit are consistent with the behavior of the continuum model. That is, the critical radius is proportional to the ratio of the diffusion constant to the reaction rate constant. This behavior implies that these models share the same mechanism for dendritic growth. In each case, dendrites emerge when the circumference of the cluster becomes comparable to the reaction-diffusion length. More broadly, our findings suggest that continuum formulations of reactive deposition, which are widely used to study lithium metal batteries and other types of electrodeposition, are able to accurately reproduce the microscopic features of dendrite formation [19–26].

Future investigations will test whether the CTD transition displays the same phenomenology in real, as opposed to idealized, systems with the aim of managing dendritic deposition in applications like batteries. In experiments, the continuum limit could be accessed by making the reaction rate slower rather than changing the radius of the microscopic particles. This procedure would be particularly practical in electrochemistry since the applied voltage directly controls the surface reaction

kinetics [36]. However, we also expect reaction-diffusion length scaling to apply to many other systems, including those that feature the deposition of colloids or misfolded proteins.

Finally, it remains to be seen how the CTD transition interacts with more complicated deposition geometries. Here, we examined a cluster that grows outwards in all directions. This configuration has been the focus of previous computational and theoretical efforts due to its simplicity [15]. However, another possible choice is to grow the cluster upwards starting from a reactive surface at the bottom of a box, a geometry that more closely resembles a standard electrodeposition experiment [9, 37]. Intriguingly, the confinement provided by the box walls has been shown to suppress dendritic growth in experiments and continuum scale models [23–25]. We plan to characterize the CTD transition in this type of deposition in a future publication.

2.6 Acknowledgments

We thank Steve Whitelam, Tomislav Begušić, and Emiliano Deustua for providing comments on the manuscript. DJ acknowledges support from the Department of Energy Computational Science Graduate Fellowship, under Contract No. DE-FG02–97ER25308. This work was supported by a grant from NIGMS, National Institutes of Health, (R01GM125063) to TFM.

References

1. Lin, M. Y. *et al.* Universality in Colloid Aggregation. *Nature* **339**, 360–362. ISSN: 1476-4687. <https://www.nature.com/articles/339360a0> (June 1989).
2. Foderà, V., Zaccone, A., Lattuada, M. & Donald, A. M. Electrostatics Controls the Formation of Amyloid Superstructures in Protein Aggregation. *Physical Review Letters* **111**, 108105. <https://link.aps.org/doi/10.1103/PhysRevLett.111.108105> (Sept. 5, 2013).
3. Kahanda, G. L. M. K. S., Zou, X.-q., Farrell, R. & Wong, P.-z. Columnar Growth and Kinetic Roughening in Electrochemical Deposition. *Physical Review Letters* **68**, 3741–3744. <https://link.aps.org/doi/10.1103/PhysRevLett.68.3741> (June 22, 1992).
4. Witten, T. A. & Sander, L. M. Diffusion-Limited Aggregation. *Physical Review B* **27**, 5686–5697. <https://link.aps.org/doi/10.1103/PhysRevB.27.5686> (May 1, 1983).

5. Meakin, P. Diffusion-Controlled Cluster Formation in 2—6-Dimensional Space. *Physical Review A* **27**, 1495–1507. <https://link.aps.org/doi/10.1103/PhysRevA.27.1495> (Mar. 1, 1983).
6. Meakin, P. Models for Colloidal Aggregation. *Annual Review of Physical Chemistry* **39**, 237–267. ISSN: 0066-426X. <https://www.annualreviews.org/doi/10.1146/annurev.pc.39.100188.001321> (Oct. 1, 1988).
7. Nagatani, T. Laplacian Growth Phenomena with the Third Boundary Condition: Crossover from Dense Structure to Diffusion-Limited Aggregation Fractal. *Physical Review A* **40**, 7286–7291. <https://link.aps.org/doi/10.1103/PhysRevA.40.7286> (Dec. 1, 1989).
8. Halsey, T. C. & Leibig, M. Electrodeposition and Diffusion-limited Aggregation. *The Journal of Chemical Physics* **92**, 3756–3767. ISSN: 0021-9606. <https://aip.scitation.org/doi/abs/10.1063/1.457834> (Mar. 15, 1990).
9. Mayers, M. Z., Kaminski, J. W. & Miller, T. F. Suppression of Dendrite Formation via Pulse Charging in Rechargeable Lithium Metal Batteries. *The Journal of Physical Chemistry C* **116**, 26214–26221. ISSN: 1932-7447. <http://dx.doi.org/10.1021/jp309321w> (Dec. 20, 2012).
10. Mullins, W. W. & Sekerka, R. F. Morphological Stability of a Particle Growing by Diffusion or Heat Flow. *Journal of Applied Physics* **34**, 323–329. ISSN: 0021-8979. <https://aip.scitation.org/doi/abs/10.1063/1.1702607> (Feb. 1, 1963).
11. Liu, K., Liu, Y., Lin, D., Pei, A. & Cui, Y. Materials for Lithium-Ion Battery Safety. *Science Advances* **4**, eaas9820. <https://www.science.org/doi/10.1126/sciadv.aas9820> (June 22, 2018).
12. Lin, D., Liu, Y. & Cui, Y. Reviving the Lithium Metal Anode for High-Energy Batteries. *Nature Nanotechnology* **12**, 194–206. ISSN: 1748-3387. <http://www.nature.com/nnano/journal/v12/n3/full/nnano.2017.16.html> (Mar. 2017).
13. Hwang, J.-Y., Myung, S.-T. & Sun, Y.-K. Sodium-Ion Batteries: Present and Future. *Chemical Society Reviews* **46**, 3529–3614. ISSN: 1460-4744. <http://pubs.rsc.org/en/content/articlelanding/2017/cs/c6cs00776g> (June 19, 2017).
14. Meakin, P. in *On Growth and Form: Fractal and Non-Fractal Patterns in Physics* (eds Stanley, H. E. & Ostrowsky, N.) 111–135 (Springer Netherlands, Dordrecht, 1986). ISBN: 978-94-009-5165-5. https://doi.org/10.1007/978-94-009-5165-5_7.
15. Meakin, P. *Fractals, Scaling and Growth Far from Equilibrium Cambridge Nonlinear Science Series* **5**. xiv+674. ISBN: 978-0-521-45253-3 (Cambridge University Press, Cambridge [England] ; New York, 1998).

16. Erban, R. & Chapman, S. J. Reactive Boundary Conditions for Stochastic Simulations of Reaction–Diffusion Processes. *Physical Biology* **4**, 16. ISSN: 1478-3975. <http://stacks.iop.org/1478-3975/4/i=1/a=003> (2007).
17. Witten, T. A. & Sander, L. M. Diffusion-Limited Aggregation, a Kinetic Critical Phenomenon. *Physical Review Letters* **47**, 1400–1403. <https://link.aps.org/doi/10.1103/PhysRevLett.47.1400> (Nov. 9, 1981).
18. Barenblatt, G. I. *Scaling, Self-similarity, and Intermediate Asymptotics: Dimensional Analysis and Intermediate Asymptotics* 1–386. ISBN: 978-0-521-43522-2 (Cambridge University Press, 1996).
19. Aogaki, R. Image Analysis of Morphological Instability in Galvanostatic Electrocrystallization: I. General Expression for the Growth Mode of Surface Irregularities. *Journal of The Electrochemical Society* **129**, 2442. ISSN: 1945-7111. <https://iopscience.iop.org/article/10.1149/1.2123563/meta> (Nov. 1, 1982).
20. Sundström, L.-G. & Bark, F. H. On Morphological Instability during Electrodeposition with a Stagnant Binary Electrolyte. *Electrochimica Acta* **40**, 599–614. ISSN: 0013-4686. <http://www.sciencedirect.com/science/article/pii/001346869400379F> (Apr. 1, 1995).
21. Monroe, C. & Newman, J. The Effect of Interfacial Deformation on Electrodeposition Kinetics. *Journal of The Electrochemical Society* **151**, A880. ISSN: 1945-7111. <https://iopscience.iop.org/article/10.1149/1.1710893/meta> (May 4, 2004).
22. Monroe, C. & Newman, J. The Impact of Elastic Deformation on Deposition Kinetics at Lithium/Polymer Interfaces. *Journal of The Electrochemical Society* **152**, A396–A404. ISSN: 0013-4651, 1945-7111. <http://jes.ecsdl.org/content/152/2/A396> (Feb. 1, 2005).
23. Tikekar, M. D., Archer, L. A. & Koch, D. L. Stability Analysis of Electrodeposition across a Structured Electrolyte with Immobilized Anions. *Journal of The Electrochemical Society* **161**, A847–A855. ISSN: 0013-4651, 1945-7111. <https://iopscience.iop.org/article/10.1149/2.085405jes> (2014).
24. Liu, W., Lin, D., Pei, A. & Cui, Y. Stabilizing Lithium Metal Anodes by Uniform Li-Ion Flux Distribution in Nanochannel Confinement. *Journal of the American Chemical Society* **138**, 15443–15450. ISSN: 0002-7863. <https://doi.org/10.1021/jacs.6b08730> (Nov. 30, 2016).
25. Tu, Z. *et al.* Nanoporous Hybrid Electrolytes for High-Energy Batteries Based on Reactive Metal Anodes. *Advanced Energy Materials* **7**, 1602367. ISSN: 1614-6832. <https://onlinelibrary.wiley.com/doi/full/10.1002/aenm.201602367> (Apr. 1, 2017).

26. Choudhury, S. *et al.* Confining Electrodeposition of Metals in Structured Electrolytes. *Proceedings of the National Academy of Sciences* **115**, 6620–6625. ISSN: 0027-8424, 1091-6490. pmid: 29891658. <https://www.pnas.org/content/115/26/6620> (June 26, 2018).
27. Hastings, M. & Levitov, L. Laplacian Growth as One-Dimensional Turbulence. *Physica D: Nonlinear Phenomena* **116**, 244–252. ISSN: 01672789. <https://linkinghub.elsevier.com/retrieve/pii/S0167278997002443> (May 1998).
28. Singer, A., Schuss, Z., Osipov, A. & Holcman, D. Partially Reflected Diffusion. *SIAM Journal on Applied Mathematics* **68**, 844–868. ISSN: 0036-1399. <http://epubs.siam.org/doi/abs/10.1137/060663258> (Jan. 1, 2008).
29. Niemeyer, L., Pietronero, L. & Wiesmann, H. J. Fractal Dimension of Dielectric Breakdown. *Physical Review Letters* **52**, 1033–1036. <https://link.aps.org/doi/10.1103/PhysRevLett.52.1033> (Mar. 19, 1984).
30. Pietronero, L. & Wiesmann, H. J. Stochastic Model for Dielectric Breakdown. *Journal of Statistical Physics* **36**, 909–916. ISSN: 1572-9613. <https://doi.org/10.1007/BF01012949> (Sept. 1, 1984).
31. Allen, M. P. & Tildesley, D. J. *Computer Simulation of Liquids* Second edition. 626 pp. ISBN: 978-0-19-880319-5 978-0-19-880320-1 (Oxford University Press, Oxford, United Kingdom, 2017).
32. Agresti, A. & Coull, B. A. Approximate Is Better than "Exact" for Interval Estimation of Binomial Proportions. *The American Statistician* **52**, 119–126. ISSN: 0003-1305. JSTOR: 2685469 (1998).
33. Nagatani, T. & Stanley, H. E. Double-Crossover Phenomena in Laplacian Growth: Effects of Sticking Probability and Finite Viscosity Ratio. *Physical Review A* **41**, 3263–3269. <https://link.aps.org/doi/10.1103/PhysRevA.41.3263> (Mar. 1, 1990).
34. Tolman, S. & Meakin, P. Off-Lattice and Hypercubic-Lattice Models for Diffusion-Limited Aggregation in Dimensionalities 2–8. *Physical Review A* **40**, 428–437. <https://link.aps.org/doi/10.1103/PhysRevA.40.428> (July 1, 1989).
35. Newman, M. E. J. *Monte Carlo Methods in Statistical Physics* in collab. with Barkema, G. T. xiv+475. ISBN: 978-0-19-851796-2 (Clarendon Press ; Oxford University Press, Oxford : New York, 1999).
36. Bard, A. J. & Faulkner, L. R. *Electrochemical Methods: Fundamentals and Applications* 2nd ed. 833 pp. ISBN: 978-0-471-04372-0 (Wiley, New York, 2001).
37. Somfai, E., Ball, R. C., DeVita, J. P. & Sander, L. M. Diffusion-Limited Aggregation in Channel Geometry. *Physical Review E* **68**, 020401. <https://link.aps.org/doi/10.1103/PhysRevE.68.020401> (Aug. 29, 2003).

SUPPLEMENTARY MATERIALS: COMPACT-TO-DENDRITIC TRANSITION IN THE REACTIVE DEPOSITION OF BROWNIAN PARTICLES

2.7 Linear Stability Analysis of the Continuum Growth Model

The continuum reactive deposition model was first characterized by Witten and Sander in Ref. [1]. In this section, we reproduce their analysis using the updated conceptual framework from the main text⁷. We focus in particular on two-dimensional (2D) growth. The analysis for three-dimensional growth is similar.

As introduced in Sec. 2.2, the concentration field C that surrounds the cluster in the continuum model is determined by the diffusion equation and boundary conditions

$$\begin{aligned}\nabla^2 C &= 0, \\ C(|\mathbf{x}| = b) &= C_0, \\ D\nabla C(\mathbf{w}) \cdot \mathbf{n}(\mathbf{w}) &= kC(\mathbf{w}).\end{aligned}\tag{2.22}$$

Here, \mathbf{x} is position, b is the bath radius, C_0 is the bath concentration, \mathbf{w} is a position on the cluster boundary, D is the diffusion constant, and k is the surface reaction rate constant. The value of C_0 does not affect the analysis of the growth behavior as long as C is pseudosteady (see Sec. 2.2 of the main text). We are interested in understanding growth behavior in the limit as $b \rightarrow \infty$. While it is possible to analyze the model as written and then take this limit, it is simpler to take the limit first. The generalization of the bath boundary condition to an infinite domain in 2D is [3]

$$C \rightarrow C_1 \ln(r/r_0) + C_2 \text{ as } r \rightarrow \infty.\tag{2.23}$$

In this equation, r is the radial polar coordinate, C_1 is a known constant that plays the same role as C_0 in (2.22), and the parameters r_0 and C_2 are linked undetermined constants.

Following Witten and Sander, the growth behavior of the model can be characterized using a linear stability analysis [1]. This analysis takes the cluster boundary to be composed of a circle plus a small cosine perturbation with a given wavelength. If the calculated growth rate of the perturbation is faster than the growth rate of the cluster radius, then deposition will be unstable. Analyzing a cosine perturbation is enough

⁷Witten and Sander's results were originally expressed in terms of the equivalent parameters from their lattice-based deposition simulations, see Sec. 2.9 and Ref. [2].

to understand the stability of any small boundary perturbation for two reasons. First, any perturbation can be decomposed into a Fourier series, and second, the stability analysis equations are linear.

To begin, we present the equations that describe the perturbed cluster. In polar coordinates, the boundary of this cluster $\zeta(\theta)$ is

$$\zeta(\theta) = \zeta_0 + \epsilon_m \cos(m\theta). \quad (2.24)$$

Here, ζ_0 is the cluster radius, ϵ_m is the size of the perturbation and $m \in \{1, 2, 3, \dots\}$.

We then nondimensionalize with

$$\begin{aligned} \bar{\zeta} &= \zeta/\zeta_0, & \bar{C} &= C/C_1, \\ \bar{\epsilon}_m &= \epsilon_m/\zeta_0, & \bar{r} &= r/\zeta_0, \\ \bar{\nabla} &= \zeta_0 \nabla, & \psi &= \frac{k\zeta_0}{D}. \end{aligned} \quad (2.25)$$

As a result, (2.24) becomes

$$\bar{\zeta}(\theta) = 1 + \bar{\epsilon}_m \cos(m\theta), \quad (2.26)$$

and the diffusion equation and boundary conditions, (2.22), become

$$\begin{aligned} \bar{\nabla}^2 \bar{C} &= 0, \\ \bar{C} &\rightarrow \ln(\bar{r}) + \bar{C}_3 \text{ as } \bar{r} \rightarrow \infty, \\ \bar{\nabla} \bar{C}(\bar{\zeta}(\theta), \theta) \cdot \mathbf{n} &= \psi \bar{C}(\bar{\zeta}(\theta), \theta), \end{aligned} \quad (2.27)$$

where \bar{C}_3 is a new undetermined constant resulting from the transformation.

Next, we solve for \bar{C} perturbatively up to first order in the small parameter $\bar{\epsilon}_m$. Specifically, we seek a solution of the form [4]

$$\bar{C}(\bar{r}, \theta) = \bar{C}_I(\bar{r}, \theta) + \bar{\epsilon}_m \bar{C}_{II}(\bar{r}, \theta). \quad (2.28)$$

To find \bar{C}_I , we set $\bar{\epsilon}_m = 0$. Since there is no longer any perturbation, \bar{C}_I is a function of \bar{r} only, leading to the solution

$$\bar{C}_I(\bar{r}) = \ln(\bar{r}) + \psi^{-1}. \quad (2.29)$$

Solving for the second term, \bar{C}_{II} requires first expanding the reactive boundary condition at the surface to $O(\bar{\epsilon}_m)$. The outward surface unit normal is

$$\mathbf{n} = \hat{\mathbf{e}}_r + \bar{\epsilon}_m m \sin(m\theta) \hat{\mathbf{e}}_\theta, \quad (2.30)$$

where \hat{e}_r and \hat{e}_θ are the r and θ unit vectors, respectively. Consequently, the reactive boundary condition in (2.27) reduces to

$$\partial_{\bar{r}}\bar{C}(\bar{\zeta}(\theta), \theta) = \psi\bar{C}(\bar{\zeta}(\theta), \theta). \quad (2.31)$$

After expanding each side of this equation at the boundary and gathering $O(\bar{\epsilon}_m)$ terms, we have for the \bar{C}_{II} problem

$$\begin{aligned} \bar{\nabla}^2\bar{C}_{II} &= 0, \\ \bar{C}_{II} &\rightarrow 0 \text{ as } \bar{r} \rightarrow \infty, \\ \partial_{\bar{r}}\bar{C}_{II}(1, \theta) &= \psi\bar{C}_{II}(1, \theta) + \cos(m\theta)(\psi + 1), \end{aligned} \quad (2.32)$$

leading to the solution

$$\bar{C}_{II}(\bar{r}, \theta) = -\frac{\psi + 1}{\psi + m} \frac{\cos(m\theta)}{\bar{r}^m}. \quad (2.33)$$

We can now evaluate the stability of the growth. First, the (negative) flux at the surface is

$$\bar{\nabla}\bar{C}(\bar{\zeta}(\theta), \theta) \cdot \mathbf{n} = 1 + \frac{m-1}{1+m\psi^{-1}}\bar{\epsilon}_m \cos(m\theta), \quad (2.34)$$

so the dimensional growth velocity, from (2.8) in the main text, is

$$v(\theta) = \frac{\mu DC_1}{\zeta_0^2} \left[\zeta_0 + \frac{(m-1)\epsilon_m \cos(m\theta)}{1+m\frac{D}{k\zeta_0}} \right]. \quad (2.35)$$

Comparing this expression with the equation for the boundary (2.24), we see that the first term expresses the growth velocity of the radius v_{ζ_0} while the second term expresses the growth velocity of the perturbation v_{ϵ_m} . As a result, the stability parameter χ is [5]

$$\chi = \frac{v_{\epsilon_m}/\epsilon_m}{v_{\zeta_0}/\zeta_0} = \frac{m-1}{1+m\frac{D}{k\zeta_0}}. \quad (2.36)$$

Eq. (2.36) shows that when $\zeta_0 \gg D/k$, the growth is unstable, perturbations for $m > 2$ grow faster than the radius itself. However, the instability is suppressed when $\zeta_0 \ll D/k$. Based on this analysis, Witten and Sander concluded that the critical radius for the compact-to-dendritic transition in the continuum model scales as D/k [1].

2.8 Brownian Dynamics Simulations

Brownian Dynamics Algorithm

The basis for our Brownian dynamics algorithm is the standard Gaussian update of the particle position [6]. However, since the particle is often far from the cluster, using this kind of update exclusively is inefficient. Instead, we adopt several standard computational tricks to speed up the simulation of the dynamics [3, 7]. These tricks involve breaking the incoming particle's motion into three different types of steps: small steps, large steps, and first-hit steps. In this subsection, we first describe each kind of step individually and then show how we combine them to form the full algorithm. For a summary see Alg. 1.

Small Steps

During a small step, we displace the incoming particle following the standard Gaussian procedure and check for contacts with particles in the supercluster. We run the contacts check by treating the displacement as straight-line motion between the initial and final positions [2, 8]. Then to find the supercluster particles that intersect this path, we use the line-sphere intersection algorithm [9]. We also constrain the maximum distance that the particle can move in each dimension during a single step to be σ_{cut} , drawing displacements from a truncated rather than a standard Gaussian distribution. Bounding the displacement limits the number of possible contacts per step and allows us to quickly check these contacts using a cell list [6]. Further, the bias introduced by this constraint is negligible as long as σ_{cut} is large.

When the particle does make contact with the supercluster, we draw a random number and compare it to the sticking probability, (2.10), as described in the main text. If the particle does not stick, it reflects off the supercluster such that the incoming and outgoing angles of reflection are equal [2, 8]. After this contact, the particle continues to travel in a straight line, reflecting off the supercluster again if necessary. The step ends when either the particle sticks or the lengths of the particle's straight-line displacements between reflections sum to the magnitude of the initial displacement. Note that in the future, we plan to implement the additional sticking probability correction to this algorithm described in Ref. [10]. With this correction, the size of the timestep can be increased while maintaining the same level of accuracy.

Small steps have issues with numerical stability in two rare situations. The first situation occurs when the final position of the incoming particle is very close to

the supercluster boundary. Such a configuration can cause the contact checking algorithm to miss the nearby boundary during the next step. We prevent this problem by checking if the incoming particle ends up within $2a+\iota$ of any supercluster particles. Here $\iota = 1 \times 10^{-8}a$ is a threshold parameter that we use throughout the algorithm. If so, we treat the particle's final position as a contact and make a draw against the sticking probability. We then either attach the particle to the cluster or, when the draw fails, reject the original move such that $\mathbf{x}(t + \Delta t) = \mathbf{x}(t)$. The second situation that leads to numerical instability is similar to the first. It arises when the incoming particle bounces off the supercluster at a cusp within ι of the boundary of another supercluster particle. In this case, the contact checking algorithm may once again miss the nearby boundary during the next cycle of motion. We avoid this problem by rejecting the move rather than continuing to resolve the bounce.

Large Steps

We use the second type of step, large steps, when the particle is far from the supercluster. During these steps, we first find the distance H from the incoming particle to the nearest supercluster particle. This operation can be done in $O(\ln N)$ time using a k -d tree [7, 11]. We then displace the incoming particle by $H - 2a - 2\iota$ in a random direction. Such a step size guarantees that no contacts will occur. Note that we must subtract 2ι instead of just ι from displacement since supercluster particles already have a skin of size ι for collision detection, as mentioned previously.

First-Hit Steps

The final type of step we use in the Brownian dynamics algorithm is the first-hit step. For this step, we first define a circle (or sphere in 3D) centered at the origin that bounds the supercluster. Then, if the incoming particle ends up outside this region, we return it to a point on the bounding surface by integrating the dynamics analytically [3]. The analytical integration involves calculating the first-hit distribution, the probability distribution that the particle hits the bounding circle (or sphere) for the first time at a given point. The 2D first-hit distribution is derived in Ref. [3] and we derive the 3D first-hit distribution in in Sec. 2.10.

A key feature that makes the first-hit calculation possible is that in the limit as the bath distance goes to infinity, the effect of the bath can be ignored. In other words, the analytical first-hit distribution can be calculated in an unbounded domain. To understand how the unbounded domain approximation works, consider the growth

dynamics when the bath is in place. In this case, if the diffusive particle makes it all the way out to the bath, it is killed. The next particle that is launched is then equally likely to approach the supercluster from any direction. Now consider the case without a bath. When the particle reaches the bath distance it will continue to diffuse rather than being killed. However, at this point, the particle is so far from the supercluster that when it returns, it will also be equally likely to approach from any direction. Consequently, the systems with a bath and without a bath have the same first-hit distribution.

Combined Algorithm

Having specified the three different types of steps, we combine them to form the Brownian dynamics algorithm according to Alg. 1. First, we check the cell list to see if any supercluster particles are in the incoming particle's current cell or any adjacent cells. If so, we choose to take a small step. Otherwise, we take a large step. Following this choice, if the particle ends up outside the circle or sphere that bounds the supercluster, we take a first-hit step. Lastly, when the time comes to launch a new incoming particle, we initialize it from a random point on the same first-hit bounding surface.

Algorithm 1 Brownian Dynamics Algorithm

```

while cluster size < desired size do
  initialize new incoming particle
  while incoming particle not stuck do
    if current and adjacent cells empty then
      take small step
    else
      take large step
    end if
    if outside supercluster bounding circle/sphere then
      take first-hit step
    end if
  end while
end while

```

Timestep Convergence

The Brownian dynamics algorithm has two convergence parameters, both of which relate to small steps: the timestep Δt and the cutoff distance σ_{cut} . We set these parameters based on the root-mean-square displacement (RMSD) of the particle per

timestep in each dimension

$$\eta = \sqrt{2D\Delta t}. \quad (2.37)$$

Note that this is the RMSD for a non-truncated Gaussian distribution. The truncated Gaussian distribution we use for small steps has a smaller RMSD, but the difference is negligible if σ_{cut} is large. For example, when $\sigma_{\text{cut}}/\eta = 5$, these quantities differ by less than 0.001%. Given η in one dimension, the total RMSD of the particle during a small step in d dimensions is $\sqrt{d\eta^2}$. Setting the value of this latter quantity implicitly sets Δt .

To choose the timestep and cutoff distance for our simulations, we evaluated the effect of these parameters on the critical radius. Fig. 2.5(a) shows the results of our calculations for 2D deposition. The overlap of the blue and orange curves demonstrates that at $\sqrt{d\eta^2}/a = 2$ and $\sigma_{\text{cut}}/\eta = 5$, R_c is converged to within error bars. We consequently selected these parameters.

We tested the convergence of the critical radius in 3D using the same approach. In this case, Fig. 2.5(b) shows that the timestep and cutoff convergence is slightly worse than in 2D. Specifically, the confidence intervals for the orange point on the right and the associated blue point do not overlap. However, if the timestep is too small, generating clusters in 3D is prohibitively expensive in the limit as $\text{Da} \rightarrow 0$. We consequently selected the same set of parameters as in 2D, $\sqrt{d\eta^2}/a = 2$ and $\sigma_{\text{cut}}/\eta = 5$, for our simulations to provide a balance of speed and accuracy.

Parallel Algorithm

Even with computational tricks like large steps and first-hit steps, generating large clusters is still expensive, especially in 3D. Consequently, to further increase the speed of our simulations, we used a simple parallel algorithm. In this algorithm, the dynamics of M particles are propagated simultaneously on M different CPUs. To begin, these particles each take a total of s small or large steps (first-hit steps are also taken as needed). If a particle sticks to the cluster during this interval, the remaining steps are forfeited. After these s steps, information about which particles deposited onto the cluster is shared between the processors, and new incoming particles are introduced to the system. In rare cases, two incoming particles stick in the same place, or an incoming particle ends up inside a newly added supercluster particle. To resolve these issues, we eliminate one of the offending particles. If one particle is free (versus attached to the cluster), we eliminate that one, otherwise we choose randomly.

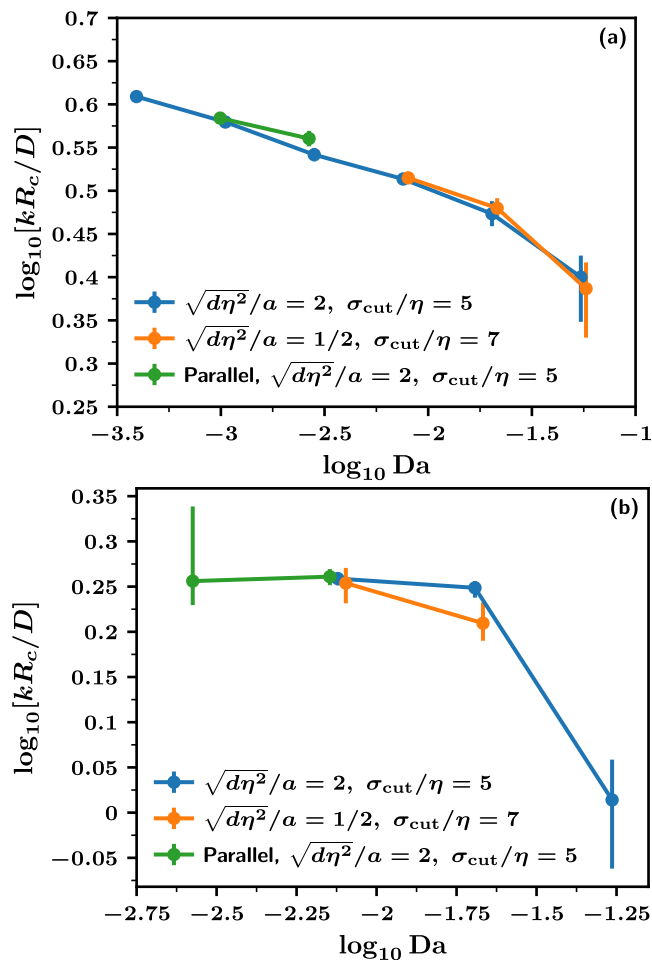


Figure 2.5: Test of the timestep and parallel algorithm convergence for 2D (a) and 3D (b) Brownian dynamics simulations. Each panel shows the critical radius R_c versus the Damköhler number Da for the serial (blue and orange curves) and parallel (green curve) algorithms. The serial curves were generated with different values of the cutoff distance σ_{cut} and the root-mean-square-displacement per timestep $\sqrt{d\eta^2}$ (which implicitly sets the value of the timestep Δt , see (2.37)). Note that to increase the visibility of individual points, the x-values of the orange and green curves in both panels are shifted by 0.025 and -0.025 , respectively.

The parallel interval parameter s offers the following trade-off. Using a small value of s decreases the speed of the algorithm because it increases the amount of inter-processor communication. However, using a large value of s is inefficient because an incoming particle may stick early in the cycle. In this case, the associated processor must wait a long time before it can be occupied with a new incoming particle. A large value of s also causes a higher fraction of the incoming particles to stick in each cycle, creating more overlap artifacts. For our simulations, we used $s = 100$.

While the parallel algorithm speeds up the generation of large clusters, it also biases the growth morphology. The easiest way to limit this bias is to use the parallel algorithm for less time by starting from a medium-sized, serially-generated cluster rather than a single seed particle [12]. Here, if we estimated that the compact-to-dendritic transition would occur at N_c particles, we switched to the parallel algorithm at $N_c/2$ particles. Reducing M also decreases the algorithm's bias. However, we set $M = 16$ to take advantage of our computer cluster's architecture.

Fig. 2.5(a) shows an empirical test of the parallel bias for 2D deposition. This figure compares the critical radius computed with the serial algorithm (blue curve) and the parallel algorithm (green curve). Though there are only two data points, the bias appears to be smaller for smaller values of Da .

We used the same setup in Fig. 2.5(b) to test the bias of the parallel algorithm in 3D. Comparing the serial and parallel algorithms at $\log_{10} Da = -2.12$ shows that the bias introduced by the latter at this Damköhler number is negligible. Based on this data point and the trend of the bias with Da in 2D, we used the parallel algorithm for our 3D simulations at $\log_{10} Da = -2.55$. We did not use the parallel algorithm for our 2D simulations.

Trajectory Details

Tables 2.1 and 2.2 summarize the number of 2D and 3D trajectories (runs) used to generate the figures in the main text. These tables include two entries for the number of runs for each value of Da , R_c runs, and extended runs. The R_c runs indicate the number of trajectories we used to calculate the critical radius. After this calculation, we continued with a smaller number of runs, extended runs, to map out the rest of the fractal dimension curve. The switch between the R_c runs and extended runs is also the reason that the size of the error bars increases substantially in Figs. 2.3(a) and 2.4(b) in the main text when the cluster radius of gyration exceeds the critical radius, $R_g > R_c$.

Table 2.1: Details of the 2D deposition simulations used to generate Fig. 2.3 in the main text. The first column lists the Damköhler number Da . The second column, R_c runs, indicates the number of runs used to calculate the critical radius. A smaller number of runs listed in the next column, extended runs, were extended in some cases to map out the fractal dimension curve. Finally, the last column indicates whether we used the parallel or serial algorithm.

$\log_{10} Da$	R_c Runs	Extended Runs	Parallel
-1.26	400,000	100	No
-1.69	40,000	100	No
-2.12	10,000	100	No
-2.55	1000	100	No
-2.98	400	N/A	No
-3.14	400	N/A	No

Table 2.2: Descriptions of the 3D simulations used to generate Fig. 2.4 in the main text. The columns are the same as in Table 2.1.

$\log_{10} Da$	R_c Runs	Extended Runs	Parallel
-1.26	10,000	100	No
-1.69	30,000	10	No
-2.12	1000	10	No
-2.55	10	N/A	Yes

2.9 Reactive Deposition on a Lattice

While the main text focuses on off-lattice formulations of discrete reactive deposition, a number of authors have also examined deposition on a lattice [1, 13]. In this section, we briefly review these efforts and discuss their implications for the study of the compact-to-dendritic transition.

To begin with, we clarify the relationship between off-lattice and lattice-based simulations. Specifically, it is possible to use a lattice model to propagate the exact deposition dynamics of an *off-lattice system* by taking the limit as the lattice constant l goes to zero while the particle radius a remains fixed [2]. Fig. 2.9 demonstrates that in this limit, particles start to take up more and more lattice sites. But similar to taking $\Delta t \rightarrow 0$ in an off-lattice simulation, when taking $l \rightarrow 0$ on a lattice, the sticking probability P acts as a second convergence parameter. The rate constant k being simulated depends on l and P through

$$k = DP/l. \quad (2.38)$$

Therefore, to maintain a constant surface reaction rate as $l \rightarrow 0$, the ratio P/l must be kept fixed.

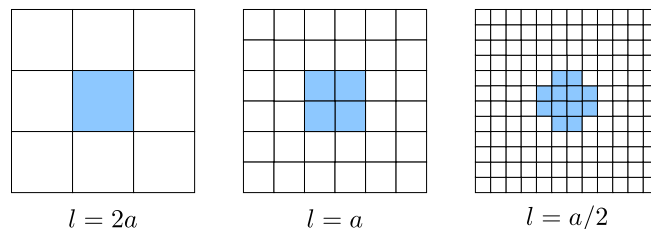


Figure 2.6: Illustration of a particle (light blue) with radius a represented on square lattices with varying lattice constants l . As l becomes smaller, the particle takes up an increasing number of lattice sites.

Previous studies that used lattice models, however, did not attempt to simulate the behavior of an off-lattice system in this manner [1, 13]. Instead, they kept the lattice constant fixed at the particle diameter, $l = 2a$, such that each particle fills one lattice site. This type of approach is well suited for modeling systems where the lattice has a physical basis, like the aggregation of atoms diffusing across a crystal surface.

Meakin in particular examined the compact-to-dendritic transition on a triangular lattice [13]. When l is a fixed value, the sticking probability can be taken to be a physical parameter rather than a convergence parameter. As a result, the critical radius for the compact-to-dendritic transition in the limit $P \rightarrow 0$ is expected to scale as

$$R_c/l \sim P^\nu \quad (2.39)$$

with unknown exponent ν [13, 14]. Meakin used simulations to estimate that $\nu = -1.2$ [13, 15].

The study of the compact-to-dendritic transition on a lattice raises the question of whether this phenomenon behaves the same way as it does off-lattice. Previous authors expected that it would given that, in surface growth models, the on- versus off-lattice distinction usually has no effect on the large-length scale emergent properties of the morphology [1, 16]. It is now clear, however, that the features of the compact-to-dendritic transition do depend on the underlying geometry of the system. Specifically, on a lattice, the lattice symmetry introduces persistent anisotropy into the dendritic structure of the cluster [17, 18]. In spite of this difference, it is still possible that lattice-based and off-lattice deposition share the same critical radius scaling. Making use of (2.38), we find that Meakin's ν estimate is consistent with an off-lattice scaling exponent of $\gamma = -0.2$.

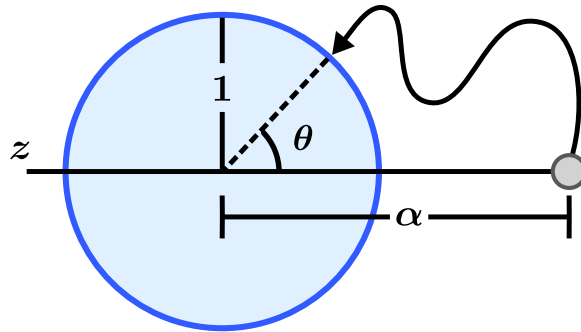


Figure 2.7: The particle lies on the z -axis a distance α away from the center of an absorbing unit sphere. Once released, it diffuses until it escapes off to infinity or absorbs at polar angle θ .

2.10 First-Hit Distribution in Three Dimensions

Here, we calculate the (3D) first-hit distribution for a Brownian particle released from a point outside of an absorbing sphere. This distribution gives the probability density that the particle first makes contact with the sphere at a given position on the surface. Our derivation closely follows the derivation of the 2D first-hit distribution found in Ref. [3]. We also describe how we sample the 3D first-hit distribution for our deposition simulations.

To set up the calculation, consider a sphere with a given radius centered at the origin and a Brownian point particle outside of this sphere as shown in Fig. 2.7. After nondimensionalizing by the sphere's radius, the particle position vector is $\bar{\mathbf{x}}_0 = \alpha \hat{\mathbf{e}}_z$ where $\alpha > 1$. Since the geometry is symmetric in the azimuthal angle, the first-hit distribution is a function of the polar angle θ alone.

To determine the first-hit distribution, we start with the dimensionless probability density of the particle $\xi(\bar{\mathbf{x}}, \tau)$. This density evolves according to the diffusion equation

$$\frac{\partial \xi}{\partial \tau} = \bar{\nabla}^2 \xi. \quad (2.40)$$

The boundary condition for ξ on the sphere is

$$\xi(|\bar{\mathbf{x}}| = 1, \tau) = 0 \quad (2.41)$$

and the initial condition is

$$\xi(\bar{\mathbf{x}}, 0) = \delta(\bar{\mathbf{x}} - \bar{\mathbf{x}}_0). \quad (2.42)$$

Instead of solving for ξ explicitly, we integrate (2.40) with respect to time, yielding

$$\bar{\nabla}^2 \int_0^\infty \xi d\tau = -\delta(\bar{\mathbf{x}} - \bar{\mathbf{x}}_0). \quad (2.43)$$

The right-hand side of this equation follows from

$$\xi(\bar{\mathbf{x}}, \tau = \infty) = 0 \quad (2.44)$$

which is justified since the particle probability density eventually either absorbs or spreads across the infinite domain making ξ arbitrarily small. After defining $\Xi(\bar{\mathbf{x}}) = \int_0^\infty \xi(\bar{\mathbf{x}}, \tau) d\tau$, we have

$$\bar{\nabla}^2 \Xi = -\delta(\bar{\mathbf{x}} - \bar{\mathbf{x}}_0) \quad (2.45)$$

with the boundary condition

$$\Xi(|\bar{\mathbf{x}}| = 1) = 0. \quad (2.46)$$

Eqs. (2.45) and (2.46) are equivalent to the problem of a point charge next to a conducting sphere. Solving these equations using the method of images yields

$$\Xi(\bar{\mathbf{x}}) \sim \frac{1}{|\bar{\mathbf{x}} - \bar{\mathbf{x}}_0|} - \frac{1/\alpha}{|\bar{\mathbf{x}} - \frac{1}{\alpha^2}\bar{\mathbf{x}}_0|}. \quad (2.47)$$

Upon switching to spherical coordinates $\bar{r} = |\bar{\mathbf{x}}|$ and $\Omega = \cos(\theta)$, we have

$$\Xi(\bar{r}, \Omega) \sim \frac{1}{\sqrt{\bar{r}^2 + \alpha^2 - 2\alpha\bar{r}\Omega}} - \frac{1}{\sqrt{1 + \alpha^2\bar{r}^2 - 2\alpha\bar{r}\Omega}}. \quad (2.48)$$

We are now ready to calculate the first-hit distribution $q(\Omega)$. This distribution is proportional to the time integral of the radial flux on the sphere. First, note that the integrated radial flux in general $\lambda(\bar{r}, \Omega)$ is

$$\lambda = \int_0^\infty \frac{\partial \xi}{\partial \bar{r}} d\tau = \frac{\partial}{\partial \bar{r}} \left(\int_0^\infty \xi d\tau \right) = \frac{\partial \Xi}{\partial \bar{r}}. \quad (2.49)$$

After evaluating λ on the sphere, $\bar{r} = 1$, and adding a normalizing constant, we have

$$q(\Omega) = \frac{\alpha^3 - \alpha}{2(\alpha^2 - 2\alpha\Omega + 1)^{3/2}}. \quad (2.50)$$

Lastly, to get the first-hit cumulative distribution function (CDF) $Q(\Omega)$ we integrate from -1 to Ω

$$Q(\Omega) = \frac{(\alpha - 1) \left(\alpha + 1 - \sqrt{\alpha^2 - 2\alpha\Omega + 1} \right)}{2\sqrt{\alpha^2 - 2\alpha\Omega + 1}}. \quad (2.51)$$

Although Eq. (2.51) is normalized, we have not yet addressed the transience of Brownian motion in three dimensions. Unlike in 2D, there is a chance the particle will escape to infinity before absorbing at the boundary. Specifically, this escape probability is [19]

$$\text{Probability(Escape)} = 1 - \frac{1}{\alpha}. \quad (2.52)$$

Consequently, sampling the 3D first-hit distribution requires two steps. First, we must make a draw against the escape probability in (2.52) to see if the particle makes contact with the sphere at all. If not, we sample (2.51), the CDF, by setting Q equal to a random number taken from $[0, 1]$ and solving for Ω

$$\Omega = \frac{\alpha^2 + 1}{2\alpha} - \frac{(\alpha^2 - 1)^2}{2\alpha(\alpha - 1 + 2Q)^2}. \quad (2.53)$$

The azimuthal angle can then be drawn randomly from the interval $[0, 2\pi)$. When sampling the first-hit distribution for our 3D deposition simulations, if the particle escapes in the first step, it is taken to have reached the distant, surrounding bath. As a result, the particle is killed, and a new diffusive particle is launched.

References

1. Witten, T. A. & Sander, L. M. Diffusion-Limited Aggregation. *Physical Review B* **27**, 5686–5697. <https://link.aps.org/doi/10.1103/PhysRevB.27.5686> (May 1, 1983).
2. Erban, R. & Chapman, S. J. Reactive Boundary Conditions for Stochastic Simulations of Reaction–Diffusion Processes. *Physical Biology* **4**, 16. ISSN: 1478-3975. <http://stacks.iop.org/1478-3975/4/i=1/a=003> (2007).
3. Sander, E., Sander, L. M. & Ziff, R. M. Fractals and Fractal Correlations. *Computers in Physics* **8**, 420–425. ISSN: 0894-1866. <https://aip.scitation.org/doi/10.1063/1.168501> (July 1, 1994).
4. Dyke, M. D. V. *Perturbation Methods in Fluid Mechanics* Annotated ed edition (ed Dyke, M. V.) 271 pp. ISBN: 978-0-915760-01-5 (Parabolic Pr, Stanford, Calif, June 15, 1975).
5. Mullins, W. W. & Sekerka, R. F. Morphological Stability of a Particle Growing by Diffusion or Heat Flow. *Journal of Applied Physics* **34**, 323–329. ISSN: 0021-8979. <https://aip.scitation.org/doi/abs/10.1063/1.1702607> (Feb. 1, 1963).
6. Allen, M. P. & Tildesley, D. J. *Computer Simulation of Liquids* Second edition. 626 pp. ISBN: 978-0-19-880319-5 978-0-19-880320-1 (Oxford University Press, Oxford, United Kingdom, 2017).

7. Tolman, S. & Meakin, P. Off-Lattice and Hypercubic-Lattice Models for Diffusion-Limited Aggregation in Dimensionalities 2–8. *Physical Review A* **40**, 428–437. <https://link.aps.org/doi/10.1103/PhysRevA.40.428> (July 1, 1989).
8. Singer, A., Schuss, Z., Osipov, A. & Holcman, D. Partially Reflected Diffusion. *SIAM Journal on Applied Mathematics* **68**, 844–868. ISSN: 0036-1399. <http://epubs.siam.org/doi/abs/10.1137/060663258> (Jan. 1, 2008).
9. Eberly, D. H. *3D Game Engine Design: A Practical Approach to Real-Time Computer Graphics* 2nd edition. 1040 pp. ISBN: 978-0-12-229063-3 (CRC Press, Amsterdam ; Boston, Nov. 3, 2006).
10. Boccoardo, G., Sokolov, I. M. & Paster, A. An Improved Scheme for a Robin Boundary Condition in Discrete-Time Random Walk Algorithms. *Journal of Computational Physics* **374**, 1152–1165. ISSN: 0021-9991. <http://www.sciencedirect.com/science/article/pii/S002199911830531X> (Dec. 1, 2018).
11. Blanco, J. L. & Rai, P. K. *nanoflann: a C++ header-only fork of FLANN, a library for Nearest Neighbor (NN) with KD-trees* <https://github.com/jlblancoc/nanoflann>. 2014.
12. Kaufman, H., Vespignani, A., Mandelbrot, B. B. & Woog, L. Parallel Diffusion-Limited Aggregation. *Physical Review E* **52**, 5602–5609. ISSN: 1063-651X, 1095-3787. <https://link.aps.org/doi/10.1103/PhysRevE.52.5602> (Nov. 1, 1995).
13. Meakin, P. Models for Colloidal Aggregation. *Annual Review of Physical Chemistry* **39**, 237–267. ISSN: 0066-426X. <https://www.annualreviews.org/doi/10.1146/annurev.pc.39.100188.001321> (Oct. 1, 1988).
14. Barenblatt, G. I. *Scaling, Self-similarity, and Intermediate Asymptotics: Dimensional Analysis and Intermediate Asymptotics* 1–386. ISBN: 978-0-521-43522-2 (Cambridge University Press, 1996).
15. Meakin, P. *Fractals, Scaling and Growth Far from Equilibrium Cambridge Nonlinear Science Series* **5**. xiv+674. ISBN: 978-0-521-45253-3 (Cambridge University Press, Cambridge [England] ; New York, 1998).
16. Barabási, A.-L. *Fractal Concepts in Surface Growth* in collab. with Stanley, H. E. xx+366. ISBN: 978-0-511-59979-8 (Cambridge University Press, New York, N.Y., 1995).
17. Meakin, P. & Family, F. Structure and Dynamics of Reaction-Limited Aggregation. *Physical Review A* **36**, 5498–5501. ISSN: 0556-2791. <https://link.aps.org/doi/10.1103/PhysRevA.36.5498> (Dec. 1, 1987).

18. Grebenkov, D. S. & Beliaev, D. How Anisotropy Beats Fractality in Two-Dimensional on-Lattice Diffusion-Limited-Aggregation Growth. *Physical Review E* **96**, 042159. <https://link.aps.org/doi/10.1103/PhysRevE.96.042159> (Oct. 30, 2017).
19. Wendel, J. G. Hitting Spheres with Brownian Motion. *The Annals of Probability* **8**, 164–169. ISSN: 0091-1798, 2168-894X. <https://projecteuclid.org/euclid.aop/1176994833> (Feb. 1980).

DIRECT EVALUATION OF DYNAMICAL LARGE-DEVIATION RATE FUNCTIONS USING A VARIATIONAL ANSATZ

Jacobson, D. & Whitlam, S. Direct Evaluation of Dynamical Large-Deviation Rate Functions Using a Variational Ansatz. *Physical Review E* **100**, 052139. <https://link.aps.org/doi/10.1103/PhysRevE.100.052139> (Nov. 25, 2019)

Chapter Abstract

We describe a simple form of importance sampling designed to bound and compute large-deviation rate functions for time-extensive dynamical observables in continuous-time Markov chains. We start with a model, defined by a set of rates, and a time-extensive dynamical observable. We construct a reference model, a variational ansatz for the behavior of the original model conditioned on atypical values of the observable. Direct simulation of the reference model provides an upper bound on the large-deviation rate function associated with the original model, an estimate of the tightness of the bound, and, if the ansatz is chosen well, the exact rate function. The exact rare behavior of the original model does not need to be known in advance. We use this method to calculate rate functions for currents and counting observables in a set of network- and lattice models taken from the literature. Straightforward ansätze yield bounds that are tighter than bounds obtained from Level 2.5 of large deviations via approximations that involve uniform scalings of rates. We show how to correct these bounds in order to recover the rate functions exactly. Our approach is complementary to more specialized methods, and offers a physically transparent framework for approximating and calculating the likelihood of dynamical large deviations.

3.1 Introduction

Dynamical systems, such as chemical networks [1], biochemical and molecular machines [2–4], and models of driven [5–8] and glassy [9–11] systems, exhibit fluctuations, departures from typical behavior [12]. Fluctuations of time-extensive observables – which can be work, entropy production [13, 14], other currents [8, 15, 16], or dynamical activity [11, 17] – characterize the behavior of these systems, much as fluctuations of size-extensive quantities, such as energy or magnetization,

characterize the static behavior of equilibrium systems [18, 19]. The probability distributions that control dynamical fluctuations satisfy certain requirements, known as fluctuation relations [3, 13, 14, 20–26], which impose constraints on their symmetries. The precise form of these distributions, however, must be obtained by explicit calculation.

Here we focus on calculating probability distributions $\rho_T(A)$ for models with a discrete state space, for stochastic dynamical trajectories of elapsed time T and time-extensive observables A . Time-extensive observables are those that can be built from a sum of values of individual pieces of a trajectory. For large values of T these distributions often adopt the large-deviation form [20–25, 27, 28]

$$\rho_T(A) \approx e^{-TJ(a)}, \quad (3.1)$$

in which $a = A/T$ is the time-intensive value of the observable. $J(a)$ is the large-deviation *rate function*, which quantifies the likelihood of observing particular values of the observable a ¹. The symbol \approx denotes equality of the logarithms of both sides of (3.1), to leading order in T , for all values of a . In the physics literature, most numerical methods for calculating $J(a)$ aim to first compute its Legendre transform, the scaled cumulant-generating function (SCGF) [11, 28, 32–37]. It is possible to recover $J(a)$ from the SCGF if the former is convex [38]. A common way to calculate the SCGF is to use cloning methods [32, 39], which duplicate or eliminate trajectories according to their time-integrated weights. Often cloning is supplemented by other importance-sampling methods [34–36], some of which make use of a modified dynamics in order to produce trajectories that more closely resemble the rare dynamics of the original model.

Determining $J(a)$ *solely* by reweighting trajectories of a modified dynamics, without prior knowledge of the rare dynamics of the model of interest, is not widely done (see, however, Refs. [40–43]). Standard arguments suggest that determining the probability distribution of a within one dynamics by reweighting against a second dynamics requires, in general, the evaluation of random quantities whose variance is exponential in the trajectory length [44–47] (see Section 3.2). Such observations are sometimes taken to mean that trajectory reweighting, without advance knowledge of the rare dynamics to be sampled, is little better than direct sampling using the original model [48]. Here we argue that more optimism is warranted, and show

¹More directly it quantifies the rate of decay of a fluctuation a , which depends both on the likelihood of a and the basic timescale governing the establishment and decay of fluctuations. This latter piece plays a key role for certain models [29–31].

that the conditions under which meaningful results can be extracted from trajectory reweighting are much less restrictive than has been recognized. Moreover, trajectory reweighting presents few technical complications beyond the requirement to simulate the original model with modified rates, and allows the reconstruction of $J(a)$ directly, without first calculating the SCGF.

To compute the large-deviation rate function $J(a)$ for a given model and dynamical observable a , we use a simple form of importance sampling [44–46, 49–52]. We begin with a modification of the model dynamics. This modified or *reference* model is a microscopic ansatz for the original model’s behavior, conditioned on particular values of the observable a . The ansatz is characterized by a set of parameters whose values we determine variationally. In practical terms we simply guess a reference dynamics that is able to generate more or less of a than the normal dynamics. Let the typical value of a produced by original and reference models be a_0 and \tilde{a}_0 , respectively ². Reweighting trajectories of the reference model produces an upper bound on the rate function J associated with the original model at the point \tilde{a}_0 , an estimate of the tightness of the bound, and, if the ansatz is chosen well, the exact rate function (to within statistical error). That is, the reference dynamics is a true ansatz, a guess whose accuracy can be determined by subsequent calculation. Repeating the calculation for a set of reference models possessing a set of distinct values $\{\tilde{a}_0\}$ allows us to attempt reconstruction of $J(a)$ at the set of points $a \in \{\tilde{a}_0\}$. In this respect the procedure is similar to umbrella sampling of equilibrium systems. We show that the conditions under which the exact rate function can be recovered are less restrictive than usually assumed.

Any reference dynamics can be reweighted to produce *some* upper bound on $J(a)$, simply by making the desired value of a typical [53]. Good choices of reference dynamics, leading to tight bounds, render the fluctuations of the reweighting factor or likelihood ratio (the ratio of path probability of new and old dynamics) small. We show here that relatively simple reference-model choices produce meaningful (i.e. tight) bounds, for a set of models and observables taken from the literature. We compare the bounds produced by our method with universal bounds on currents [54, 55] and non-decreasing counting variables [56]. Those bounds can be obtained from Level 2.5 of large deviations [57, 58], the exact rate function for the empirical flow (jumps between states) and measure (state occupation times), via a uniform rescaling

²The “typical” value of a time-integrated observable is the value to which the sample mean of an unbiased estimator of that quantity converges at long times, provided that a large-deviation principle exists and that the associated rate function has a unique zero [28].

of rates. That approach provides important physical insight into the quantities that constrain fluctuations of time-integrated observables, and also provides numerical bounds on rate functions. Our approach, which uses a microscopic ansatz within the exact path integral for the dynamics, produces tighter bounds, particularly far into the tails of rate functions. The extent to which bounds vary as we change the nature of the ansatz provides physical insight into how much certain types of microscopic processes contribute to the rare dynamics of a model. Microscopic ansätze, even relatively simple ones, are capable of capturing a wide range of behavior, including regimes of anomalous fluctuations in which the usual central-limit theorem breaks down [41]. Computing a correction to these bounds, by measuring fluctuations of the likelihood ratio, allows the recovery of the exact rate function. Importantly, fluctuations of the likelihood ratio do not need to be zero for $J(a)$ to be calculated

The approach described here is variational, in the sense that we vary the parameters of the reference model in order to identify the dynamics that best approximates the rare dynamics of interest. Variational principles underpin the study of large deviations, embodied by the notion that “any large deviation is done in the least unlikely of all the unlikely ways” [27]. Variational ideas are central to different representations of rare processes – see e.g. Section 5 of Ref. [33] – and have been widely used in analytic and numerical work [35, 37, 59–61]. The aim of this paper is to present a simple, physically-motivated approach to bounding and calculating rate functions using a variational principle enacted by (only) direct simulations, and to present a set of convergence criteria, adapted from Ref. [62], that reveal when bounds can be corrected to produce the exact rate function. We have provided a GitHub script [63] that computes the correction term automatically, this being the most involved step of the calculation. These results extend our previous work [41–43] by a) showing how different forms of physically-motivated reference dynamics can be used to treat different models, and b) by providing a set of criteria that identify when the exact rate function can be recovered. One point we emphasize is that considerable progress can be made using physical intuition and basic knowledge of the properties of a model, without the application of other forms of importance sampling (such as cloning or transition-path sampling). Our method requires only continuous-time Monte Carlo simulation, and so can be applied to any set of circumstances in which that method can be used, including to models with unbounded state spaces [41]. In addition, it can be used to reconstruct families of large-deviation rate functions from a single set of simulations, using the principle that the dynamics of one model can be reweighted to examine the dynamics of many others [43]. Reference models

represent a form of importance sampling similar in spirit but different in detail to the umbrella potentials used in equilibrium sampling [64, 65].

In Section 3.2 we describe our approach, which we refer to as VARD (for Variational Ansatz for Rare Dynamics). In general terms there are many forms of VARD that have been used in the literature (see above); we use the term to convey the specific notion of doing (only) direct simulations of a family of modified models. In Section 3.3 we apply the method to four models taken from the literature. We have chosen models from the literature that display a variety of interesting behavior: two lattice models (the asymmetric simple exclusion process [6, 66] and the Fredrickson-Andersen model [67]) and two network models, and we sample both currents and non-decreasing counting variables to show that the method works the same way for each. In the cases described in Section 3.3–Section 3.3, relatively simple choices of reference model allow the computation of the exact rate function, and we gain physical insight into the nature of the dynamics that contributes to particular pieces of $J(a)$. We also show, in Section 3.3, that bounds that are descriptive in small systems remain so in larger systems. We conclude in Section 3.4.

3.2 A variational ansatz for rare dynamics

Continuous-time Markov chains and large deviations

Consider a continuous-time dynamics [68] on a set of discrete states, defined by the master equation

$$\partial_t P_x(t) = \sum_{y \neq x} W_{yx} P_y(t) - R_x P_x(t). \quad (3.2)$$

Here $P_x(t)$ is the probability that a system resides in (micro)state x at time t . W_{xy} is the rate for passing from state x to state y , and $R_x = \sum_{y \neq x} W_{xy}$ is the escape rate from x (Table 1 provides a reference for some of the more frequently-used symbols in this paper). The standard algorithm for simulating the dynamics (3.2) is as follows [69]. From state x , choose a destination state y with probability

$$p_{xy} = \frac{W_{xy}}{R_x}. \quad (3.3)$$

The time increment Δt required to make this move is a random number drawn from the exponential distribution with mean $1/R_x$,

$$p_x(\Delta t) = R_x e^{-R_x \Delta t}. \quad (3.4)$$

Given an initial state x_0 , the dynamics defined by (4.2) and (3.4) generates a trajectory $\omega = x_0 \rightarrow x_1 \rightarrow \dots \rightarrow x_{K(\omega)}$, which consists of a sequence of $K(\omega)$ jumps

$x_k \rightarrow x_{k+1}$ and associated jump times Δt_k . In this paper we are concerned with calculating

$$\rho_T(A) = \sum_{\omega} p(\omega) \delta(T(\omega) - T) \delta(A(\omega) - A), \quad (3.5)$$

the probability distribution, taken over all trajectories of elapsed time T , of a time-extensive dynamical observable

$$A(\omega) = \sum_{k=0}^{K(\omega)-1} \alpha_{x_k x_{k+1}}. \quad (3.6)$$

Here α_{xy} is the change of the observable A upon moving from x to y , and $A(\omega)$ is the sum of these quantities over a single trajectory ω . We define $a(\omega) \equiv A(\omega)/T(\omega)$ as the time-intensive version of A . $T(\omega)$ is the elapsed time of trajectory ω , and is equal to T when $T_{K(\omega)} \leq T < T_{K(\omega)+1}$, where $T_{K(\omega)} = \sum_{k=0}^{K(\omega)-1} \Delta t_k$. The symbol $p(\omega)$ is the probability of a trajectory ω . Given an initial state, this term is equal to a product of factors (4.2) and (3.4) for all jumps of the trajectory, multiplied by the probability of not exiting state $x_{K(\omega)}$ between times $T_{K(\omega)}$ and T .

Table 3.1: Glossary of frequently-used symbols

$A = aT$	path-extensive order parameter
T	elapsed time of a trajectory
K	number of jumps of a trajectory
α_{xy}	change of A upon making the jump $x \rightarrow y$
W_{xy}	“original” model rates for the jump $x \rightarrow y$
R_x	“original” model escape rate $\sum_{y \neq x} W_{xy}$
a_0	typical value of a under the original dynamics
$J(a)$	rate function for a under the original dynamics
$J_0(a)$	upper bound on $J(a)$
$J_1(a)$	correction to the bound: $J(a) = J_0(a) + J_1(a)$
\tilde{W}_{xy}	reference-model rates for jumps $x \rightarrow y$
s	one parameter of \tilde{W}_{xy} : see (3.8)
β_{xy}	remaining parameters of \tilde{W}_{xy} : see (3.8)
\tilde{R}_x	reference-model escape rate $\sum_{y \neq x} \tilde{W}_{xy}$
λ	clock bias: see (3.9)
\tilde{a}_0	typical value of a under the reference dynamics
$J_0[\{x\}]$	$J_0(a)$ determined from a scan of the reference-model parameter set $\{x\}$

In (3.5), the delta functions denote the conditions of fixed A and fixed T that we wish to impose on the trajectory ensemble. This conditioning defines the *microcanonical path ensemble* [33], of which (3.5) is the normalization constant.

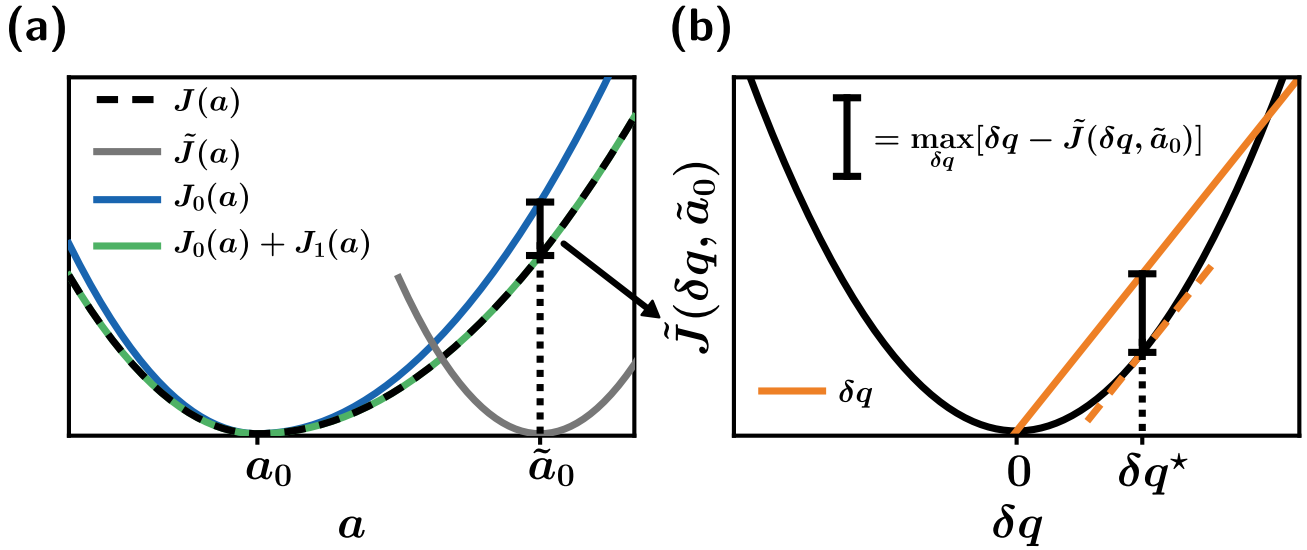


Figure 3.1: Large deviations from a variational ansatz for rare dynamics (VARD). (a) We aim to bound or calculate the large-deviation rate function $J(a)$ (black dashed line) for a given model and observable a , under the continuous-time dynamics (4.2) and (3.4). We introduce a reference model (3.7) and (3.9), a variational ansatz for the rare dynamics of the original model conditioned upon a . The reference model has rate function $\tilde{J}(a)$ (gray line; we do not aim to compute this function). The typical value of a generated by the reference model is \tilde{a}_0 ; this is potentially far from the typical value a_0 generated by the original model. Evaluation of (3.17) from the sample mean of a single trajectory of the reference model produces one point $J_0(\tilde{a}_0)$ on the blue line, an upper bound on $J(a)$. (b) If we can evaluate the auxiliary rate function $\tilde{J}(\delta q, \tilde{a}_0)$ at the point δq^* at which its gradient is unity, then we can calculate the correction term (3.18) and determine one point on the green curve in panel (a), the exact rate function of the original model. If not, then we gain information about the quality of the bound $J_0(\tilde{a}_0)$. Variation of the parameters of the reference model allows reconstruction of the entire blue and (potentially) green curves in panel (a). VARD thus reduces a single nonlocal problem, the computation of $J(a)$ arbitrarily far from a_0 , to a series of local problems, each requiring the evaluation of an auxiliary rate function $\tilde{J}(\delta q, \tilde{a}_0)$ at the point δq^* at which its gradient is unity. As we show in this paper, this procedure can be carried out for models commonly found in the literature using relatively simple choices of reference model.

We focus on models for which, for large values of T , the probability distribution (3.5) adopts the large-deviation form (3.1). Our aim is to calculate the rate function $J(a)$ (sometimes the notation $I(a)$ or $\varphi(a)$ is used to denote a rate function [28, 56]). This function quantifies the rate of decay of atypical values of a . For many models $J(a)$ has a unique minimum at a point $a = a_0$, where $J(a_0) = 0$. This point defines the typical value of a : the distribution $\rho_T(A)$ concentrates on a_0 in the long-time limit, an expression of the law of large numbers [27, 28]. In general, a rate function can have more than one point at which it is zero, defining multiple typical values of an observable [28, 41, 70]. Often, the rate function is quadratic in the neighborhood of its minimum, an expression of the central-limit theorem [27, 28]. Exceptions to this norm occur at phase transitions, where the usual central-limit theorem does not hold [71]. Far from their minima, rate functions display a variety of behaviors [28]. However, direct simulation of the dynamics (4.2) and (3.4) leads to poor sampling of $J(a)$ anywhere other than in the neighborhood $a \approx a_0$.

Quantifying rare events

To remedy the sampling problem for values of the observable a far from a_0 , we introduce a *reference model*. We wish to reweight the trajectories of the reference model in order to approximate or calculate $J(a)$ for values of a potentially far from a_0 . The reference model must satisfy certain requirements. It needs to be able to generate all trajectories possible in the original model, but no trajectories not possible in the original model (otherwise the reweighting factor, discussed below, can be infinity or zero). We want the reference model to be able to generate trajectories possessing values of a that are rarely generated by the original model, which is relatively easy to arrange, but we also need to be able to recover from reference-model trajectories the probability with which such trajectories *would* have been generated by the original model. This second requirement is harder to arrange, but not prohibitively so. As we show, if the reference model generates trajectories possessing values of a in a manner completely unlike the original model, then we have to do prohibitively heavy sampling of reference-model trajectories in order to calculate $J(a)$. If, however, the reference model generates trajectories possessing values of a in a manner similar to the original model, then $J(a)$ can be reconstructed from trajectories of the reference model with relatively little effort. Importantly, the method tells us when this is so: we do not need to know in advance the precise nature of the rare dynamics of the original model in order to recover $J(a)$.

For a trajectory ω of the reference model we want to be able to influence how much

of the dynamical observable is produced per jump, $A(\omega)/K(\omega)$, and the number of jumps per unit time, $K(\omega)/T$. To control the former we use a reference-model dynamics that selects destination states with probability

$$\tilde{p}_{xy} = \frac{\tilde{W}_{xy}}{\tilde{R}_x}, \quad (3.7)$$

where \tilde{W}_{xy} is an effective rate, and $\tilde{R}_x = \sum_{y \neq x} \tilde{W}_{xy}$. (The true rates of the reference model are, from (3.7) and (3.9), $\tilde{W}_{xy}(R_x + \lambda)/\tilde{R}_x$.) Here we use the parameterization

$$\tilde{W}_{xy} = e^{-s\alpha_{xy} - \beta_{xy}} W_{xy}, \quad (3.8)$$

which is a modification of (4.2). The factor $e^{-s\alpha_{xy}}$ is chosen in order to guide the jump destination according to the change of the observable α_{xy} weighted by a parameter s . In general such a bias is not sufficient to control $A(\omega)/K(\omega)$, and so we also consider an additional arbitrary bias, β_{xy} . For the models considered here a simple and physically-motivated guess for what β_{xy} should be is sufficient to produce a good reference model. We shall return to this point.

To control the number of jumps per unit time, $K(\omega)/T$, we draw times between jumps of the reference model from the distribution

$$\tilde{p}_x(\Delta t) = (R_x + \lambda)e^{-(R_x + \lambda)\Delta t}, \quad (3.9)$$

where $\lambda > -\min_x R_x$ serves to make the jump time from a given state unusually large or small by the reckoning of the original model. This ‘‘clock trick’’ provides a simple way of sampling jump times without having those times appear explicitly in the reweighting factor [43]. (The parameter β_{xy} can also affect jump times indirectly, if, for example, it is chosen to be proportional to R_y , the escape rate from the destination state.)

Next observe that the path weight $p(\omega)$ in (3.5) can be written $\tilde{p}(\omega)\phi(\omega)$, where $\phi(\omega) = p(\omega)/\tilde{p}(\omega)$ is the reweighting factor, the ratio of weights of a trajectory ω in the original and reference models. $\phi(\omega)$ is also known as the likelihood ratio or the Radon-Nikodym derivative [33, 52]. For a jump $x \rightarrow y$ in time Δt , the reweighting factor is the product of (4.2) and (3.4), divided by the product of (3.7) and (3.9); for the entire trajectory ω we have

$$\phi(\omega) = e^{sA(\omega) + \lambda T(\omega) + Tq(\omega)}, \quad (3.10)$$

where

$$q(\omega) = \frac{1}{T} \sum_{k=0}^{K(\omega)-1} \left(\beta_{x_k x_{k+1}} + \ln \frac{\tilde{R}_{x_k}}{R_{x_k} + \lambda} \right) \quad (3.11)$$

is the piece of ϕ that is not fixed by the delta-function constraints in (3.5). (The time-dependent piece of (3.10) produced by $K(\omega)$ jumps is $e^{\lambda T_K(\omega)}$; the contribution from the final entry in the path weight, the probability of not jumping between time $T_K(\omega)$ and $T(\omega)$, leads to the factor of $e^{\lambda T(\omega)}$ shown in (3.10).)

We can then write (3.5) in the form

$$\frac{\rho_T(A)}{\tilde{\rho}_T(A)} = e^{sA+\lambda T} \frac{\sum_{\omega} \tilde{p}(\omega) e^{Tq(\omega)} \delta(T) \delta(A)}{\sum_{\omega} \tilde{p}(\omega) \delta(T) \delta(A)}, \quad (3.12)$$

where $\tilde{\rho}_T(A) \approx e^{-T\tilde{J}(a)}$ is the analog of (3.5) for the reference model, and we have used the shorthand $\delta(X) \equiv \delta(X(\omega) - X)$. Replacing the sums over trajectories with an integral over trajectory weights gives

$$\frac{\rho_T(A)}{\tilde{\rho}_T(A)} = e^{sA+\lambda T} \int dq \tilde{p}_T(q|a) e^{Tq}, \quad (3.13)$$

where $\tilde{p}_T(q|a)$ is the normalized probability distribution of $q(\omega)$ for trajectories of the reference model that have specified values of a and T . For large T we assume that this distribution will obey a large-deviation principle of its own. If so we can write, using the rules of conditional probability,

$$\tilde{p}_T(q|a) \approx e^{-T\tilde{J}(q|a)} = e^{-T[\tilde{J}(q,a) - \tilde{J}(a)]}, \quad (3.14)$$

where $\tilde{J}(q, a)$ is the joint rate function for q and a within the reference model.

We next take the large- T limit in (3.13), replace all probability distributions with their large-deviation forms, and set $a = \tilde{a}_0$, the value typical of the reference model (such that $\tilde{J}(\tilde{a}_0) = 0$). The result, upon taking logarithms, is

$$J(\tilde{a}_0) = -s\tilde{a}_0 - \lambda - \lim_{T \rightarrow \infty} T^{-1} \ln \int dq e^{T[q - \tilde{J}(q, \tilde{a}_0)]}. \quad (3.15)$$

Finally, we introduce $\delta q \equiv q - \tilde{q}_0$, where \tilde{q}_0 is the value of q typical of the reference model. This value can be computed from a single reference-model trajectory (for a given set of parameters s, λ, β_{xy}). Extracting $e^{T\tilde{q}_0}$ from the exponential in (3.15) and evaluating the integral using the saddle-point method yields

$$J(\tilde{a}_0) = J_0(\tilde{a}_0) + J_1(\tilde{a}_0), \quad (3.16)$$

where

$$J_0(\tilde{a}_0) = -s\tilde{a}_0 - \lambda - \tilde{q}_0 \quad (3.17)$$

and

$$J_1(\tilde{a}_0) = -\max_{\delta q} [\delta q - \tilde{J}(\delta q, \tilde{a}_0)]. \quad (3.18)$$

Eqs.(3.16)–(3.18) provide an exact representation of the rate function, if the probability distributions (3.5) and (3.14) adopt large-deviation forms ³. Fig. 3.1 illustrates the relationship between Equations (3.16), (3.17), and (3.18), which are central to the sampling scheme discussed in this paper.

We can compute $J(a)$ as the sum of a bound and a correction

The piece $J_0(\tilde{a}_0) \geq J(\tilde{a}_0)$, Eq. (3.17), is an upper bound on the rate function at the point $a = \tilde{a}_0$, by Jensen’s inequality applied to (3.13), and can be obtained from the sample mean of single trajectory of the reference model. It is always possible to calculate this term. If $\tilde{J}(a)$ is locally quadratic about \tilde{a}_0 , meaning that the usual central-limit theorem holds ⁴, then errors in the computation of \tilde{a}_0 go as $\sqrt{\langle (a - \tilde{a}_0)^2 \rangle} \sim T^{-1/2}$. The same is true for the computation of \tilde{q}_0 . Thus statistical errors in the computation of the bound can be made negligible simply by computing (3.17) for a sufficiently long trajectory.

The term $J_1(\tilde{a}_0)$, Eq. (3.18), is a correction to the bound, and can be calculated by sampling values of q , Eq. (3.11), of trajectories of the reference model that have $a = \tilde{a}_0$. It is possible to calculate this term if the reference model is chosen well, but not if it is chosen badly.

The two terms in (3.18) describe a competition between the logarithmic weight δq associated with reference-model trajectories that have atypical values of q , and the logarithmic probability $\tilde{J}(\delta q, \tilde{a}_0)$ of observing such trajectories. When $\tilde{J}(\delta q, \tilde{a}_0)$ is differentiable, (3.18) can be written

$$J_1(\tilde{a}_0) = -\delta q^\star + \tilde{J}(\delta q^\star, \tilde{a}_0), \quad (3.19)$$

where

$$\partial_{\delta q} \tilde{J}(\delta q, \tilde{a}_0)|_{\delta q = \delta q^\star} = 1. \quad (3.20)$$

Thus we need to measure the value of $\tilde{J}(\delta q, \tilde{a}_0)$ at the point δq^\star at which its gradient is unity, which will be a unique point when $\tilde{J}(\delta q, \tilde{a}_0)$ is convex. The sampling problem is now *localized*: instead of sampling $J(a)$ arbitrarily far from a_0 (using the original model), we need only sample a specific piece δq^\star of an auxiliary rate function, $\tilde{J}(\delta q, \tilde{a}_0)$ (using the reference model). This fact, summarized in

³In an abuse of notation we have, for brevity, changed from writing the joint rate function in the form $\tilde{J}(q, a)$ in (3.15) to $\tilde{J}(\delta q, a)$ in (3.18) and subsequently.

⁴Note that the reference model can be well behaved in this manner even when the *original* model exhibits anomalous fluctuations such that $J(a)$ is not quadratic about its minimum [41].

Fig. 3.1, shows why the present scheme has the potential to be much more efficient than unbiased simulation, if the reference model is chosen well.

This sampling problem is still formidable in general. If the reference model is chosen badly, meaning that its typical trajectories have very different character to trajectories of the original model that have $a = \tilde{a}_0$, then the bound will be slack, meaning that $J_0(\tilde{a}_0) \gg J(\tilde{a}_0)$, and so $J_1(\tilde{a}_0)$ will be large. In this case $\tilde{J}(\delta q, \tilde{a}_0)$ will be broad around its minimum $\delta q = 0$ (the variance of δq will be large) and unreasonably heavy sampling using the reference model will be required to determine the point δq^* (because this corresponds to a rare event within the reference model).

However, for good choices of the reference model the opposite situation arises: the bound will be tight, meaning that $J_0(\tilde{a}_0) \approx J(\tilde{a}_0)$, and so $J_1(\tilde{a}_0)$ will be small. In this case the latter can be evaluated with reasonable numerical effort (in the examples that follow we can gather the required statistics of q by sub-sampling a single trajectory of the reference model). If we can reconstruct $\tilde{J}(\delta q^*, \tilde{a}_0)$ then we can calculate $J_1(\tilde{a}_0)$ and we have obtained the exact rate function.

Computing the correction

Given a model and an observable a , we construct a reference model (3.7) and (3.9) so as to approximate or calculate $J(a)$. In Section 3.3 we provide a set of worked examples of this procedure. In general terms we simply guess which rates of the original model can be modified so as to produce more or less of a than usual, and introduce a parameter (s , λ , or β_{xy}) able to control the rate in question. We do not know in advance which combination of these modified rates best approximates the way in which the original model produces rare values of a , but by running short trajectories of the reference model for different values of its parameters we can identify how this is done within the space of possibilities defined by the reference model. From the sample mean of each reference-model trajectory we obtain the values \tilde{a}_0 and \tilde{q}_0 ; plotting \tilde{a}_0 against $-s\tilde{a}_0 - \lambda - \tilde{q}_0$ for a range of values of reference-model parameters, and identifying the lower envelope of these points (conveniently calculated using a union of convex hull constructions), gives the bound $J_0(a)$ associated with that choice of reference model.

This bound is the starting point for our attempt to calculate the correction $J_1(a)$. The correction term can be interpreted as a measure of how close the typical dynamics of the reference model is to the desired rare dynamics of the original model. If $J_1(a) = 0$ then typical trajectories of the reference model correspond exactly to trajectories of

the original model conditioned on the relevant value a of the order parameter. If J_1 is small then (slightly) atypical versions of reference-model trajectories correspond to the desired rare dynamics; and if J_1 is large (or cannot be calculated) then it is the very rare trajectories of the reference model that correspond to the desired rare dynamics of the original model.

In previous versions of our sampling method [41–43] we used a cumulant expansion to evaluate the integral in (3.15), giving, in place of (3.18),

$$J_1^{\text{approx}}(\tilde{a}_0) = \frac{T}{2}\sigma_{\text{ref}}^2 + \frac{T^2}{6}\kappa_{\text{ref}} + \dots \quad (3.21)$$

Here $\sigma_{\text{ref}}^2 \propto 1/T$ is the variance of δq over typical trajectories of the reference model (those having $a = \tilde{a}_0$), i.e. $\sigma_{\text{ref}}^2 = \langle (\delta q)^2 \rangle_{\text{ref}}$, and $\kappa_{\text{ref}} = \langle (\delta q)^3 \rangle_{\text{ref}} \propto 1/T^2$. Eq. (3.21) can give accurate results for the rate-function correction [41–43], but does not provide a self-consistent way of determining *when* the correction is accurate. At best we can determine that the first omitted term in the expansion (3.21) is small, but this does not provide a proof of convergence.

In this paper we present an alternative way to calculate the correction term (3.18), which builds upon methods designed to compute rate functions (or their SCGF Legendre duals) empirically [62, 72]. This process is more involved than the computations required to evaluate (3.21), but has the advantage of providing a set of clear convergence criteria and statistical error bars. This information reveals when we have converged (3.18), and so have the exact rate function, and when we do not, thus turning the reference-model guess into a true ansatz. In the remainder of this section we describe the method we use to compute (3.18). We have provided a GitHub script [63] for calculating the correction automatically.

To obtain the correction we first assume that $\tilde{J}(\delta q, a)$ is differentiable, and so work with (3.19) instead of (3.18). We then introduce the two-dimensional scaled cumulant-generating function (SCGF),

$$\tilde{\theta}(k_{\delta q}, k_a) \equiv \lim_{T \rightarrow \infty} T^{-1} \ln \langle e^{T(k_{\delta q} \delta q + k_a a)} \rangle_{\text{ref}}, \quad (3.22)$$

where the angle brackets denote a trajectory ensemble average within the reference model. The SCGF (3.22) is related to $\tilde{J}(\delta q, a)$ through the double Legendre transform

$$\tilde{J}(\delta q, a) = k_{\delta q} \delta q + k_a a - \tilde{\theta}(k_{\delta q}, k_a), \quad (3.23)$$

where $k_{\delta q}$ and k_a are conjugate to δq and a respectively. As a result, if we want to calculate $\tilde{J}(\delta q, a)$ at a single point, we can calculate the right-hand side of (3.23).

Doing so is much more efficient than attempting to reconstruct $\tilde{J}(\delta q, a)$ directly, for the reasons given in Section 3.2.

The formula for the correction (3.19) depends on $\tilde{J}(\delta q^*, \tilde{a}_0)$, which we can get from (3.23):

$$\tilde{J}(\delta q^*, \tilde{a}_0) = k_{\delta q^*} \delta q^* + k_{\tilde{a}_0} \tilde{a}_0 - \tilde{\theta}(k_{\delta q^*}, k_{\tilde{a}_0}). \quad (3.24)$$

We can simplify this relationship by combining the implicit definition of $k_{\delta q}$ in the Legendre transform with (3.20) to get

$$k_{\delta q^*} = \partial_{\delta q} \tilde{J}(\delta q, \tilde{a}_0)|_{\delta q = \delta q^*} = 1. \quad (3.25)$$

Inserting (3.25) into (3.24) yields

$$\tilde{J}(\delta q^*, \tilde{a}_0) = \delta q^* + k_{\tilde{a}_0} \tilde{a}_0 - \tilde{\theta}(1, k_{\tilde{a}_0}). \quad (3.26)$$

The quantity \tilde{a}_0 is the typical value of the observable in the reference model, and can be obtained from a single reference-model trajectory. The three other unknown quantities on the right-hand side of (3.26) that are needed for the correction are δq^* , $k_{\tilde{a}_0}$, and $\tilde{\theta}(1, k_{\tilde{a}_0})$.

To calculate these quantities we have to compute the value of the two-dimensional SCGF (3.22) at various points $(k_{\delta q}, k_a)$. We can do this using a simple extension of existing techniques developed to sample points on 1D SCGFs [62, 72]. Following Ref. [62] we generate a single long trajectory of the reference model and sub-sample it into M approximately independent blocks ω_i of length $T(\omega_i) = B$. Within each block we record the sample mean of δq and a , which we write as δq_i and a_i . $\tilde{\theta}(k_{\delta q}, k_a)$ can be calculated from this data set using the estimator

$$\hat{\theta}(k_{\delta q}, k_a) = \frac{1}{B} \ln \left(\frac{1}{M} \sum_{i=1}^M e^{B(k_{\delta q} \delta q_i + k_a a_i)} \right). \quad (3.27)$$

Eq. (3.27) is guaranteed to converge to the exact value of the SCGF, $\tilde{\theta}(k_{\delta q}, k_a)$, in the limit $M \rightarrow \infty$ and $B \rightarrow \infty$. The convergence properties of this estimator for finite M and B will be addressed in the next section, 3.2. For now we assume that we can obtain convergence as needed. Finally, note that by changing the values of $k_{\delta q}$ and k_a in (3.27) a single data set consisting of values of a_i and δq_i , generated from a single long trajectory, can be used to recover many points $(k_{\delta q}, k_a)$ on $\tilde{\theta}(k_{\delta q}, k_a)$.

We now turn to the calculation of the three unknowns in (3.26), δq^* , $k_{\tilde{a}_0}$ and $\tilde{\theta}(1, k_{\tilde{a}_0})$. First we use the relation

$$\tilde{a}_0 = \partial_{k_a} \tilde{\theta}(k_{\delta q^*} = 1, k_a)|_{k_a = k_{\tilde{a}_0}} \quad (3.28)$$

to find $k_{\tilde{a}_0}$. We do so by calculating the SCGF, $\tilde{\theta}(k_{\delta q}, k_a)$, along a 1D slice through its 2D domain using the estimator (3.27). This slice is defined by fixing $k_{\delta q} = k_{\delta q^*} = 1$ and varying k_a . We then use the method of finite differences to get $\partial_{k_a} \tilde{\theta}(k_{\delta q^*} = 1, k_a)$ at each point k_a , and find the point that fulfills (3.28). Once we know the value of $k_{\tilde{a}_0}$ we can calculate $\tilde{\theta}(1, k_{\tilde{a}_0})$, again using (3.27). Finally we can compute δq^* using the analog of (3.28) for δq ,

$$\delta q^* = \partial_{k_{\delta q}} \tilde{\theta}(k_{\delta q}, k_{\tilde{a}_0})|_{k_{\delta q}=1}. \quad (3.29)$$

Inserting δq^* , $k_{\tilde{a}_0}$, $\tilde{\theta}(1, k_{\tilde{a}_0})$, and \tilde{a}_0 into (3.26) yields $\tilde{J}(\delta q^*, \tilde{a}_0)$. The correction to the bound, $J_1(\tilde{a}_0)$, then follows from (3.19).

Convergence of the SCGF Estimator

When used with only a finite number M of blocks of finite length B , the estimator $\hat{\theta}(k_{\delta q}, k_a)$, defined in (3.27), can exhibit statistical and systematic errors. In this section, we analyze these errors to understand when the estimate of $J_1(\tilde{a}_0)$ calculated through the SCGF (3.22) will be accurate. As in the previous subsection, this analysis closely follows Ref. [62].

To quantify the statistical error associated with our calculated value of $J_1(\tilde{a}_0)$ we repeat the calculation procedure using R independent trajectories. Each of these trajectories is split up into M blocks of length B , and used to calculate $J_1(\tilde{a}_0)$. Our final estimate for the correction is then

$$\hat{J}_1(\tilde{a}_0) = \frac{1}{R} \sum_{j=1}^R J_1^{(j)}(\tilde{a}_0), \quad (3.30)$$

where $J_1^{(j)}(\tilde{a}_0)$ is the value of the correction calculated from the j^{th} trajectory. The statistical error of (3.30) can be estimated using

$$\text{Err}[\hat{J}_1(\tilde{a}_0)] = \sqrt{\frac{\text{Var}[\hat{J}_1(\tilde{a}_0)]}{R}}. \quad (3.31)$$

This statistical error is only meaningful if we know that the systematic error in the calculation is comparatively small. There are two sources of systematic error that arise when using (3.27): correlation error and linearization error. Correlation error results from the fact that the derivation of the estimator assumes that the trajectory blocks are long enough to be approximately independent. This will be true if $B > T_{\text{corr}}$ where T_{corr} is the correlation time of the reference model. If, however, the

sub-sampled blocks of a trajectory are correlated, meaning that $B < T_{\text{corr}}$, then we will not obtain an accurate estimate of $\tilde{\theta}(k_{\delta q}, k_a)$ even as $M, R \rightarrow \infty$.

One way to resolve this correlation issue is to increase the block time B , but this also increases the magnitude of the other systematic source of error, linearization error. Linearization error is a manifestation of the fact that trajectories that contribute most to the average in the SCGF (3.22) for $k_a, k_{\delta q} \neq 0$ have atypical values of δq and a . Using larger B creates more self-averaging within a single trajectory and, as a result, makes sampling these atypical values more difficult. Linearization error also increases for fixed B with increasing $|k_a|$ and $|k_{\delta q}|$, because larger values of these parameters weight rare trajectories' contributions to the SCGF more heavily. Ref. [62] contains a detailed discussion of these problems. The authors of that work describe a method for checking to see if linearization error will substantially influence the estimate of the SCGF at a point $(k_{\delta q}, k_a)$ for some fixed B . We use this check, modified to account for the fact that our SCGF is two dimensional, as follows.

First, we calculate the SCGF (3.27) along another 1D slice through its 2D domain. This slice is defined by fixing $k_{\delta q} = 0$ and increasing k_a , starting from $k_a = 0$ ⁵. By using finite difference along this slice we can calculate how a varies with k_a . To compute the statistical error, we generate R independent trajectories (usually the same R trajectories we used to get (3.31)), split each one into M blocks of length B , and use each data set to calculate $a(k_a)$ along the slice. Our final estimate for the value of a at each k_a is

$$\hat{a}(k_a) = \frac{1}{R} \sum_{j=1}^R a^{(j)}(k_a), \quad (3.32)$$

where $a^{(j)}(k_a)$ is calculated from the j^{th} trajectory.

We will not end up using the $\hat{a}(k_a)$ values themselves. Instead, we focus on the associated values of the statistical error, calculated in the same way as the error of (3.27),

$$\text{Err}[\hat{a}(k_a)] = \sqrt{\frac{\text{Var}[\hat{a}(k_a)]}{R}}. \quad (3.33)$$

A plot of $\text{Err}[\hat{a}(k_a)]$ as a function of k_a will peak at some point $\hat{k}'_a(B)$ and then decline. Again $k_{\delta q} = 0$ is fixed during this entire calculation. As discussed

⁵The choice of moving in the positive k_a direction is arbitrary. Moving in the negative k_a direction will yield an equivalent convergence criterion (similarly we can move in either the positive or negative $k_{\delta q}$ directions while holding $k_a = 0$).

in Ref. [62], $\hat{k}'_a(B)$ is an estimate for the maximum value $k'_a(B)$ at which the calculation of the SCGF will converge without being overwhelmed by linearization error. $k'_a(B)$ is a decreasing function of B , because linearization error grows as B is increased.

Next we note that $\tilde{\theta}(k_{\delta q} = 0, k'_a)$ corresponds to a point on the rate function $\tilde{J}(a')$, via the Legendre transform (3.23). If we can converge the value of $\tilde{J}(a')$ then we can, with the same data set, also converge the value of $\tilde{J}(\delta q, a)$ at any point for which

$$\tilde{J}(\delta q, a) < \tilde{J}(a'). \quad (3.34)$$

This statement is intuitive in the context of probabilities and rate functions. However, it also applies when working with the SCGF, provided that $\tilde{J}(\delta q, a)$ is convex [38]. Thus the value of a point $\hat{\theta}(k_{\delta q}, k_a)$ estimated using (3.27) will be unaffected by linearization error if the associated point on the rate function, $\hat{J}(\delta q, a)$, satisfies

$$\hat{J}(\delta q, a) < \xi \hat{J}(a'), \quad (3.35)$$

where $\xi < 1$ is an empirical constant (we set $\xi = 0.8$). The terms \hat{J} in (3.35) are averages over R independent data sets of the corresponding Legendre transform (3.23). This formula allows the convergence criteria derived in [62] for estimating one-dimensional SCGFs and rate functions to be applied in an arbitrary number of dimensions.

We now discuss the procedure we use to converge the correction (3.19) while accounting for correlation and linearization errors. For fixed block time B we first increase M and R until the error bars for $\hat{J}_1(\tilde{a}_0)$, (3.33), are smaller than a desired value. We repeat this process for larger and larger B until $\hat{J}_1(\tilde{a}_0)$ becomes independent of B . This is equivalent to increasing B until it becomes larger than the reference-model correlation time T_{corr} . If this happens while the convergence criterion (3.35) holds at $\tilde{J}(\delta q^*, \tilde{a}_0)$ then the calculation has succeeded, and we have computed (to within statistical error) the exact value of the correction $J_1(\tilde{a}_0)$.

If, however, the convergence criterion (3.35) fails to hold in the regime in which (3.27) still changes rapidly with B , then the bound $J_0(\tilde{a}_0)$ is too far from the exact answer for us to effectively sample $J_1(\tilde{a}_0)$ using direct simulation of the reference model. In this case the chosen ansatz is probably missing a crucial piece of the physics of the rare trajectories of the original model. On several occasions our failure to converge $J_1(\tilde{a}_0)$ based on an initial guess led us to construct a modified ansatz from which we could converge the exact correction. In the cases described

in this paper we were able to reconstruct $J(a)$ using physically transparent ansätze containing only a modest number of parameters.

A quick way to estimate the scale of the correction is to compute the first term in (3.21), which requires computing only the variance of δq within the reference model. By the central limit theorem we will have $\tilde{J}(\delta q, \tilde{a}_0) \approx (\delta q)^2 / (2T\sigma_{\text{ref}}^2)$ close enough to the origin, where $\sigma_{\text{ref}}^2 \propto 1/T$ is the variance of q within the reference model. If σ_{ref}^2 is small (which is the case when the ansatz is very good) then the correction $J_1(\tilde{a}_0) \approx T\sigma_{\text{ref}}^2/2$. Thus if $T\sigma_{\text{ref}}^2/2$ looks small when plotted in the form of Fig. 3.1 it might be worth attempting to compute the correction (3.18). If not, a better reference model ansatz is probably required.

Efficiency of the correction calculation

Standard arguments are often used to suggest that computing the exact value of $J(a)$ is not possible without knowledge of the exact rare dynamics, or the use of methods such as cloning or transition-path sampling. This claim is based on the fact that computing $J(a)$ requires computation of the integral in (3.15), and assumes that because the integrand grows exponentially with T , the number of trajectories required to converge this expression as $T \rightarrow \infty$ is prohibitively large. While this latter statement is correct, it does not speak directly to the task at hand. To compute the integral we do not need to take $T \rightarrow \infty$. Instead, we need $T \gtrsim T'$ where T' is smallest time at which the large deviation principle applies. Taking $T \gg T'$ makes sampling more difficult and is unnecessary. It is possible for T' to be large, but if the reference-model dynamics are close enough to the rare dynamics of the original model then the variance of the q will be small and it will be possible to converge this integral term without using an unreasonable number of trajectories.

Moreover, computing the correction is numerically cheaper than inspection of the integral alone might suggest. If we switch to the SCGF representation, (3.22), we can instead work with trajectories of length $T = T_{\text{corr}}$, where T_{corr} is the correlation time of the reference model (in practice these trajectories are constructed by sub-sampling a single longer trajectory). Generally, T_{corr} is much smaller than T' , the time required for the large-deviation principle to apply, and so sampling the moderately rare events required to reconstruct the auxiliary rate function $\tilde{J}(\delta q, a)$ near its minimum is cheaper in the SCGF representation. This property is ideal for the present method because we have reduced the problem of sampling $J(a)$ arbitrarily far from its minimum to one of sampling $\tilde{J}(\delta q, \tilde{a}_0)$ (potentially) close to

its minimum. Working with the SCGF also removes the constraint $a = \tilde{a}_0$ present in (3.18). Finally, we note that we are calculating the SCGF that is Legendre dual to the correction term (3.18), and not the SCGF that is Legendre dual to the original rate function $J(a)$. Thus our method can in principle reproduce rate functions $J(a)$ that are not convex (J_0 is not required to be convex).

Summary – A variational ansatz for rare dynamics (VARD)

1. Given a continuous-time dynamics with rates W_{xy} and a path-extensive dynamical observable a , we wish to determine $J(a)$, the large-deviation rate function for a for trajectories of the model W_{xy} of fixed time (assuming that $J(a)$ exists). We use a reference dynamics to calculate $J(a)$ as the sum of an upper bound $J_0(a)$ and a correction $J_1(a)$. The bound can always be calculated, and the correction can be calculated if the criteria described in Section 3.2 hold. If so then we succeed in calculating $J(a)$; if not, then the method returns an upper bound $J_0(a) \geq J(a)$.
2. Determine a reference-model dynamics (3.7) and (3.9) able to produce more or less of a than the original model. In this paper we set the arbitrary bias β_{xy} using physical intuition.
3. Run a set of reference-model trajectories for different values of the reference-model parameters (s, λ, β_{xy}) . For each trajectory, evaluate \tilde{a}_0 and \tilde{q}_0 , using Eqs. (3.6) and (3.11), and then use Eq. (3.17) to plot the point $(\tilde{a}_0, J(\tilde{a}_0))$; see Fig. 3.1(a). The lower envelope of these points over values of the reference-model parameter set is the tightest upper bound on $J(a)$ associated with the ansatz chosen in Step 1.
4. Attempt to calculate the correction $J_1(a)$ at points on the bound by running a few (~ 5) trajectories for each reference model. With the data from each trajectory, calculate $\tilde{J}(\delta q^*, \tilde{a}_0)$, Eq. (3.26), using Eqs. (3.27), (3.28) and (3.29). Insert the resulting values into Eq. (3.19). Calculate the averaged correction $\hat{J}_1(a)$ and associated statistical error using Eqs. (3.30) and (3.31).
5. To verify convergence, repeat the calculation of Step 3 for increasing values of the block time B , until the averaged estimate for the correction Eq. (3.30) no longer changes with B , and the convergence criterion (3.35), with $\delta q = \delta q^*$

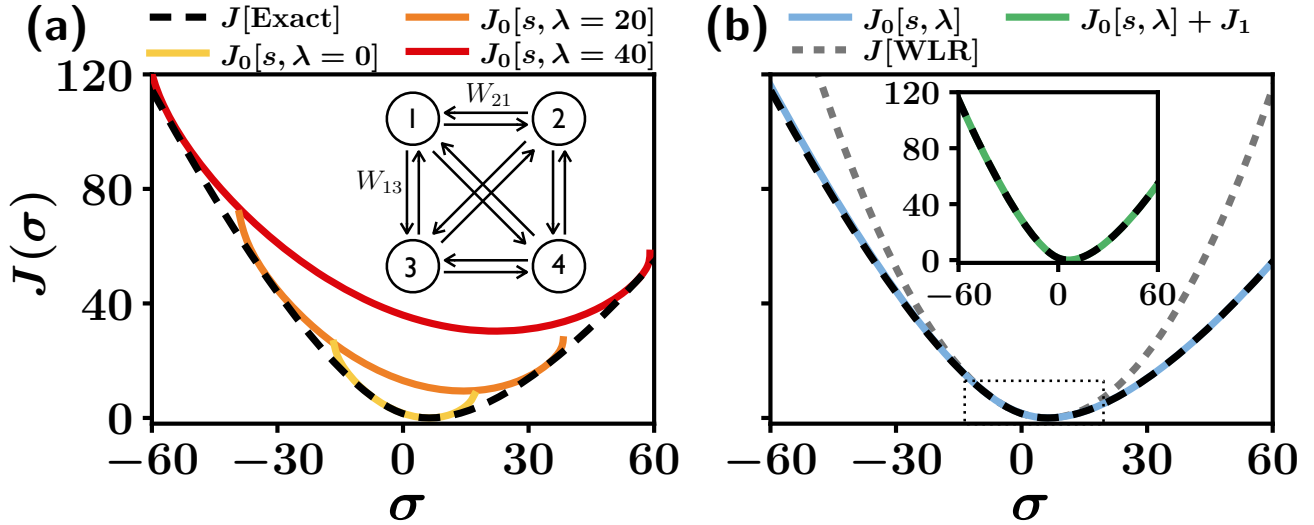


Figure 3.2: Entropy production rate σ for the 4-state model of Ref. [55], the rates W_{xy} of which are given by (3.36). (a) Bounds (3.17) for the large-deviation rate function $J(\sigma)$. Each point on the colored lines results from a reference-model dynamics [Eqns. (3.7) and (3.9)] obtained by scanning the indicated parameters. The black dashed line is the exact answer. (b) Bound (blue line) resulting from a scan of the parameters s and λ compared with the WLR bound of Ref. [55], Eq. (3.37). Inset: The sum (green line) of the bound and the correction (3.18) equals the exact rate function, arbitrarily far into its tails. The boxed region in panel (b) indicates the scale of Fig. 2 of Ref. [55]. Error bars for both axes are smaller than the thickness of the lines.

and $a = \tilde{a}_0$, holds ⁶. The accompanying GitHub script [63] performs steps 4 and 5 automatically.

3.3 VARD applied to four examples

Summary of the section

We now apply the method to four models taken from the literature. In each case, a simple and physically-motivated ansatz for the modified dynamics allows computation of the exact rate function $J(a)$. We focus on models whose state space is small enough that the exact rate function can be computed by standard methods – Legendre transform of the SCGF calculated using the largest eigenvalue of the tilted rate matrix [28] – in order to validate our method (at the end of the section we also

⁶The quantity $\hat{J}(a')$ on the right-side of (3.35) is determined from the Legendre transform (3.23) of $\hat{\theta}(k_{\delta q} = 0, k_a = \hat{k}'_a)$. The quantity \hat{k}'_a is calculated by finding the maximum of $\text{Err}[\hat{a}(k_a)]$, Eq. (3.33), while starting at the point $(k_{\delta q} = 0, k_a = 0)$ on the SCGF and scanning outwards by increasing k_a .

use VARD to compute descriptive rate-function bounds for two systems too large to solve by matrix diagonalization). In figures, the exact rate function is shown as a black dashed line. Absent the exact answer we would apply the method in exactly the same way. For a given reference model the fluctuations of the quantity q reveal whether the bound $J_0(a)$ is tight, and whether we can compute $J(a)$ exactly.

Entropy production in a 4-state model

We start by sampling entropy production in the 4-state model of Ref. [55], shown in the inset of Fig. 3.2(a). This is a fully-connected network model with transition rates

$$\begin{aligned}
 W_{12} &= 3, & W_{13} &= 10, & W_{14} &= 9, \\
 W_{21} &= 10, & W_{23} &= 1, & W_{24} &= 2, \\
 W_{31} &= 6, & W_{32} &= 4, & W_{34} &= 1, \\
 W_{41} &= 7, & W_{42} &= 9, & W_{43} &= 5.
 \end{aligned} \tag{3.36}$$

These rates do not satisfy detailed balance, and so the model produces nonzero entropy on average. To quantify the fluctuations of entropy production for trajectories of fixed time we construct a reference model as follows. The dynamical observable is $a = \sigma = T^{-1} \sum \alpha_{xy}$, where the sum is taken over all jumps $x \rightarrow y$ of a trajectory, and $\alpha_{xy} = \ln(p_{xy}/p_{yx})$, where $p_{xy} = W_{xy}/\sum_y W_{xy}$. Our basic reference-model parameterization is defined by the parameters s and λ appearing in (3.7) and (3.9), together with any additional set of biases β_{xy} suggested by the physics of the problem under study. Here we reason that none is necessary: the bias λ is always required, in order to sample jump times, and the bias s is sufficient to influence the entropy produced per jump, A/K (a fact that is easy to guess, and to confirm with some short simulations). We therefore impose no additional bias, and set $\beta_{xy} = 0$.

We ran trajectories for a fixed number $K = 1.5 \times 10^8$ of events, roughly equivalent to a time of $T = 10^7$ in the unbiased model. We simulate in the constant-event ensemble for convenience, because there all simulations, regardless of the value of λ , take approximately the same amount of processor time. The equations of Section 3.2 then allow us to compute the rate function for the original model in the constant-time ensemble (see Ref. [73] for more on the relationship between the constant-event and constant-time ensembles).

The bounds $J_0(a)$ resulting from a scan of s , for three values of λ , are shown as colored lines in Fig. 3.2(a). In figures we use the compact notation $J_0[x]$ to indicate the bound $J_0(a)$ swept out by scanning the set of parameters $\{x\}$. We also

show the exact rate function (black dashed line), obtained by matrix diagonalization. Different combinations of s and λ produce the best (lowest) bound at different values of a , so indicating the “least unlikely way” of realizing each value of a within the manifold of dynamics accessible to the reference model. The bound produced by the scan $\lambda = 0$ provides the best bound close to the typical value a_0 , but not far from it, indicating that very rare values of a are produced by the original model using a combination of rare jump types ($s \neq 0$) and rare jump times ($\lambda \neq 0$).

The bound swept out by scanning both s and λ is shown in blue in Fig. 3.2(b). We used 201 equally spaced s values on the interval $[-5, 5]$, and 51 equally spaced λ values on $[0, 50]$. This bound lies close to the exact answer, even far into the tails of the rate function. For comparison we show the weakened linear response (WLR) universal current bound of Ref. [55] (gray dashed line); the dotted box in the center of the figure indicates the scale of Fig. 2 of that paper. The WLR bound is

$$J[\text{WLR}] = \frac{\sigma_0}{4c_0^2}(c - c_0)^2, \quad (3.37)$$

where c is a current, c_0 is its typical value (in the original model), and σ_0 is the typical value of the rate of entropy production. c_0 and σ_0 must be determined by running a single trajectory of the original model, and (3.37) then provides a bound on the probability of observing an atypical value of c . The bound is tightest in the case $c \propto \sigma$.

The WLR bound can be derived from Level 2.5 of large deviations [57, 58] using a mean-field ansatz that assumes all currents scale with time in the same way (for both forward and time-reversed versions of the model). By contrast, the (s, λ) -bound results from a microscopic ansatz, (3.7) and (3.9), inserted into the exact result (3.5) for the dynamical partition sum, and does not assume that all currents scale in the same way. Inspection of the tails of the bounds reveals that the microscopic ansatz captures the rare behavior of the model more accurately than does the homogeneous ansatz. Thus we learn that the rare behavior of even this very simple model does not simply resemble a speeded-up or slowed-down version of its typical behavior. The bound (3.37) is a universal statement about the physics that constrain fluctuations, and is not designed to be a means of accurate numerical sampling. Nonetheless, it is meaningful and instructive to compare the bounds produced by different types of ansätze.

For each of the reference models that lie on the bound $J_0[s, \lambda]$ we calculate the correction (3.18) using the procedure described in Section 3.2. For all points we

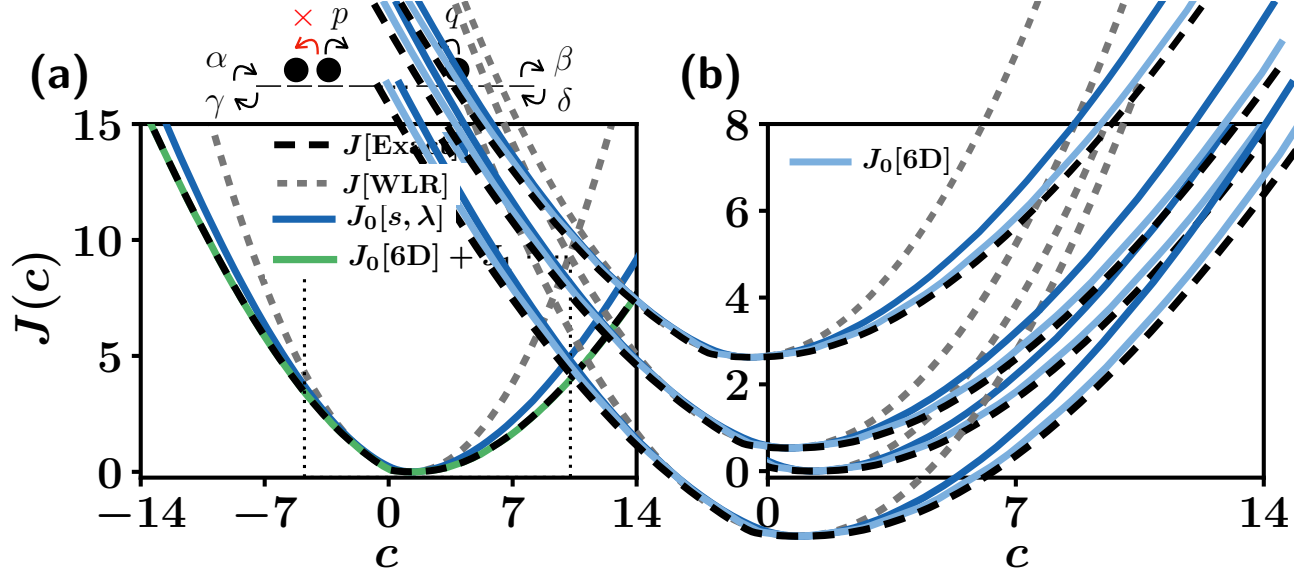


Figure 3.3: Large-deviation rate function $J(c)$ of particle current, c , for the version of the ASEP studied in Ref. [55]; rate constants are given in the text. (a) We show the exact answer (black), the WLR universal current bound [54, 55] (gray), and the bound produced using our default (s, λ) reference-model parameterization (dark blue). (b) With additional physical insight used to refine the reference model it is possible to tighten the bound (compare dark blue and light blue lines). The green line in (a) is the corrected version of the 6D bound. The boxed region in panel (a) indicates the scale of Fig. 3 of Ref. [55] (not the scale of Fig. 3.3(b)). Error bars for both axes are smaller than the thickness of the lines.

obtain convergence of the correction. The result, $J_0(a) + J_1(a)$, is shown as a green line in the inset of Fig. 3.2(b), and matches the exact answer (black), obtained by matrix diagonalization, as it should. We used 10^4 blocks, each of length of $50T_{\text{event}}$, where T_{event} is the time per event for each reference model. The average correction (3.30) and statistical error are obtained from 10 independent data sets. Error bars on the rate function are calculated by combining the error from the correction and the error from the bound according to

$$\text{Err}[\hat{J}(\tilde{a}_0)] = \sqrt{(\text{Err}[\hat{J}_0(\tilde{a}_0)])^2 + (\text{Err}[\hat{J}_1(\tilde{a}_0)])^2}. \quad (3.38)$$

The error in the bound is estimated by running 10 additional trajectories at each point and calculating the standard deviation of $J_0(\tilde{a}_0)$. The standard deviation of \tilde{a}_0 , calculated in the same way, yields error bars for the horizontal axis.

From this example it is clear that VARD is numerically much more efficient than direct simulation (of the original model): accurate calculation of the rate function at values of order 100 indicates accurate calculation of probabilities of order e^{-100T} ,

where T is the elapsed time of the trajectory. We do not know in advance which values of reference-model parameters constitute good choices, for particular values of a , but it is a simple matter to scan parameters and pick the smallest value of J_0 given a . Additional sampling then allows us to determine if we can calculate the correction (3.18), and therefore the exact rate function. We were able to do this here with little additional numerical effort. In this example, the state space of the model is small enough that its dynamics can be solved by matrix diagonalization, and so we possess the exact answer in advance. We made this choice because we wish to benchmark the method. However, our procedure would be identical if we did not know the exact answer ahead of time: define the reference model, pick the best bound, and attempt to calculate the correction term. The results of the latter calculation tell us if we have the exact answer, or, if not, roughly how close we are to obtaining it. If we are not close at all then we need a better reference-model guess. Inspection of the bounds produced by different reference models is also physically instructive, indicating the extent to which certain dynamical mechanisms contribute to the rate function at particular values of the order parameter.

Current in the ASEP

We next sample current in the asymmetric simple exclusion process (ASEP), a model of hard particles that hop between lattice sites [6, 66] (an interesting alternative would be to consider the symmetric simple exclusion process, which has fewer parameters but also shows complex scaling behavior [74]). We consider the version of the model studied in Fig. 3 of [55], shown in Fig. 3.3, with open boundaries and a lattice of $L = 15$ sites. The rate constants are $\alpha = 1.25, \beta = 0.5, \gamma = 0.5, \delta = 1.5, p = 1$, and $q = 0.5$, placing the model in the high-density region of the ASEP phase diagram [75, 76]. The dynamical observable is $a = c = T^{-1} \sum \alpha_{xy}$, where the sum is taken over all jumps $x \rightarrow y$ of a trajectory, and $\alpha_{xy} = \pm 1$ if the jump $x \rightarrow y$ sees a particle move to the right (upper sign) or left (lower sign).

In Fig. 3.3(a) we show the bound swept out by our default (s, λ) reference-model parameterization (dark blue), which provides a meaningful numerical bound on the exact rate function (black) even far into the tails. We ran trajectories for $K = 5 \times 10^5$ events, roughly equivalent to a time $T = 10^5$ in the unbiased model. We scanned 81 equally spaced s values on the interval $[-2, 2]$, and 41 equally spaced λ values on $[0, 10]$. Also shown is the WLR universal current bound [54, 55] (gray). The WLR bound describes accurately the moderately rare behavior of the model, but not the very rare behavior, which is quantified by the tails of the rate function. Comparison of

bounds indicates, as in the previous subsection, that very rare currents are generated by trajectories that do not resemble speeded-up or slowed-down versions of the forward- or backward-running typical dynamics: the configurations visited in the tails of the rate function are different to those visited near the center.

While the (s, λ) -bound is already meaningful, it is possible to produce tighter numerical bounds by guessing additional ways in which the very rare high- or low-current behavior might be achieved. Inspection of the way in which s couples to the rate constants (here any rate involving a hop to the right is multiplied by e^{-s} and any rate involving a hop to the left is multiplied by e^s) reveals that varying s moves the reference model around the ASEP phase diagram [75, 76]. The original model sits in the high-density region of phase space, but the reference model need not. Inspection of the phase diagram indicates that the end rates $\alpha, \beta, \gamma, \delta$, separate from the bulk rates p and q , play a key role in determining the ASEP's typical behavior: if particles are fed in relatively quickly or slowly then we reside in the high- or low-density region of phase space, respectively, and if input- and output rates are balanced then we can access the maximum-current region. Returning to (3.8) we introduce a set of parameters β_{xy} that couple to the end rates, such that the rate α in the original model becomes $e^{-u_\alpha} \alpha$ in the reference model (u_α being a parameter), and similarly for the three other end rates. We also include a contribution to β_{xy} that biases trajectories toward or away from creating particle-particle contacts (i.e. particles on adjacent sites), reasoning that controlling such contacts can help control the escape rate of visited configurations, so helping cause or prevent traffic jams. A simple way to do this is to add to β_{xy} a bias $-\mu \Delta_{xy}$, where μ is a parameter and Δ_{xy} is the change in the number of particle-particle contacts when moving from x to y .

With the new bias determined we can generate an improved bound for the ASEP. We split the calculation into two parts and focus separately on the piece of the rate function for values of the observable greater than the mean, $a > a_0$, and less than the mean, $a < a_0$. Since the dynamics in these two different regimes are qualitatively different, generating an effective set of reference models for each requires scanning over different regions of the ansatz parameter space. For $a < a_0$ we scanned s, λ, u_γ and μ . For $a > a_0$ we scanned $s, \lambda, u_\alpha, u_\beta$ and μ , making 6 parameters in total. Combining these calculations produces the 6D bound shown in light blue in Fig. 3.3(b). This bound is tighter than the default (s, λ) -bound. The 6-parameter scan can be carried out with reasonable numerical effort: for a given set of parameters we need only a short single trajectory to compute the averages

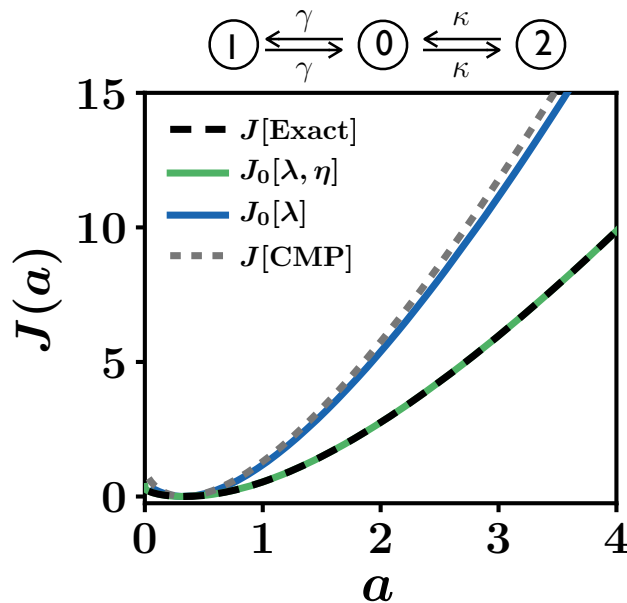


Figure 3.4: Large-deviation rate function $J(a)$ for the number of jumps $1 \rightarrow 0$ per unit time, a , for the 3-state model of Ref. [56]. We compare with the exact answer (black) the bounds produced by reference models in which we control jump times (blue), or jump times and jumps from $0 \rightarrow 1$ (green). Error bars for both axes are smaller than the thickness of the lines. Also shown is the CMP universal activity bound [56], Eq. (3.39) (gray).

required for the bound, and there is no requirement for communication between the calculations. On the left side we scanned 11 equally spaced s values on the interval $[0, 2]$; 21 equally spaced λ values on the interval $[-0.6, 0]$, and 17 more on the interval $[0, 8]$; 29 u_γ values so that γ takes on equally spaced values on the interval $[0.1, 1.5]$; and 31 equally spaced μ values on the interval $[-1, 0.5]$. On the right side we scanned 11 equally spaced s values on the interval $[-2, 0]$; 17 equally spaced λ values on the interval $[0, 8]$; 21 u_α values and 21 u_β values so that α and β each take on values equally spaced on the interval $[0.5, 1.25]$; and 11 equally spaced μ values on the interval $[0, 0.5]$. The lower envelope of the values of (3.17) constitutes the improved bound.

Correcting the 6D bound by calculating the correction J_1 at points along the bound gives the green line shown in Fig. 3.3(a), which agrees with the exact rate function even far into the tails. For this calculation we used 10^4 blocks of length $100T_{\text{event}}$, where T_{event} is the time per event in each reference model. Errors are computed as in Section 3.3.

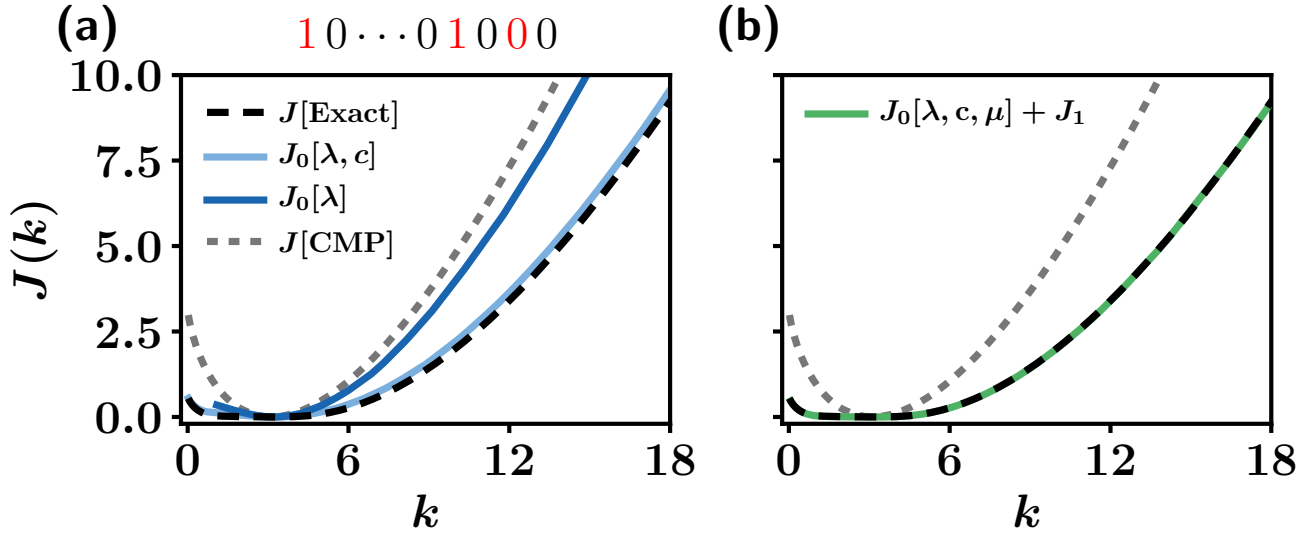


Figure 3.5: Large-deviation rate function $J(k)$ for the number of jumps per unit time, k , for the one-dimensional Fredrickson-Andersen model. (a) We compare with the exact answer (black) the bounds produced by reference models in which we control jump times (dark blue) or jump times and the mean up-spin fraction (light blue). Also shown is the CMP universal activity bound [56], Eq. (3.39) (gray). (b) The sum (green) of the bound (produced using a reference model in which we control jump times, mean up-spin fraction, and pair correlations) and the correction matches the exact answer. Error bars for both axes are smaller than the thickness of the lines.

Activity in a 3-state model

We consider the three-state model of Fig. 3 of Ref. [56], shown in Fig. 3.4. The rate constants are $\gamma = 1$ and $\kappa = 1/2$. Our chosen dynamical observable, a , is the number of jumps from states $1 \rightarrow 0$ per unit time. The parameter s in our default (s, λ) reference-model parameterization (3.8) has no role to play here: s controls the probability of the $1 \rightarrow 0$ process, but once in state 1 there is nowhere to go but state 0. Thus s cannot influence the number of counted events per jump, A/K , and so we set $s = 0$.

At this point we need to apply our physical intuition in order to create a reference-model ansatz able to control A/K . Inspection of the network reveals that controlling the jump destination from state 0 is sufficient for this purpose: if we jump $0 \rightarrow 1$ then we must subsequently jump $1 \rightarrow 0$, whereas if we jump $0 \rightarrow 2$ we will return to 0 without making the counted jump. In Eq. (3.8) we therefore set $\beta_{01} = \eta$ (a parameter) such that the reference-model rate for the process $0 \rightarrow 1$ is $\tilde{W}_{01} = e^{-\eta}\gamma$. We set all other $\beta_{xy} = 0$. Scanning η and λ (our usual jump-time bias) produces

the bound shown in green in Fig. 3.4. Bounds were calculated using 11 equally spaced λ values on the interval $[-0.5, 0]$ and 101 values on the interval $[0, 25]$, and 51 equally spaced η values on the interval $[-5, 5]$. All trajectories were run for $K = 10^7$ events, roughly equivalent to a time of $T = 10^7$ in the unbiased model. Error bars are computed as in Section 3.3.

The (η, λ) -bound is effectively exact, as we can deduce by measuring the fluctuations of q (which here are nonexistent). In this case the model is simple enough that each reference model used to compute the bound enacts the exact rare dynamics of the original model, conditioned on a particular value of a . As a result, the correction term J_1 vanishes, and the bound J_0 is exact. (This exactness is reasonable on account of the fact that the system has relatively few ways of realizing values of A/K and K/T , but it is not obvious in advance that the chosen parameterization would require no additional correction.) Recall that the correction term can be interpreted as a measure of how close the typical dynamics of the reference model is to the desired rare dynamics of the original model; here, typical trajectories of the reference model correspond exactly to trajectories of the original model conditioned on the relevant value of the order parameter.

The chosen observable is a non-decreasing counting variable, not a current, and so the universal bound of Refs. [54, 55] does not apply. One that does apply is the Conway-Maxwell-Poisson (CMP) bound of Ref. [56],

$$J[\text{CMP}] = \frac{k_0}{a_0} \left(a \ln \frac{a}{a_0} + a_0 - a \right), \quad (3.39)$$

where a is the dynamical observable, a_0 is its typical value (in the original model), and k_0 is the typical dynamical activity (the total number of events per unit time) of the original model (note that there is an a missing in front of the logarithm in Eq. (17) of [56]).

The CMP bound is shown in gray in Fig. 3.4. Similar to the universal current bound, the CMP bound is derived from Level 2.5 of large deviations using an ansatz that assumes the rare behavior of the system to be a speeded-up or slowed-down version of its typical behavior. It therefore has similar properties to our λ -bound, shown in blue in Fig. 3.4 (the λ bound is constructed from the pieces of the (η, λ) -bound with $\eta = 0$). Comparison of this bound and the (λ, η) -bound shows the extent to which the very rare behavior of this model is dominated by trajectories comprising rare jump times *and* an atypical propensity to jump left from state 0. Analogous to its current counterpart, the CMP bound is a general statement about the physics

controlling the fluctuations of counting variables, and is not intended to be a means of numerical sampling. Nonetheless, comparison of its properties with bounds obtained by the microscopic ansatz used here is instructive, and addresses the point raised in Ref. [56]: “It would be interesting to find alternative yet simple variational ansatzes that can capture [the] strong fluctuation behavior [of the 3-state model]”.

Activity in the FA model

We consider the one-dimensional Fredrickson-Andersen (FA) model with periodic boundary conditions [67]. This is a lattice model with simple thermodynamics and with dynamical rules that give rise to slow relaxation and complex spatiotemporal behavior [77]. On each site of a lattice (here of length $L = 15$) lives a spin, which can be up or down. Up-spins (resp. down-spins) can flip down (resp. up) with rate $1 - c$ (resp. c) if at least one of their neighboring spins is up; if not, then they cannot flip (the rate c here should not be confused with the symbol for current in previous sections). In Fig. 3.5(a), top, we show an example FA model configuration, with periodic boundary conditions; the spins in red cannot flip. Our chosen dynamical observable, $a = k = T^{-1} \sum \alpha_{xy}$, is the number of jumps per unit time, where $\alpha_{xy} = 1$ for all jumps $x \rightarrow y$. The large-deviation properties of k have been studied in detail, and give rise, in certain limits, to singular behavior in the SCGF that is Legendre dual to $J(k)$ [10, 11].

In Fig. 3.5(a) we show the CMP universal activity bound [56] on $J(k)$ and the bound produced by our reference-model λ -scan. These are of similar character, because they assume that the rare behavior of the model is a speeded-up or slowed-down version of its typical behavior. All trajectories were run for $K = 3 \times 10^5$ events, roughly equivalent to a time of $T = 10^5$ in the unbiased model. We used 61 equally spaced λ values on the interval $[-0.6, 0]$, and 61 more on the interval $[0, 12]$. To produce a tighter bound we need to assume that the configurations visited by rare trajectories are different to those visited by typical ones (the CMP bound assumes that they are the same). The parameter s in our default (s, λ) reference-model parameterization (3.8) again has no role to play, because biasing all jumps equally is equivalent to biasing none. A simple alternative is to choose the bias β_{xy} so that the reference model can generate a larger or smaller number of up-spins than is typical in the original model. We choose the parameters β_{xy} so that the parameter c in the original model becomes $e^{-\eta}c$ in the reference model, with η being a parameter. A (λ, η) -scan of the reference model produces the bound $J_0[\lambda, c]$ shown in light blue in Fig. 3.5(a). This bound provides a reasonable approximation of the exact

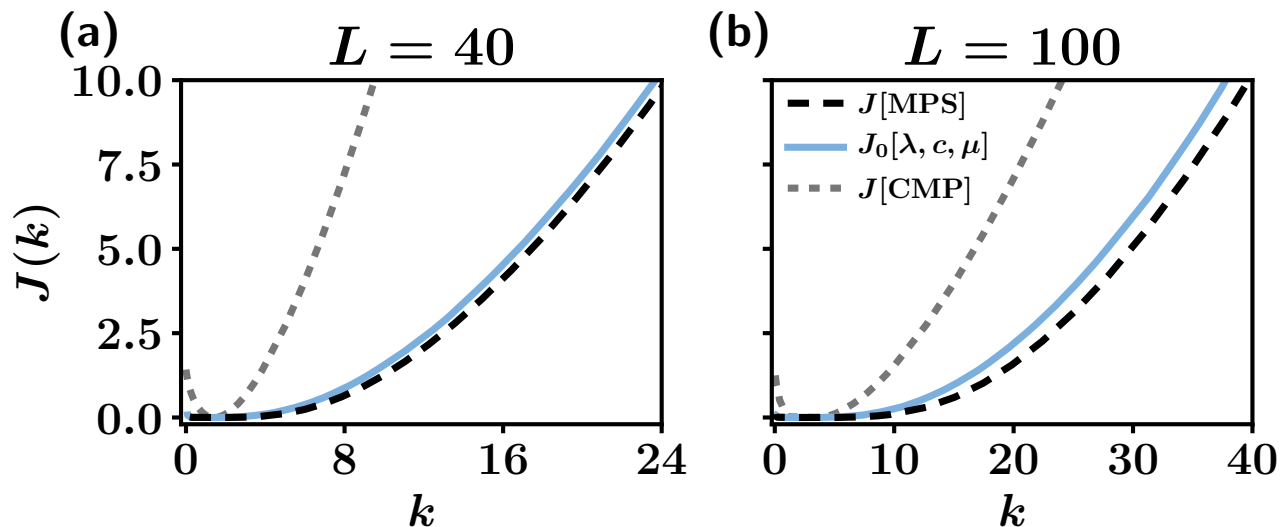


Figure 3.6: Large-deviation rate function $J(k)$ for the number of jumps per unit time, k , for the Fredrickson-Andersen model of Ref. [78] with $c = 0.1$. Lattice sizes are (a) $L = 40$ sites and (b) $L = 100$ sites. We compare the matrix product state (MPS) calculation of Ref. [78] (black) with the three-parameter VARD bound of Fig. 3.5 (blue). Also shown is the CMP universal activity bound [56], Eq. (3.39) (gray).

answer over the whole range of k , indicating that much of the physics of rare activity fluctuations of the FA model can be accounted for by considering the typical behavior of versions of the model with different values of the parameter c . Here we chose η so that c takes on 100 equally spaced values on the interval $[0.02, 2]$.

It is possible to tighten this bound by reasoning that there must exist spatial correlations between up-spins if we condition trajectories upon activity per unit time k . For instance, given an up-spin fraction of exactly $1/2$, the escape rate (the sum of rates leading out of a given state, a quantity relevant to the number of jumps per unit time) is maximized by having pairs of up-spins separated by pairs of down-spins, and minimized by having up-spins and down-spins alternate. We induce these types of spatial correlations using the same μ -bias used for the ASEP in Section 3.3, favoring more or fewer contacts between up spins. Scanning c, η , and μ produces a bound slightly tighter than $J_0[\lambda, \eta]$ (not shown). We used 41 equally spaced μ values on the interval $[-1, 1]$. From this bound we compute the correction J_1 , and the sum of the bound and correction matches the exact answer: see Fig. 3.5(b). We computed the correction by splitting the calculation into two pieces, one on either side of the mean value $a = a_0$. For $a < a_0$ we used 10^4 blocks of length $50T_{\text{event}}$,

where T_{event} is the average time per event in each reference model. For $a > a_0$ we used 10^5 blocks of length $600T_{\text{event}}$. The different block lengths generated by the convergence procedure (see Section 3.2) for $a < a_0$ and $a > a_0$ signal that the correlations present in the dynamics are qualitatively different in each of these regimes. Understanding the nature of these correlations is of physical interest [11, 77]. Errors are calculated as in Section 3.3.

Toward large-scale calculations

In this paper we have demonstrated proof-of-principle of VARD using network systems or lattice models whose state space is small enough that their rate functions can be obtained by matrix diagonalization, so providing a benchmark for the method. VARD can also be applied to systems too large for matrix diagonalization to be feasible, in order to produce bounds or (if the ansatz is good enough and convergence of the correction is obtained) exact rate functions. An active line of research is to study large versions of certain lattice models in order to determine how their large-deviation properties change with system size [11, 36, 78]. In these regimes, specialized techniques are necessary. For instance, in Ref. [36], a cloning procedure combined with feedback control was used to calculate large-deviation functions for an FA model of $L = 36$ sites. In Ref. [78], a matrix product state (MPS) calculation was used to compute large-deviation functions for an FA model of sizes of order $L = 100$ sites (these results show some differences with the results of Ref. [36], indicating that this is a technically challenging regime). Note that the FA model of Ref. [78] has open boundaries and slightly different facilitation rules than used in the previous section: spins facilitated by two spins flip at twice the rate of spins facilitated by one spin.

In Fig. 3.6 we compare the MPS calculation of Ref. [78] with the three-parameter VARD bound used in Fig. 3.5 for two lattice sizes that are considered large by current standards (the parameter $c = 0.1$). In both cases the VARD bound is descriptive, capturing the main features and the trends with k of the MPS result. The bound is less tight for the larger system size, suggesting that more terms in the ansatz are required as the system becomes larger. However, the bound quality, even using an ansatz containing only 3 parameters, remains reasonable. As for the ASEP, the natural next step is to include additional parameters in the ansatz in order to tighten the bound and calculate the correction (compare dark blue and light blue lines in Fig. 3.3(b)). A natural way to develop improved bounds is to use Monte Carlo learning procedures in order to optimize reference models containing a potentially

large number of parameters [79].

3.4 Conclusions

We have described how direct simulation of a variational ansatz for rare dynamics (VARD) can be used to compute bounds for large-deviation rate functions in continuous-time Markov chains ⁷. This approach requires only direct simulation of versions of the original model with modified rates, and so is technically simple and easy to implement. It is also physically instructive, in the sense that the quality of the bounds produced by different physical ansätze reveal the extent to which different types of dynamical processes contribute to the rare behavior of the model of interest.

If the ansatz is chosen well then bounds can be corrected to produce the exact rate function, arbitrarily far into its tails; in the literature it is often assumed or stated that such precision is not accessible via direct reweighting of trajectories, and requires the use of specialized numerical techniques such as cloning or path sampling. For the models studied in Figs. 3.2–3.5, two network models and two lattice models taken from the literature, it is possible to calculate the exact rate function using only simple and approximate guesses about the nature of the rare dynamics. Although this rare behavior can be complex, we are rarely working in the dark: the model itself can exhibit different behavior in different parameter regions, and often its rare behavior at one point in parameter space is similar to its typical behavior at another point in parameter space. For example, we have studied the ASEP in its high-density region, where (typically) the lattice is crowded and particles move slowly. The ansatz we used to calculate its current rate function is equivalent to guessing that the rare, high-current behavior in the high-density region is similar to the typical behavior in the maximum-current region, where particles move quickly and possess spatial anticorrelations. Similarly, the FA model is complex, but the likelihood of its rare behavior at one value of the parameter c can be well approximated by looking at the typical behavior of models at different values of c . We have also shown that bounds that are descriptive in small systems remain so in systems too large to solve by matrix diagonalization; we will discuss this regime further in forthcoming work.

VARD is similar to classical umbrella sampling [64, 65] in the sense that the rate function $\tilde{J}(a)$ of the reference model can be regarded as a nonequilibrium umbrella potential, concentrating sampling at a desired point: see Fig. 3.1. It is different, however, in that VARD does not require overlapping sampling windows – reference

⁷The method works for Markov chains in discrete time, upon replacing the distributions (3.4) and (3.9) by $\delta(\Delta t - 1)$; see earlier versions of the method [41–43].

models are used independently – and we compute an absolute rate-function value $J(a)$, as opposed to a free-energy difference. This latter distinction results from the fact that the path weight appearing in (3.5) is known exactly, and at the sampling point \tilde{a}_0 we know that the rate function of the reference model vanishes; by contrast, in the equilibrium case we know the probability of visiting a certain state only up to a normalization constant, and we do not know the absolute free energy of the reference model (unless it is particularly simple [80]).

VARD provides insight into the approaches used to produce universal rate-function bounds from Level 2.5 of large deviations, via homogeneous ansätze [54–56], by showing how relaxing such assumptions leads to the tightening of bounds in different sectors of parameter space. It is also complementary to numerical large-deviation methods that use path-sampling, cloning, or adaptive methods to calculate the SCGF ⁸ that is Legendre dual to $J(a)$ [11, 28, 32–37]. Sometimes path sampling or cloning are used in isolation, and sometimes they are combined with a modified dynamics. VARD lies at the other extreme of the methods spectrum in the sense that it uses *only* a modified dynamics. The bounds that result provide a natural starting point for those specialized methods, because the set of reference models that live on the bounds already resemble the rare dynamics of interest. Indeed, direct sampling of those reference models is, in the cases described in Figs. 3.2–3.5, sufficient to recover the statistics (the constituent configurations and jump times) required to compute $J(a)$ exactly.

There are several possible variants of the present method. The λ -scan accesses roughly the same information as the universal bounds of Refs. [54–56], and one possible numerical simplification would be to eliminate the λ -scan in favor of the universal bounds (3.37) or (3.39). We have also simply scanned parameters in order to identify the best bounds associated with a given ansatz, but as the complexity of an ansatz grows it is be natural to replace the scan with an evolutionary Monte Carlo procedure [79]. For instance, consider a set of reference models having N parameters, and construct an initial (s, λ) -bound. Take models at various points on this bound, and define a window Δa for the observable. For each model, perturb the N parameters, generate a short trajectory, and calculate Eq. (3.17). If this value is less than the current bound (and a lies within the designated window) accept the new reference model; otherwise, retain the original.

⁸One advantage of bypassing the SCGF and calculating the rate function directly, as we do here, is the ability to reconstruct rate functions that are not strictly convex [28, 41, 81].

3.5 Acknowledgments

We thank Hugo Touchette, Tom Ouldridge, and Juan Garrahan for discussions and comments on the manuscript, and thank Juan Garrahan, Todd Gingrich, and Mari Carmen Bañuls for providing data from Refs. [56], [16], and [78], respectively. This work was performed as part of a user project at the Molecular Foundry, Lawrence Berkeley National Laboratory, supported by the Office of Science, Office of Basic Energy Sciences, of the U.S. Department of Energy under Contract No. DE-AC02-05CH11231. DJ acknowledges support from the Department of Energy Computational Science Graduate Fellowship.

References

1. Gillespie, D. T. Stochastic simulation of Chemical kinetics. *Annu. Rev. Phys. Chem.* **58**, 35–55 (2007).
2. McGrath, T., Jones, N. S., ten Wolde, P. R. & Ouldridge, T. E. BioChemical machines for the interconversion of mutual information and work. *Physical Review Letters* **118**, 028101 (2017).
3. Seifert, U. Stochastic thermodynamics, fluctuation theorems and molecular machines. *Reports on progress in Physics* **75**, 126001 (2012).
4. Brown, A. I. & Sivak, D. A. Allocating dissipation across a molecular machine cycle to maximize flux. *Proceedings of the National Academy of Sciences* **114**, 11057–11062 (2017).
5. Visco, P., Puglisi, A., Barrat, A., Trizac, E. & van Wijland, F. Fluctuations of power injection in randomly driven granular gases. *Journal of statistical Physics* **125**, 533–568 (2006).
6. Chou, T., Mallick, K. & Zia, R. Non-equilibrium statistical mechanics: from a paradigmatic model to biological transport. *Reports on progress in Physics* **74**, 116601 (2011).
7. Vaikuntanathan, S., Gingrich, T. R. & Geissler, P. L. Dynamic phase transitions in simple driven kinetic networks. *Physical Review E* **89**, 062108 (2014).
8. Harris, R. J. Fluctuations in interacting particle systems with memory. *Journal of Statistical Mechanics: Theory and Experiment* **2015**, P07021 (2015).
9. Berthier, L. Nonequilibrium glassy dynamics of self-propelled hard disks. *Physical Review Letters* **112**, 220602 (2014).
10. Garrahan, J. P. *et al.* Dynamical first-order phase transition in kinetically constrained models of glasses. *Physical Review Letters* **98**, 195702 (2007).
11. Garrahan, J. P. *et al.* First-order dynamical phase transition in models of glasses: an approach based on ensembles of histories. *Journal of Physics A: Mathematical and Theoretical* **42**, 075007 (2009).

12. Ritort, F. Nonequilibrium fluctuations in small systems: From Physics to biology. *Advances in Chemical Physics* **137**, 31 (2008).
13. Seifert, U. Entropy production along a stochastic trajectory and an integral fluctuation theorem. *Physical Review Letters* **95**, 040602 (2005).
14. Speck, T., Engel, A. & Seifert, U. The large deviation function for entropy production: the optimal trajectory and the role of fluctuations. *Journal of Statistical Mechanics: Theory and Experiment* **2012**, P12001 (2012).
15. Lecomte, V., Imparato, A. & Wijland, F. v. Current fluctuations in systems with diffusive dynamics, in and out of equilibrium. *Progress of Theoretical Physics Supplement* **184**, 276–289 (2010).
16. Gingrich, T. R. & Horowitz, J. M. Fundamental bounds on first passage time fluctuations for currents. *Physical Review Letters* **119**, 170601 (2017).
17. Fodor, É. *et al.* Activity-driven fluctuations in living cells. *EPL (EuroPhysics Letters)* **110**, 48005 (2015).
18. Chandler, D. Introduction to modern statistical mechanics. *Introduction to Modern Statistical Mechanics, by David Chandler, pp. 288. Foreword by David Chandler. Oxford University Press, Sep 1987. ISBN-10: 0195042778. ISBN-13: 9780195042771, 288* (1987).
19. Binney, J. J., Dowrick, N., Fisher, A. & Newman, M. *The theory of critical phenomena: an introduction to the renormalization group* (Oxford University Press, Inc., 1992).
20. Gallavotti, G. & Cohen, E. G. D. Dynamical ensembles in nonequilibrium statistical mechanics. *Physical Review Letters* **74**, 2694 (1995).
21. Maes, C. The fluctuation theorem as a Gibbs property. *Journal of Statistical Physics* **95**, 367–392 (1999).
22. Jarzynski, C. Nonequilibrium equality for free energy differences. *Physical Review Letters* **78**, 2690 (1997).
23. Kurchan, J. Fluctuation theorem for stochastic dynamics. *Journal of Physics A: Mathematical and General* **31**, 3719 (1998).
24. Lebowitz, J. L. & Spohn, H. A Gallavotti–Cohen-type symmetry in the large deviation functional for stochastic dynamics. *Journal of Statistical Physics* **95**, 333–365 (1999).
25. Crooks, G. E. Entropy production fluctuation theorem and the nonequilibrium work relation for free energy differences. *Physical Review E* **60**, 2721 (1999).
26. Harris, R. J. & Schütz, G. M. Fluctuation theorems for stochastic dynamics. *Journal of Statistical Mechanics: Theory and Experiment* **2007**, P07020 (2007).
27. Den Hollander, F. *Large Deviations* (American Mathematical Soc., 2008).

28. Touchette, H. The large deviation approach to statistical mechanics. *Physics Reports* **478**, 1–69 (2009).
29. Spiliopoulos, K. Large deviations and importance sampling for systems of slow-fast motion. *Applied Mathematics & Optimization* **67**, 123–161 (2013).
30. Bouchet, F., Grafke, T., Tangarife, T. & Vanden-Eijnden, E. Large deviations in fast–slow systems. *Journal of Statistical Physics* **162**, 793–812 (2016).
31. Whitlam, S. Large deviations in the presence of cooperativity and slow dynamics. *Physical Review E* **97**, 062109 (2018).
32. Giardinà, C., Kurchan, J. & Peliti, L. Direct evaluation of large-deviation functions. *Physical Review Letters* **96**, 120603 (2006).
33. Chetrite, R. & Touchette, H. Variational and optimal control representations of conditioned and driven processes. *Journal of Statistical Mechanics: Theory and Experiment* **2015**, P12001 (2015).
34. Jack, R. L. & Sollich, P. Effective interactions and large deviations in stochastic processes. *The European Physical Journal Special Topics* **224**, 2351–2367 (2015).
35. Ray, U., Chan, G. K.-L. & Limmer, D. T. Exact fluctuations of nonequilibrium steady states from approximate auxiliary dynamics. *Physical Review Letters* **120**, 210602 (2018).
36. Nemoto, T., Jack, R. L. & Lecomte, V. Finite-size scaling of a first-order dynamical phase transition: Adaptive population dynamics and an effective model. *Physical Review Letters* **118**, 115702 (2017).
37. Ferré, G. & Touchette, H. Adaptive sampling of large deviations. *arXiv preprint arXiv:1803.11117* (2018).
38. Chetrite, R. & Touchette, H. Nonequilibrium microcanonical and canonical ensembles and their equivalence. *Physical Review Letters* **111**, 120601 (2013).
39. Lecomte, V. & Tailleur, J. A numerical approach to large deviations in continuous time. *Journal of Statistical Mechanics: Theory and Experiment* **2007**, P03004 (2007).
40. Kundu, A., Sabhapandit, S. & Dhar, A. Application of importance sampling to the computation of large deviations in nonequilibrium processes. *Physical Review E* **83**, 031119 (2011).
41. Klymko, K., Geissler, P. L., Garrahan, J. P. & Whitlam, S. Rare behavior of growth processes via umbrella sampling of trajectories. *Phys. Rev. E* **97**, 032123. <https://link.aps.org/doi/10.1103/PhysRevE.97.032123> (3 Mar. 2018).
42. Whitlam, S. Sampling rare fluctuations of discrete-time Markov chains. *Physical Review E* **97**, 032122 (2018).

43. Whitelam, S. Multi-point nonequilibrium umbrella sampling and associated fluctuation relations. *Journal of Statistical Mechanics: Theory and Experiment* **2018**, 063211. <http://stacks.iop.org/1742-5468/2018/i=6/a=063211> (2018).
44. Bucklew, J. A., Ney, P. & Sadowsky, J. S. Monte Carlo simulation and large deviations theory for uniformly recurrent Markov chains. *Journal of Applied Probability* **27**, 44–59 (1990).
45. Glynn, P. W. & Iglehart, D. L. Importance sampling for stochastic simulations. *Management Science* **35**, 1367–1392 (1989).
46. Sadowsky, J. S. & Bucklew, J. A. On large deviations theory and asymptotically efficient Monte Carlo estimation. *IEEE transactions on Information Theory* **36**, 579–588 (1990).
47. Glasserman, P., Wang, Y., *et al.* Counterexamples in importance sampling for large deviations probabilities. *The Annals of Applied Probability* **7**, 731–746 (1997).
48. Warren, P. B. & Allen, R. J. Trajectory reweighting for non-equilibrium steady states. *Molecular Physics* **116**, 3104–3113 (2018).
49. Bucklew, J. A. *Large deviation techniques in decision, simulation, and estimation* (Wiley New York, 1990).
50. Asmussen, S. & Glynn, P. W. *Stochastic simulation: algorithms and analysis* (Springer Science & Business Media, 2007).
51. Juneja, S. & Shahabuddin, P. Rare-event simulation techniques: an introduction and recent advances. *Handbooks in operations research and management science* **13**, 291–350 (2006).
52. Bucklew, J. *Introduction to rare event simulation* (Springer Science & Business Media, 2013).
53. Varadhan, S. S. *Large deviations in Proceedings of the International Congress of Mathematicians 2010 (ICM 2010) (In 4 Volumes) Vol. I: Plenary Lectures and Ceremonies Vols. II–IV: Invited Lectures* (2010), 622–639.
54. Pietzonka, P., Barato, A. C. & Seifert, U. Universal bounds on current fluctuations. *Physical Review E* **93**, 052145 (2016).
55. Gingrich, T. R., Horowitz, J. M., Perunov, N. & England, J. L. Dissipation bounds all steady-state current fluctuations. *Physical Review Letters* **116**, 120601 (2016).
56. Garrahan, J. P. Simple bounds on fluctuations and uncertainty relations for first-passage times of counting observables. *Physical Review E* **95**, 032134 (2017).

57. Maes, C. & Netočný, K. Canonical structure of dynamical fluctuations in mesoscopic nonequilibrium steady states. *EPL (EuroPhysics Letters)* **82**, 30003 (2008).
58. Bertini, L., Faggionato, A., Gabrielli, D., *et al.* Large deviations of the empirical flow for continuous time Markov chains in *Annales de l'Institut Henri Poincaré, Probabilités et Statistiques* **51** (2015), 867–900.
59. Tsobgni Nyawo, P. & Touchette, H. Large deviations of the current for driven periodic diffusions. *Phys. Rev. E* **94**, 032101. <https://link.aps.org/doi/10.1103/PhysRevE.94.032101> (3 Sept. 2016).
60. Jack, R. L. & Sollich, P. Large deviations of the dynamical activity in the East model: Analysing structure in biased trajectories. *Journal of Physics A: Mathematical and Theoretical* **47**, 015003 (2013).
61. Ray, U., Chan, G. K. & Limmer, D. T. Importance sampling large deviations in nonequilibrium steady states: Part 1. *arXiv preprint arXiv:1708.00459* (2017).
62. Rohwer, C. M., Angeletti, F. & Touchette, H. Convergence of large-deviation estimators. *Physical Review E* **92**, 052104 (2015).
63. Jacobson, D. & Whitelam, S. *vard_correction* https://github.com/drdrrjacobs/ward_correction.git. 2019.
64. Torrie, G. & Valleau, J. Nonphysical sampling distributions in Monte Carlo free-energy estimation: umbrella sampling. *Journal of Computational Physics* **23**, 187–199 (1977).
65. Ten Wolde, P. R. & Frenkel, D. Computer simulation study of gas–liquid nucleation in a Lennard-Jones system. *The Journal of Chemical Physics* **109**, 9901 (1998).
66. Derrida, B. An exactly soluble non-equilibrium system: the asymmetric simple exclusion process. *Physics Reports* **301**, 65–83 (1998).
67. Fredrickson, G. H. & Andersen, H. C. Kinetic Ising model of the glass transition. *Physical Review Letters* **53**, 1244 (1984).
68. Binder, K. in *Monte Carlo Methods in Statistical Physics* 1–45 (Springer, 1986).
69. Gillespie, D. T. Exact stochastic simulation of coupled Chemical reactions. *The journal of physical chemistry* **81**, 2340–2361 (1977).
70. Dinwoodie, I. H. & Zabell, S. L. Large Deviations for Exchangeable Random Vectors. *The Annals of Probability* **20**, 1147–1166 (1992).
71. Ellis, R. S. *Large deviations and statistical mechanics* (Springer, New York, 1985).
72. Duffy, K. & Metcalfe, A. P. The large deviations of estimating rate functions. *Journal of applied probability* **42**, 267–274 (2005).

73. Budini, A. A., Turner, R. M. & Garrahan, J. P. Fluctuating observation time ensembles in the thermodynamics of trajectories. *Journal of Statistical Mechanics: Theory and Experiment* **2014**, P03012 (2014).
74. Derrida, B., Lebowitz, J. & Speer, E. Large deviation of the density profile in the steady state of the open symmetric simple exclusion process. *Journal of statistical physics* **107**, 599–634 (2002).
75. Kolomeisky, A. B., Schütz, G. M., Kolomeisky, E. B. & Straley, J. P. Phase diagram of one-dimensional driven lattice gases with open boundaries. *Journal of Physics A: Mathematical and General* **31**, 6911 (1998).
76. Blythe, R., Evans, M., Colaiori, F. & Essler, F. Exact solution of a partially asymmetric exclusion model using a deformed oscillator algebra. *Journal of Physics A: Mathematical and General* **33**, 2313 (2000).
77. Garrahan, J. P. & Chandler, D. Geometrical explanation and scaling of dynamical heterogeneities in glass forming systems. *Physical Review Letters* **89**, 035704 (2002).
78. Bañuls, M. C. & Garrahan, J. P. Using matrix product states to study the dynamical large deviations of kinetically constrained models. *arXiv preprint arXiv:1903.01570* (2019).
79. Whitelam, S., Jacobson, D. & Tamblyn, I. Evolutionary reinforcement learning of dynamical large deviations. *arXiv preprint arXiv:1909.00835* (2019).
80. Frenkel, D. & Ladd, A. J. New Monte Carlo method to compute the free energy of arbitrary solids. Application to the fcc and hcp phases of hard spheres. *The Journal of Chemical Physics* **81**, 3188–3193 (1984).
81. Nickelsen, D. & Touchette, H. Anomalous scaling of dynamical large deviations. *arXiv preprint arXiv:1803.05708* (2018).

Chapter 4

VARIED PHENOMENOLOGY OF MODELS DISPLAYING DYNAMICAL LARGE-DEVIATION SINGULARITIES

Whitelam, S. & Jacobson, D. Varied Phenomenology of Models Displaying Dynamical Large-Deviation Singularities. *Physical Review E* **103**, 032152. <https://link.aps.org/doi/10.1103/PhysRevE.103.032152> (Mar. 29, 2021)

Chapter Abstract

Singularities of dynamical large-deviation functions are often interpreted as the signal of a dynamical phase transition and the coexistence of distinct dynamical phases, by analogy with the correspondence between singularities of free energies and equilibrium phase behavior. Here we study models of driven random walkers on a lattice. These models display large-deviation singularities in the limit of large lattice size, but the extent to which each model's phenomenology resembles a phase transition depends on the details of the driving. We also compare the behavior of ergodic and non-ergodic models that present large-deviation singularities. We argue that dynamical large-deviation singularities indicate the divergence of a model timescale, but not necessarily one associated with cooperative behavior or the existence of distinct phases.

4.1 Introduction

Phase transitions are collective phenomena that occur in the limit of large system size and whose presence can be detected in finite systems [1–3]. Phase transitions cause singularities in thermodynamic potentials and dynamical large-deviation functions, which quantify the logarithmic probability of observing particular values of extensive order parameters [4–7]. An important example of this singularity-phase coexistence correspondence in equilibrium is the 2D Ising model below its critical temperature [1–3, 8]. In dynamical models, singularities (kinks) of large-deviation functions develop in certain limits, and can signal the emergence of a dynamical phase transition and the coexistence of distinct dynamical phases [9–22].

However, large-deviation singularities do not necessarily indicate the existence of cooperative phenomena or distinct phases. For instance, singular features are seen in the large-deviation functions of finite systems in the reducible limit, when the con-

nections between microstates are severed [23–27]. We show here that singularities can also appear in the limit of large system size of dynamical models, if the model’s basic timescale (mixing time) diverges with system size. Such singularities appear whether or not this divergence results from cooperative behavior or is accompanied by evidence of distinct phases.

We study models of driven random walkers on a lattice, which display dynamical large-deviation singularities in the limit of large system size. If the walker is driven in one direction then we see the emergence of dynamical intermittency within trajectories conditioned to produce particular values of a dynamical order parameter. The switching time of this intermittency grows with system size. If the walker is undriven, the singularity results instead from a divergence of the diffusive mixing time of the model, with no intermittency present in conditioned trajectories (both behaviors have a thermodynamic realization in terms of a lattice polymer). We present an argument to rationalize when to expect random-walk models to exhibit intermittency of their conditioned trajectory ensembles, and show that this argument correctly predicts the mixed intermittent/non-intermittent character of the conditioned trajectory ensemble of a random walker whose driving varies with position. We also comment on the relationship between ergodic and non-ergodic dynamical systems that exhibit large-deviation singularities.

In Section 4.2 and Section 4.3 we consider two random-walk models that display large-deviation singularities, but whose conditioned trajectory ensembles are of different character. In Section 4.4 we present a simple argument to rationalize when such models display intermittency of their conditioned trajectories. In Section 4.5 we compare the behavior of ergodic and non-ergodic dynamical models that present large-deviation singularities. We conclude in Section 4.6, arguing that dynamical large-deviation singularities indicate the divergence of a model timescale, but not necessarily one associated with cooperative behavior or the existence of distinct phases.

4.2 Driven random walker

We start with a model similar to one studied in Ref. [13], a driven random walker on a closed (non-periodic) lattice of L sites. We choose L to be odd, and work in discrete time ¹. Let the instantaneous position of the walker be $x \in \{-(L-1)/2, \dots, (L-1)/2\}$. At each time t the walker moves right ($x \rightarrow x+1$) with probability $p(x)$, or

¹We have carried out analogous calculations in continuous time, and draw the same conclusions.

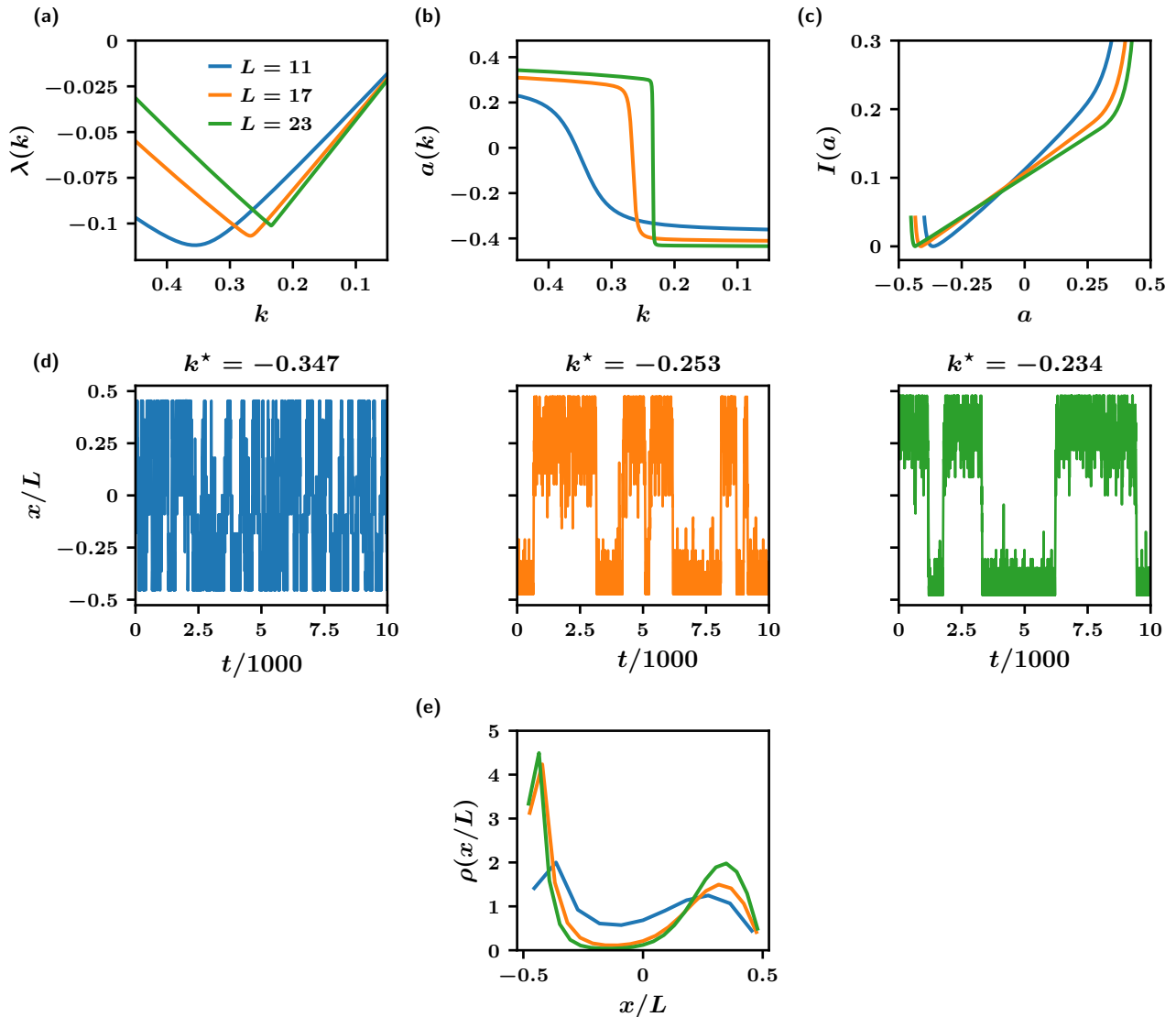


Figure 4.1: (a–c) Large-deviation functions for the time-averaged position a of a driven discrete random walker on a closed lattice of L sites. (d) Walker trajectories showing the instantaneous position x/L under the biased dynamics corresponding to the point $k = k^*$ of greatest curvature of $\lambda(k)$. These trajectories show intermittency, with the walker switching between two locations on either side of the lattice. The timescale for residence in the distinct lattice locations increases with increasing L . (e) Histograms of the instantaneous position x/L for the trajectories in (d).

left with probability $1 - p(x)$. In this section we set $p(x) = 1/4$, and so the walker's typical location is near the left-hand side of the lattice, $x = -(L - 1)/2$. If the walker sits at either edge of the lattice then it moves away from the edge with probability 1 (so $p(-(L - 1)/2) = 1$ and $p((L - 1)/2) = 0$), analogous to reflecting boundaries in the continuum limit.

The master equation associated with this dynamics is

$$P_x(t + 1) = \sum_{x'} W_{x'x} P_{x'}(t), \quad (4.1)$$

where $P_x(t)$ is the probability that the walker resides at lattice site x at time t , and the generator $W_{x'x} = p(x')\delta_{x,x'+1} + (1 - p(x'))\delta_{x,x'-1}$ is the probability of the transition $x' \rightarrow x$.

We take the time-averaged position a of the walker as our dynamical observable. This quantity is

$$a(\omega) = (TL)^{-1} \sum_{t=1}^T x_t^\omega, \quad (4.2)$$

where x_t^ω is the position of the walker at time $t = 1, \dots, T$ within a trajectory ω . We have normalized $a(\omega)$ by the size of the lattice, L . The typical value of a , which we call a_0 , corresponds to the value of (4.2) in the limit of large T . Because the walker prefers to sit near the left-hand side of the lattice, $a_0 \approx -1/2$.

To calculate the probability distribution $\rho_T(A = aT)$ of the walker's time-averaged position, we appeal to the tools of large-deviation theory. The probability distribution adopts in the long-time limit the large-deviation form

$$\rho_T(A) \approx e^{-TI(a)}, \quad (4.3)$$

where $I(a)$ is the rate function (on speed T) [4, 5]. $I(a)$ quantifies the probability with which the walker achieves a specific, and potentially rare, time-averaged position. When $I(a)$ is convex, as it is for ergodic Markov chains, it can be recovered from its Legendre transform, the scaled cumulant-generating function (SCGF) [5],

$$\lambda(k) = a(k)k - I(a(k)). \quad (4.4)$$

Here k is a conjugate field, and $a(k) = \lambda'(k)$ is the value of a associated with a particular value of k . If the lattice is not too large then the SCGF can be calculated by finding directly the largest eigenvalue of the tilted generator, $W_{x'x}^k = e^{kx} W_{x'x}$. The rate function can then be obtained by inverting (4.4). We use this standard method to calculate $\lambda(k)$, $a(k)$, and $I(a)$.

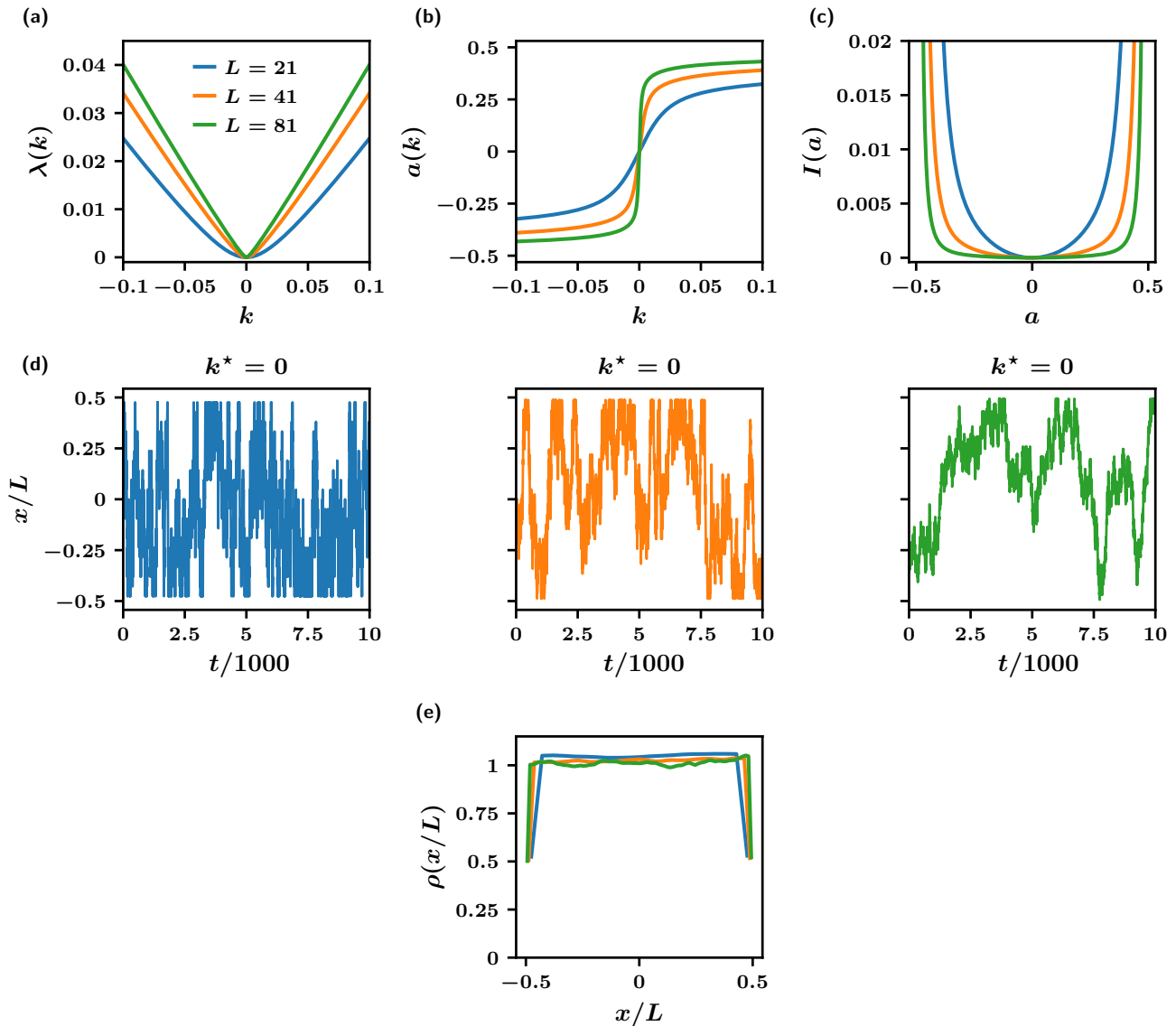


Figure 4.2: Analog of Fig. 4.1, now for an undriven walker. (a–c) As for the driven walker, large-deviation functions show increasingly sharp behavior as L increases. (d) Trajectories showing the instantaneous position x/L of the walker at the point of greatest curvature of $\lambda(k)$, $k^* = 0$. These trajectories do not exhibit intermittency. (e) As a result, histograms of the instantaneous position x/L for the trajectories in (d) are unimodal.

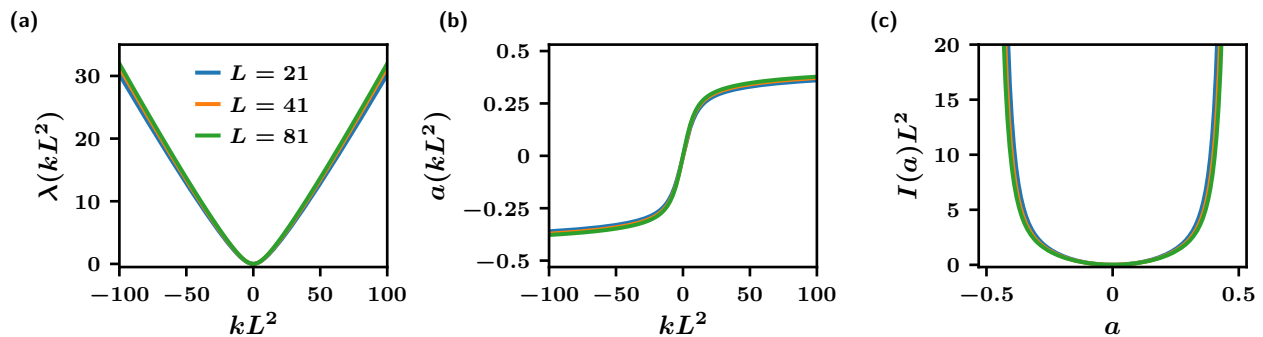


Figure 4.3: (a–c) The large-deviation functions of Fig. 4.2 (a–c), rescaled by L^2 to account for the timescale associated with diffusion. The resulting collapse indicates that these systems behave similarly when viewed on the natural timescale T/L^2 . The large-deviation singularity in this case results from divergence of the diffusive timescale.

In Fig. 4.1 we show the large-deviation functions for the time-averaged position a of the driven walker. As the lattice size L increases, the SCGF and $a(k)$ bend increasingly sharply, and portions of the rate function become increasingly linear.

In Fig. 4.1(d) we show biased dynamical trajectories of the walker, generated at the points $k = k^*$ at which the SCGF bends most sharply. We generated these trajectories using the exact eigenvectors of the tilted generator [28, 29]. Because the SCGF is convex, biased trajectories generated using field k correspond to trajectories that produce a value $a(k) = \lambda'(k)$ of the time-integrated observable a [28], and are the “least unlikely of all the unlikely ways” [4] of achieving the specified time average. For this model these trajectories are intermittent, with the walker switching abruptly from one location on the lattice to another. As a result, histograms of the instantaneous position of the walker are bimodal [panel (e)]. As the lattice size increases, the residence time at each location increases.

The intermittent behavior has a simple physical origin. The probability per unit time for the walker to sit at (fluctuate about) its preferred location is greater than that to sit at any site in the lattice interior, but the latter probability is essentially independent of position (see Section 4.4). If conditioned to achieve a time-averaged position a at (say) the center of the lattice, it could sit for all time at the corresponding lattice location. But it could also spend half its time at its preferred location, and half its time near the far end of the lattice. Given that sitting near the far end of the lattice is not more costly than sitting in the middle, the intermittent strategy is more probable

than the homogeneous one. This argument holds for time T much longer than $\tau(L)$, the emergent mixing time governing intermittency. The probability of crossing the lattice in the difficult direction is $\sim p^L$, and so the timescale for doing so increases exponentially with L .

4.3 Undriven random walker

We now consider an undriven walker whose probability of moving right at any site away from the edges is $p(x) = 1/2$. Again we choose the time-averaged position of the walker as our dynamical observable. As shown in Fig. 4.2, the large-deviation functions $\lambda(k)$ and $a(k)$ again show the emergence of sharp features as L grows, and $I(a)$ flattens, reminiscent of the free energy for the Ising model below its critical temperature [2]. These sharp features become singular in the limit $L \rightarrow \infty$, with the kink occurring at $k^* = 0$ (the untilted generator for a random walker has a spectral gap that vanishes as L^{-2}).

However, the implication of the emergence of distinct “phases” or dynamic intermittency is at odds with the physics of the system. Because of the model’s symmetry, the point $k = k^*$ at which the SCGF shows greatest curvature is $k^* = 0$, corresponding to the unbiased trajectory ensemble. Such trajectories do not display switching behavior, as shown in panels (d) and (e). We also verified that switching behavior occurs at no other values of k : histograms of x/L for biased or conditioned trajectory ensembles are always peaked about a single value. Why then the emergent singularity?

To answer this question we note that the rate function for dynamics controls the rate at which atypical fluctuations decay, and so measures both the probability and basic timescale of those fluctuations. Thus $I(a)$ can be small if the fluctuation a is almost typical, or if the basic timescale governing the establishment and decay of a fluctuation a is large. For diffusive systems such as the walker, the latter factor is important. The natural way to compare systems of different L is at fixed scaled observation time $T_L \equiv T/L^2$, which in large-deviation terms is equivalent to adopting T_L as the new large-deviation speed, such that

$$\rho_T(A) \approx e^{-TI(a)} = e^{-T_L I_L(a)}. \quad (4.5)$$

The object $I_L(a) \equiv I(a)L^2$ is the rate function on this new speed.

In Fig. 4.3 we show the large-deviation functions for the walker in this new frame of reference. Each panel is a rescaling of the panels shown in Fig. 4.2(a–c). These

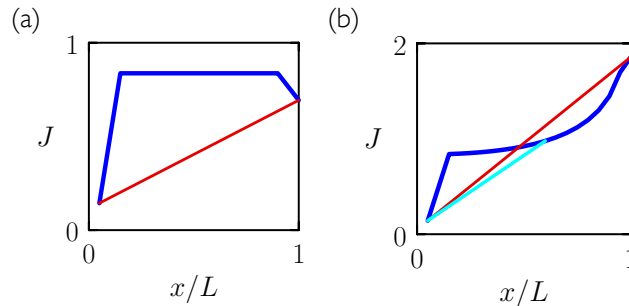


Figure 4.4: Negative log-probability per unit time for the driven walker to achieve a time-averaged position $a = x/L$ in a homogeneous way (blue lines) or a two-state intermittent way (blue and red lines). In panel (a) the walker’s driving is constant, $p(x) = 1/4$, while in panel (b) the tendency of the walker to move left increases with rightward distance, $p(x) = [1 - (x/L)^2]/4$. The lattice size $L = 20$. When the straight lines lie below the blue lines it is more likely for the system to achieve the time-averaged position a corresponding to x/L in an intermittent way. This construction is consistent with conditioned trajectories of these models (Fig. 4.5), as long as the trajectory time comfortably exceeds the time on which switching occurs.

rescaled functions show no sharpening of their features as L increases, and the collapse of the functions confirms that the long timescale associated with the walker is the diffusive one. The natural scales for comparison of these systems are T/L^2 and kL^2 , not T and k .

Therefore in this case it is a divergence of the diffusive mixing time L^2 that causes the singularity, not the emergence of intermittent behavior. One additional issue resolved by the rescaling is the apparent vanishing of the rate function in the limit $L \rightarrow \infty$. If a large-deviation principle applies then the rate function $I(a)$ has a unique zero at the point a_0 at which the system displays its typical behavior [5]. Given the symmetry of the system, the walker’s typical location in the long-time limit is $a_0 = 0$. It is clear that Fig. 4.3(c) is consistent with this idea, and the notion that time is “long”.

In Appendix A we point out that both walker models have a thermodynamic interpretation as lattice polymers, confirming that the existence of a first-order singularity in a thermodynamic system does not automatically imply phase coexistence.

4.4 When should we expect intermittency?

The previous sections show that intermittent conditioned trajectories can accompany dynamical large-deviation singularities, but that singularities can result from the

emergence of a large timescale *absent* intermittency. We show in this section that driven walkers on a lattice can display both intermittent and non-intermittent conditioned dynamics, depending upon the the details of the walker rules and the timescale of observation. The argument we use is analogous to the classic equilibrium procedure of comparing the free energies of homogenous and coexisting phases [1, 2].

Consider again a lattice of L sites, and let the probability that a walker steps right from lattice site $x \in \{1, \dots, L\}$ be $p(x)$ (we have shifted the origin of the lattice relative to the previous sections). Define $q(x) \equiv 1 - p(x)$. Let the lattice be closed, so that $p(1) = 1$ and $p(L) = 0$. The time-integrated position of the walker is $a = (LT)^{-1} \sum_{t=1}^T x_t$, where x_t is the walker's position at discrete time t .

The probability for a walker at an interior site x to fluctuate about that site, i.e. to step right, left, left, and then right again is $p(x)q(x+1)q(x)p(x-1)$. Thus the negative logarithmic probability per unit time for the walker to remain localized near interior site x is the negative logarithm of this quantity divided by 4. Accounting for the different rates at the edges of the lattice, the negative logarithmic probability per unit time for the walker to remain localized near site x is

$$U(x) = \begin{cases} -\frac{1}{2} \ln[p(x)q(x+1)] & x = 1 \\ -\frac{1}{4} \ln[p(x)q(x+1)q(x)p(x-1)] & 1 < x < L \\ -\frac{1}{2} \ln[q(x)p(x-1)] & x = L. \end{cases} \quad (4.6)$$

The negative logarithmic probability per unit time for a homogeneous trajectory, one localized at $x = aL$ for all time, is

$$J_{\text{homog}} = U(x). \quad (4.7)$$

(The quantity J is not the rate function $I(a)$, which relates to the log-probability by which the system achieves the value a by any means.)

By contrast, the negative logarithmic probability per unit time for an intermittent trajectory built from sections of trajectory localized at $x' = a'L$ for time ϕT and at $x'' = a''L$ for time $(1 - \phi)T$ is

$$J_{\text{int}} = \phi U(x') + (1 - \phi)U(x''), \quad (4.8)$$

ignoring switches back and forth between x' and x'' . For the intermittent trajectory to achieve the same time average as the homogeneous one requires

$$\phi x' + (1 - \phi)x'' = x. \quad (4.9)$$

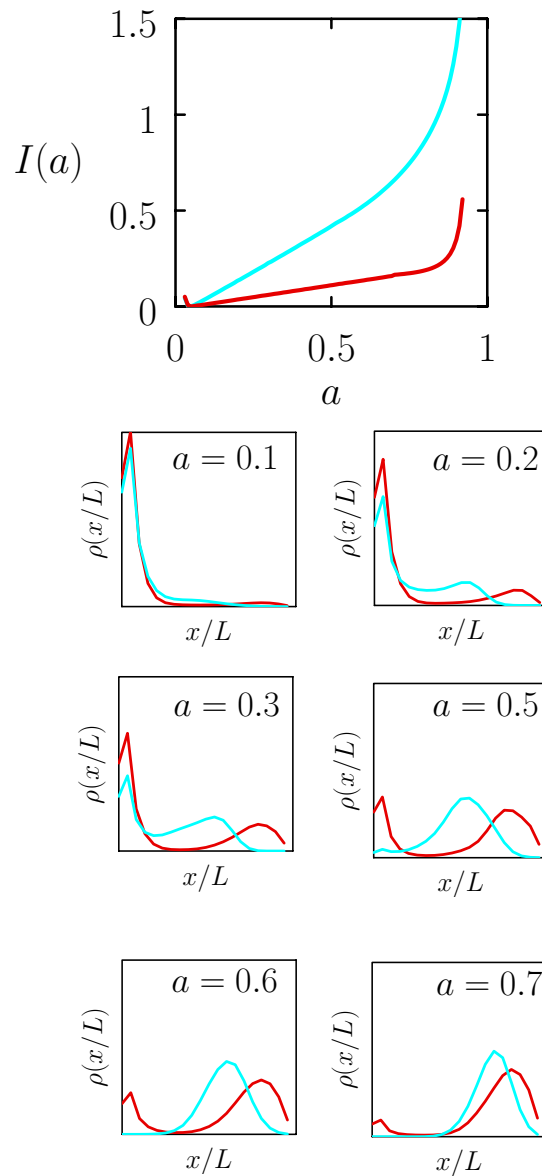


Figure 4.5: Large-deviation rate function $I(a)$ for the time-averaged position of the driven lattice random walker from Section 4.2 (red), together with that for a super-driven walker (cyan) for which the probability to move left increases with distance from the left-hand edge. Shown below are histograms of the instantaneous walker position from trajectories of the two models conditioned to produce various atypical values of a . Consistent with the simple arguments developed in this section, the driven walker displays intermittency, for most values of a , involving sites near the edges of the lattice. By contrast, the super-driven walker shows intermittency for a not too far from the typical value a_0 , involving sites near the middle of the lattice. For a far from a_0 , its conditioned trajectories are homogeneous. For both models, $L = 20$.

If, for a given value of $x = aL$, (4.8) is smaller than (4.7), then intermittent trajectories are more probable than homogeneous trajectories. There may be other types of trajectory that are more probable still, but this simple and approximate argument, which essentially reduces to an assessment of where $U(x)$ is concave, provides a starting point for understanding when intermittency will appear in the conditioned dynamics of the walker.

In Fig. 4.4(a) we show the quantities (4.7) and (4.8) for the driven walker of Section 4.2, for which $p(x) = 1/4$. The negative log-probability per unit time for homogeneous trajectories, Eq. (4.7), is shown in blue. The most probable intermittent trajectory for any x is the one built from the lattice edges, shown in red in the figure. This line lies below the homogeneous result for all x away from the edges, showing that intermittency is the more probable way to achieve a time average in the interior of the lattice.

In Fig. 4.4(b) we consider a “super-driven” walker whose probability of moving in one direction increases with distance in the opposite direction, $p(x) = [1 - (x/L)^2]/4$. For intermittent trajectories to be more likely than homogeneous ones we need to be able to draw a straight line between two points on the function $U(x)$ and have the line lie below $U(x)$. We see that this is possible for some points but not others, and that the lower-lying line (the more probable intermittent strategy) connects the typical point $x \approx 1$ with a point that is near the middle of the lattice, not the edge. Based on this picture we expect the conditioned trajectory ensemble of the super-driven walker to be intermittent for values of a near the typical value $a_0 \approx 1/L$, but not far away, and for the intermittent trajectories to involve locations on the lattice different to the edges occupied by the driven walker.

In Fig. 4.5 we show that these expectations are borne out. In the main panel we show the rate functions $I(a)$ for the time-averaged position of the driven walker (red) and super-driven walker (cyan). Shown below are position histograms for trajectories conditioned to produce various atypical values of a . Consistent with the simple arguments developed in this section, the super-driven walker shows intermittency near $a = a_0$, involving sites near the center of the lattice. For a far from a_0 its conditioned trajectories are homogeneous. The driven walker shows intermittency for a wider range of values of a , and its intermittency always involves sites near the edges of the lattice.

To produce Fig. 4.5 we used the VARD method [30] to calculate the conditioned dynamics of the walker. The unconditioned model has probability $p(x)$ of moving

right from lattice site x . We introduce a reference random walker whose probability of moving right, $\tilde{p}(x)$, is an arbitrary function of x , which we chose to express as a radial basis function neural network. The network has one input node, which takes the value x/L , a single hidden layer of 1000 neurons, each with Gaussian activations, and one output node, $\tilde{p}(x)$. For sufficiently long trajectories the optimal dynamics is Markovian, and can be represented exactly by this ansatz if suitably optimized.

Following Ref. [31] we used neuroevolution of the parameters of the network, equivalent to gradient descent in the presence of Gaussian white noise [32], to extremize the sum of values of $T^{-1} \ln[\tilde{p}(x)/p(x)]$ over a trajectory of T steps of the reference random walker's dynamics, subject to its achieving a specified value of the time-averaged position a . For T long enough, i.e. longer than any emergent mixing time of the reference model, these calculations are equivalent to the eigenvalue calculations of Section 4.2 and Section 4.3 [33], and we recover the rate function of the model and its conditioned dynamics at each point on the rate function.

For $T/\tau(L)$ not large, conditioned trajectories do not resemble their long-time counterparts. For example, for $T = L$ the most probable trajectory whose time-averaged location is the middle of the box, given free choice of initial conditions, is the one that starts at the right-hand wall and crosses the box in L steps. The histogram $\rho(x/L)$ associated with that trajectory is flat. For $T \ll L$ the only viable trajectories respecting the conditioning are those localized near the appropriate value of x/L .

4.5 Singularities in non-ergodic models

We end by noting that dynamical large-deviation singularities also arise in non-ergodic models, such as the irreversible growth model of Refs. [15, 16], and that these singularities are associated with phenomenology of a distinct type to that exhibited by the walker models.

Briefly, the growth model possesses two types of particle $x \in \{-1, 1\}$, added to an urn at discrete timesteps with a relative probability that depends on the quantity $\gamma(a) = e^{-Ja}/(2 \cosh Ja)$, where J is a parameter. Here a , the dynamical observable, is the sum of values of x at each timestep, divided by total time T . This model can also be viewed as a two-state switch with a switching probability that depends on the history of switching [27].

This model undergoes a phase transition, at a value of $J = 1$, between a regime in which trajectories display one type of characteristic behavior and a regime in which

trajectories display two types of characteristic behavior. At the critical point the trajectory ensemble displays anomalous fluctuations. Associated with this transition is a change of shape of the model's large-deviation rate function (see Appendix B), and a dynamical large-deviation singularity.

Long trajectories of the conditioned driven walker and the growth model show two-state switching behavior, but in the growth model's case the probability of switching depends on the history of switching. As a result, trajectories that adopt one type of behavior become more likely, as time advances, to remain committed to that behavior [34]. The result is ergodicity breaking and an ensemble of trajectories that in the long-time limit spontaneously adopt one of two characteristic behaviors.

The nature of the trajectory ensemble of the growth model and walker models is summarized in Fig. 4.6. Conditioned trajectories of the driven walker display intermittency and a bimodal distribution of the *instantaneous* coordinate x/L , but the distribution of the *time-integrated* quantity a is unimodal. In the growth model, the distribution of the time-integrated quantity a is bimodal.

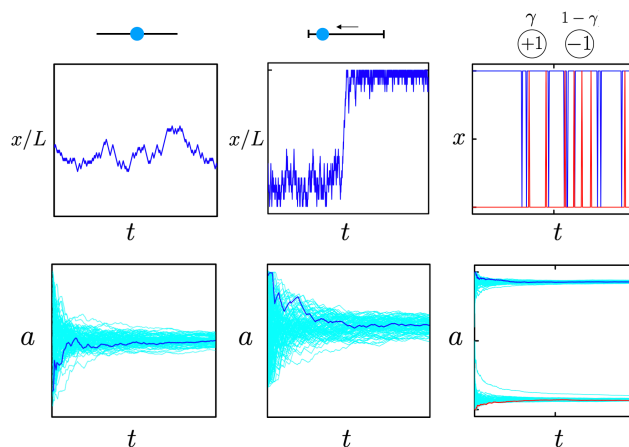


Figure 4.6: Summary of the biased trajectory ensembles associated with three model systems, each generated at the point k^* at which the SCGF associated with the time-integrated observable has largest curvature. For the undriven walker (left) and the growth model (right) we have $k^* = 0$, while for the driven walker (center) we have $k^* \neq 0$. The top panels show the instantaneous dynamical observable associated with a single trajectory (two trajectories in the case of the growth model). The lower panels show a , the time-integrated version of x , for an ensemble of 100 trajectories. The trajectories of the top panels are indicated in the bottom panels by the dark blue or red lines.

4.6 Discussion & Conclusions

Phase transitions are collective phenomena that occur in the limit of large system size, and which influence the behavior of finite systems [1–3]. Phase transitions induce singularities in thermodynamic potentials and large-deviation functions. However, similar-looking singularities can arise in the absence of collective phenomena. For instance, abrupt features are seen in the large-deviation functions of finite systems in the reducible limit, when the connections between microstates are severed [23–27]. Here we have shown that singularities can also emerge in the limit of large system size if a model becomes slow as it becomes large, whether or not it exhibits behavior reminiscent of a phase transition.

The undriven walker of Section 4.3 has a rate function $I(a)$ [Fig. 4.2(c)] that in the limit $L \rightarrow \infty$ looks similar to that of the 2D Ising model’s magnetization rate function below T_c [2, 5]. Interpreting the walker in this context suggests that it can be switched between two behaviors (corresponding to walkers localized either size of the lattice) with an infinitesimal field k . Moreover, because the switching occurs about the value $k^* = 0$, a large unbiased version of the system appears poised on the brink of phase coexistence between these behaviors. However, the conditioned trajectory ensemble of the walker shows no evidence of distinct dynamical phases. In our view a more natural interpretation is that the walker’s diffusive timescale diverges as L^2 . When time T and field k are rescaled in order to view systems of different size at fixed T/L^2 , it is clear that the probability distribution of a remains regular (Fig. 4.3). Departures from the typical behavior (a time average in the middle of the lattice) remain rare. The distinction between large-deviation singularities induced by cooperative behavior or by dynamics that is simply slow is the idea expressed in Fig. 1 of Ref. [27].

The driven walker of Section 4.2 displays emergent intermittency when its trajectories are conditioned to produce particular time-averaged positions, provided that $T \gg \tau(L)$, the emergent switching time. In Section 4.4 we show that the details of the walker’s rules and the value of the imposed time averaged determine whether intermittency or homogeneity dominates. Other authors have noted the similarity of dynamical intermittency to magnetization stripes in the Ising strip crystal, if we associate time with the long Ising box direction and regard the two walker lattice positions as “phases” [13]. However, if we swap the long and short directions of the Ising box then the direction of the interface changes, but the identity of the phases does not. If we do similarly with the walker, and make $L \gg T$, then its conditioned

trajectories can no longer be intermittent. This change switches the direction of the walker’s space-time “interface”, but also alters the identity and number of the “phases” seen.

The growth model (or two-state switch with memory) discussed in Section 4.5 is unlike the other models discussed in that it possesses only one independent dimension, that of time T . It is clearly different in detail to models with spatial degrees of freedom, but its phenomenology is similar to that of the 2D Ising model in several important respects, with T playing the role of system size. The growth model’s large-deviation function changes from being regular to being singular upon changing a model parameter J . In the singular regime the steady-state rate function of the time-extensive quantity is concave (Section B), reflecting two distinct dynamical behaviors and an associated ergodicity breaking. The origin of this behavior is cooperativity, the tendency of the model to favor one behavior the more it exhibits it.

The scaled cumulant-generating functions (SCGFs) of these models, which display kinks in certain limits, do not specify which type of dynamics the model exhibits. It is worth noting that nor do the rate functions to which they are Legendre dual. For the walker models, the SCGF kinks are related to portions of the rate function that are linear with zero gradient (the undriven walker) and with nonzero gradient (the driven walker). The latter is suggestive of intermittency, although linear rate functions also arise in other types of process, such as relaxation to an absorbing state [5, 35]. Moreover, simple switching models, which are by design intermittent, display, as the switching time increases, rate functions that broaden and vanish, becoming linear with zero gradient [23–25] (see e.g. Fig. 5 of Ref. [27]). Those rate functions therefore resemble the rate functions of the *undriven* walker, although the latter shows no intermittency. Explicit calculation of the dynamics that gives rise to the rate function is necessary to determine how the model realizes its rare behavior.

All of the models discussed here display kinks of their dynamical large-deviation functions in certain parameter regimes, but show phase transition-like behavior to different extents. On this basis we suggest that phenomenology should guide the classification of singularity-bearing models discussed in the literature.

4.7 Acknowledgments

S.W. performed work at the Molecular Foundry, Lawrence Berkeley National Laboratory, supported by the Office of Science, Office of Basic Energy Sciences, of the U.S. Department of Energy under Contract No. DE-AC02-05CH11231.

A Appendix: Thermodynamic interpretation of walker models

The random walkers of Section 4.2 and Section 4.3 have a thermodynamic interpretation, if we interpret the time dimension of the walker as a second spatial dimension. Then every trajectory ω of the walker becomes a configuration of a lattice polymer. On each row $n \in \{1, \dots, N\}$ of the lattice (formerly the time direction), the polymer occupies a single site $x_n \in \{-(L-1)/2, \dots, (L-1)/2\}$. The polymer is held at reciprocal temperature $\beta = (k_B T)^{-1}$, and we define the energy of configuration ω to be

$$\beta E(\omega) = -\ln \pi_1(x_0^\omega) - \sum_{i=2}^N \ln W_{x_i^\omega x_{i-1}^\omega}. \quad (\text{A1})$$

Here $\pi_1(x)$ is the probability that the polymer has position x on the first row of the lattice.

The probability that the thermodynamic system has configuration ω is equal to the probability that the dynamical system generates trajectory ω . The probability of the polymer achieving a row-averaged mean position a is

$$\rho_N(a) = e^{-\beta N g_N(a)}, \quad (\text{A2})$$

where

$$\beta g_N(a) = -\frac{1}{N} \ln \sum_{\omega: a(\omega)=a} e^{-\beta E(\omega)} \quad (\text{A3})$$

is the reduced free energy per lattice row. In the limit that N becomes large, the function $g_N(a)$ goes over to an N independent function $g(a)$, leading to the large deviation principle

$$\rho_N(a) \approx e^{-\beta N g(a)}, \quad (\text{A4})$$

the thermodynamic analog of (4.3). Taking the Legendre transform of $g(a)$ produces the function $f(k)$ with field k . Then $g(a) = I(a)$ and $f(k) = \lambda(k)$.

As a result, the thermodynamic polymer exhibits the same behavior as the dynamical walker, but does so in space rather than time. In particular, in the case $p = 1/2$ the correlation length of the polymer diverges as L diverges, leading to a broadening of the free energy $g(a)$ and the emergence of a kink in $f(k)$. However, analogous

to the dynamical case, the probability distribution of polymer positions remains uniform, and no distinct “phases” accompany the singularity.

B Appendix: Large-deviation functions of the growth model

The irreversible growth model of Refs. [15, 16], summarized in Section 4.5, is sketched at the top of Fig. B2 in the form of a two-state switch with memory. In that figure we show trajectories of the model at and at either side of the dynamical critical point $J_c = 1$. Associated with this phase transition is a large-deviation singularity: the rate function for a becomes non-convex at the critical point, and the associated SCGF is kinked [15, 16]. The non-convexity in the two-phase region is of different character to that seen in ergodic models that display dynamical intermittency. In this appendix we explore this point further.

The black lines in Fig. B2 are the rate-function bound

$$I_0(a) = \frac{1-a}{2} \ln(1-a) + \frac{1+a}{2} \ln(1+a) - Ja^2 + \ln \cosh Ja, \quad (\text{B1})$$

derived in Ref. [16] under the assumption of steady-state growth. We will call Eq. (B1) the steady-state rate function. It is convex for $J < 1$ and non-convex (concave) for $J > 1$.

The steady-state rate function is consistent with the empirical large-deviation rate function of the model in the one-phase and two-phase regions. In Fig. B1 we show empirical rate functions $-T^{-1} \ln \rho_T(A)$ for unbiased trajectories of the growth model, compared with the form (B1). To measure histograms $\rho_T(A)$ we used of order 10^6 trajectories, propagated for the times shown, and sampled a using 500 evenly-spaced bins (in Fig. B1(b) we used 5000 bins and simulation times one-fifth of those in the other panels). Panels are labeled with the value of the coupling J , and all simulations (except those in Fig. B1(c)) were begun from time $T_0 = 0$, corresponding to an “unassembled” structure.

For couplings J well below and well above the critical point, the empirical rate functions are convex and concave, respectively, and are consistent with the steady-state rate function (B1) (see particularly the enlargement of the right-hand side of the plot in Fig. B1(b)). Near the critical point, on either side, the relaxation time of the model is large [15], and empirical rate functions, for the times simulated, depart from the form (B1). (The distribution $\rho_T(A)$ (not the rate function) at the critical point $J_c = 1$ is bimodal, similar to the magnetization distribution of the 2D critical Ising

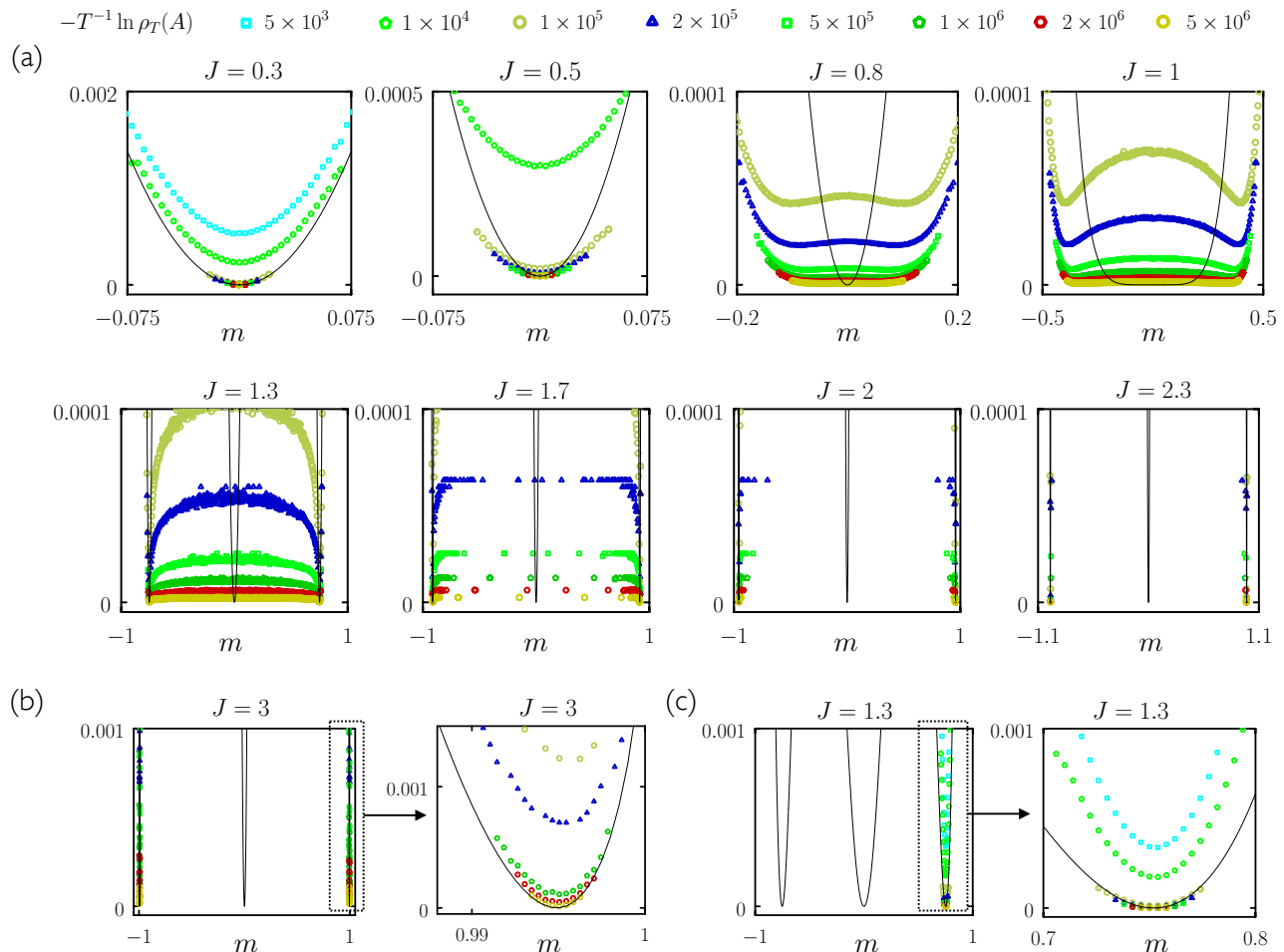


Figure B1: Empirical rate functions $-T^{-1} \ln \rho_T(A)$ for different values of trajectory time T (denoted by symbols) for the irreversible growth model, compared with the steady-state rate function (B1) (black lines). Panels are labeled by values of the parameter J . (a) Far from the critical point $J_c = 1$ the empirical rate functions are convex in the one-phase region ($J < 1$) and concave in the two-phase region ($J > 1$). Close to the critical point the behavior of the model, on the times simulated, is influenced by a population of transient trajectories. (b) Enlargement of the right-hand portion of the plot for $J = 3$ shows the empirical rate function to be consistent with the form (B1), indicating steady-state growth. (c) We again consider the case $J = 1.3$, but now initiate simulations from a pre-made structure of size $T_0 = 1000$ and composition a , consistent with the position of the right-hand minimum of the steady-state rate function (B1). Doing so allows us to effectively access longer timescales than we could from “unassembled” initial conditions. The empirical rate function derived from the resulting ensemble of trajectories is again consistent with the form (B1).

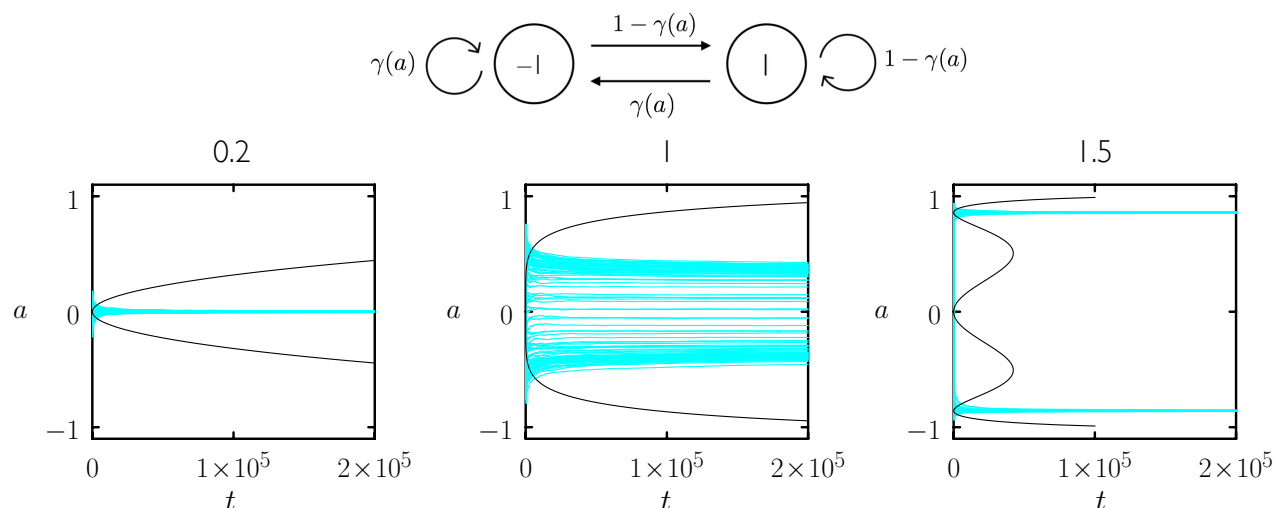


Figure B2: Time-integrated observable a for ensembles of trajectories of the irreversible growth model of Refs. [15, 16]. From left to right we show the one-phase region, the critical point, and the two-phase region. Panels are labeled by the values of the model parameter J . The black lines are derived from (B1).

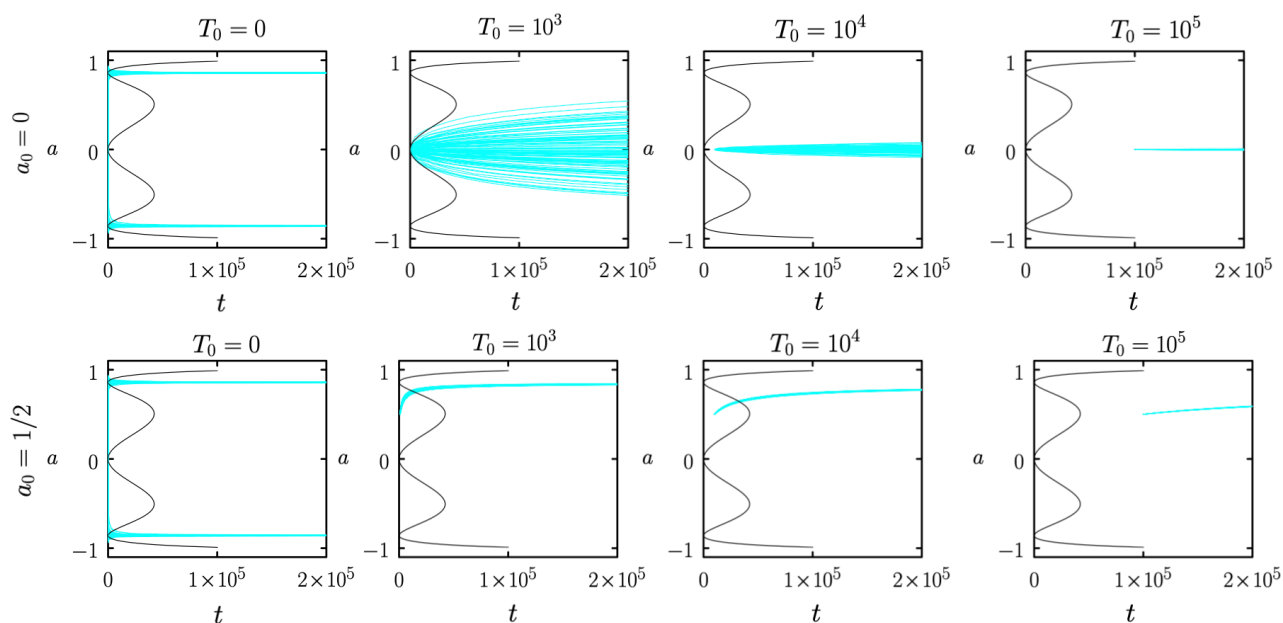


Figure B3: In the two-phase regime of the growth model, trajectory ensembles begun from structures of increasing size T_0 , having composition $a_0 = 0$ (top row), become increasingly strongly confined by the unstable dynamical attractor at $a = 0$, corresponding to the central minimum of the function (B1). By contrast, large structures of initial composition $a_0 \neq 0$ not consistent with any of the minima are driven toward the stable dynamical attractors (in this figure only, the symbol a_0 denotes initial composition, and not a typical value of the trajectory ensemble.)

model in square geometry [36].) In the two-phase regime, close to the critical point, we can detect by direct simulation a population of transient trajectories that linger for some time near the unstable fixed point $a = 0$ (see Fig. B3), and later commit to one of the stable attractors. These trajectories populate the middle portions of the empirical rate functions close to the critical point. In this regime the empirical rate function consists of two convex pieces joined by a bar, and in the limit of large T the height of this bar moves to zero.

This behavior is consistent with Ref. [37], which showed that the rate function $I(a)$ accounting for steady-state *and* transient trajectories is zero between the stable minima in the two-phase regime. However, whether the empirical rate function is described by this result or by the steady-state rate function bound (B1) depends strongly upon where in parameter space we operate. Simulations for the times and couplings used in Ref. [37] (e.g. at the point $J = 1.3$; see panel in Fig. B1) are dominated by transient effects, and are not representative of the long-time behavior of the model in the two-phase regime, contrary to the claim made in [37]. As the trajectory time T becomes large, or J is made larger (so reducing the relaxation time of the model), the number of trajectories required to observe transient trajectories. For instance, at $J = 3$ and $T > 10^5$, none of 10^8 trajectories was of the transient type. By contrast, trajectories in the vicinity of the stable attractors can be seen at all times, and the rare trajectories detected by direct simulation result from invasion from those attractors. As a result, for long times and a large but computationally feasible number of trajectories, the empirical rate function of the model in the two-phase region is non-convex (concave), and is consistent with the steady-state rate function (B1). This concavity reflects ergodicity breaking and the presence of distinct dynamical phases.

The behavior of the growth model compared to that of the walker models reinforces the importance of phenomenology to any classification scheme: these models display similar large-deviation singularities, but support phase transition-like behavior to different extents.

References

1. Goldenfeld, N. *Lectures on phase transitions and the renormalization group* (CRC Press, 2018).
2. Binney, J. J., Dowrick, N., Fisher, A. & Newman, M. *The theory of critical phenomena: an introduction to the renormalization group* (Oxford University Press, Inc., 1992).

3. Chandler, D. Introduction to modern statistical mechanics. *Introduction to Modern Statistical Mechanics*, by David Chandler, pp. 288. Foreword by David Chandler. Oxford University Press, Sep 1987. ISBN-10: 0195042778. ISBN-13: 9780195042771, 288 (1987).
4. Den Hollander, F. *Large Deviations* (American Mathematical Soc., 2008).
5. Touchette, H. The large deviation approach to statistical mechanics. *Physics Reports* **478**, 1–69 (2009).
6. Gallavotti, G. & Cohen, E. G. D. Dynamical ensembles in nonequilibrium statistical mechanics. *Physical Review Letters* **74**, 2694 (1995).
7. Lebowitz, J. L. & Spohn, H. A Gallavotti–Cohen-type symmetry in the large deviation functional for stochastic dynamics. *Journal of Statistical Physics* **95**, 333–365 (1999).
8. Onsager, L. Crystal statistics. I. A two-dimensional model with an order-disorder transition. *Physical Review* **65**, 117 (1944).
9. Corberi, F. & Sarracino, A. Probability Distributions with Singularities. *Entropy* **21**, 312 (2019).
10. Garrahan, J. P. *et al.* First-order dynamical phase transition in models of glasses: an approach based on ensembles of histories. *Journal of Physics A: Mathematical and Theoretical* **42**, 075007 (2009).
11. Vaikuntanathan, S., Gingrich, T. R. & Geissler, P. L. Dynamic phase transitions in simple driven kinetic networks. *Physical Review E* **89**, 062108 (2014).
12. Pietzonka, P., Kleinbeck, K. & Seifert, U. Extreme fluctuations of active Brownian motion. *New Journal of Physics* **18**, 052001 (2016).
13. Nemoto, T., Jack, R. L. & Lecomte, V. Finite-size scaling of a first-order dynamical phase transition: Adaptive population dynamics and an effective model. *Physical Review Letters* **118**, 115702 (2017).
14. Nyawo, P. T. & Touchette, H. A minimal model of dynamical phase transition. *EPL (EuroPhysics Letters)* **116**, 50009 (2017).
15. Klymko, K., Garrahan, J. P. & Whitlam, S. Similarity of ensembles of trajectories of reversible and irreversible growth processes. *Physical Review E* **96**, 042126 (2017).
16. Klymko, K., Geissler, P. L., Garrahan, J. P. & Whitlam, S. Rare behavior of growth processes via umbrella sampling of trajectories. *Phys. Rev. E* **97**, 032123. <https://link.aps.org/doi/10.1103/PhysRevE.97.032123> (3 Mar. 2018).
17. Horowitz, J. M. & Kulkarni, R. V. Stochastic gene expression conditioned on large deviations. *Physical Biology* **14**, 03LT01 (2017).

18. Nyawo, P. T. & Touchette, H. Dynamical phase transition in drifted Brownian motion. *Physical Review E* **98**, 052103 (2018).
19. Nemoto, T., Fodor, É., Cates, M. E., Jack, R. L. & Tailleur, J. Optimizing active work: Dynamical phase transitions, collective motion, and jamming. *Physical Review E* **99**, 022605 (2019).
20. Mallmin, E., Blythe, R. A. & Evans, M. R. A comparison of dynamical fluctuations of biased diffusion and run-and-tumble dynamics in one dimension. *arXiv preprint arXiv:1905.10260* (2019).
21. Jack, R. L. Ergodicity and large deviations in physical systems with stochastic dynamics. *The European Physical Journal B* **93**, 1–22 (2020).
22. Casert, C., Vieijra, T., Whitelam, S. & Tamblyn, I. Dynamical large deviations of two-dimensional kinetically constrained models using a neural-network state ansatz. *arXiv preprint arXiv:2011.08657* (2020).
23. Dinwoodie, I. H. & Zabell, S. L. Large Deviations for Exchangeable Random Vectors. *The Annals of Probability* **20**, 1147–1166 (1992).
24. Dinwoodie, I. H. Identifying a large deviation rate function. *Annals of probability* **21**, 216–231 (1993).
25. Coghi, F., Morand, J. & Touchette, H. Large deviations of random walks on random graphs. *Physical Review E* **99**, 022137 (2019).
26. Garrahan, J. P. & Lesanovsky, I. Comment on “Abrupt transition in the structural formation of interconnected network”, F. Radicchi and A. Arenas, *Nature Phys.* **9**, 717 (2013). *arXiv preprint arXiv:1406.4706* (2014).
27. Whitelam, S. Large deviations in the presence of cooperativity and slow dynamics. *Physical Review E* **97**, 062109 (2018).
28. Chetrite, R. & Touchette, H. Variational and optimal control representations of conditioned and driven processes. *Journal of Statistical Mechanics: Theory and Experiment* **2015**, P12001 (2015).
29. Ray, U., Chan, G. K.-L. & Limmer, D. T. Exact fluctuations of nonequilibrium steady states from approximate auxiliary dynamics. *Physical Review Letters* **120**, 210602 (2018).
30. Jacobson, D. & Whitelam, S. Direct evaluation of dynamical large-deviation rate functions using a variational ansatz. *Physical Review E* **100**, 052139 (2019).
31. Whitelam, S., Jacobson, D. & Tamblyn, I. Evolutionary reinforcement learning of dynamical large deviations. *The Journal of Chemical Physics* **153**, 044113 (2020).
32. Whitelam, S., Selin, V., Park, S.-W. & Tamblyn, I. Correspondence between neuroevolution and gradient descent. *arXiv preprint arXiv:2008.06643* (2020).

33. Chetrite, R. & Touchette, H. Nonequilibrium microcanonical and canonical ensembles and their equivalence. *Physical Review Letters* **111**, 120601 (2013).
34. Morris, R. G. & Rogers, T. Growth-induced breaking and unbreaking of ergodicity in fully-connected spin systems. *Journal of Physics A: Mathematical and Theoretical* **47**, 342003. <http://stacks.iop.org/1751-8121/47/i=34/a=342003> (2014).
35. Oono, Y. Large deviation and statistical Physics. *Progress of Theoretical Physics Supplement* **99**, 165–205 (1989).
36. Cardozo, D. L. & Holdsworth, P. C. Finite-size scaling of the magnetization probability density for the critical Ising model in slab geometry. *Journal of Physics: Condensed Matter* **28**, 166007 (2016).
37. Jack, R. L. Large deviations in models of growing clusters with symmetry-breaking transitions. *Physical Review E* **100**, 012140 (2019).